12-2020

Electromagnetic Interference Shielding Effectiveness of Interlayered Systems Containing Metal-Oxide, Conducting Polymer and Carbon Nanotube Reinforced Polymeric Composites

Shaik Merkatur Hakim Marjuban
The University of Texas Rio Grande Valley

ELECTROMAGNETIC INTERFERENCE SHIELDING EFFECTIVENESS OF INTERLAYERED SYSTEMS CONTAINING METAL-OXIDE, CONDUCTING POLYMER AND CARBON NANOTUBE REINFORCED POLYMERIC COMPOSITES

A Thesis

by

SHAIK MERKATUR HAKIM MARJUBAN

Submitted to the Graduate College of
The University of Texas Rio Grande Valley
In partial fulfillment of the requirements for the degree of

MASTER OF SCIENCE IN ENGINEERING

December 2020

Major Subject: Mechanical Engineering

ELECTROMAGNETIC INTERFERENCE SHIELDING EFFECTIVENESS OF INTERLAYERED SYSTEMS CONTAINING METAL-OXIDE, CONDUCTING POLYMER AND CARBON NANOTUBE REINFORCED POLYMERIC COMPOSITES

A Thesis
by
SHAIK MERKATUR HAKIM MARJUBAN

COMMITTEE MEMBERS

Dr. Karen Lozano
Chair of Committee

Dr. Horacio Vasquez
Committee Member

Dr. Laura Benitez
Committee Member

Dr Javier Ortega
Committee Member

December 2020

ABSTRACT

Marjuban, Shaik Merkatur Hakim, Electromagnetic Interference Shielding Effectiveness of Interlayered Systems Containing Metal-oxide, Conducting Polymer and Carbon Nanotubes Reinforced Polymeric Composites. Master of Science in Engineering (MSE), Dec 2020, 129 pp., 11 tables, 41 figures, 202 references, 78 titles.

The Electromagnetic Interference (EMI) Shielding Effectiveness (SE) has become one of the important requirements for the devices associated with telecommunication systems consisting of large frequency bands. The degradation of the quality of transmitting signal influenced by frequencies emitting from external sources can be reduced by covering the circuits of the devices by EMI Shielding materials like polymer composites, metal-based nanofiber mats, the metal of oxide films, etc. The investigation strives for the attenuation of EMI by introducing two composite mats from conducting polymer-based, multiwalled carbon nanotubes (MWCNTs) coated Nylon 6 nanofiber composites. Two other composite mats are also developed by the Forcespinning® method using sol solution of functionalized multiwalled carbon nanotubes (f-MWCNTs) and magnetite (Fe_3O_4) into as-prepared polyacrylonitrile (PAN) which is then carbonized at elevated temperature to convert it into carbon nanofiber (CNF). A total of four layers of mats are stacked and compression molded together to develop one multilayered composite (MLC 1). The Fe_3O_4 has higher magnetic properties which may provide a good magnetic loss effect. The focus is to investigate the synergistic effects between higher magnetic Fe_3O_4, conductive MWCNTs nanofillers with the dielectric CNF, conducting polymer, and

functionalized MWCNTs coated nanofiber composite which can provide information about the dominating mechanism. (Absorption, reflection, or multiple reflections) for EMI SE. The multilayered composite (MLC 2) consisting 8 layers (repeating the stacking sequence again) has given the highest obtained value more than 40 dB EMI SE in the frequency range from 300-500 MHz. The results will bring some findings of optimized materials yielding good EMI SE in lightweight applications.

DEDICATION

The research work is wholeheartedly dedicated to our beloved parents, the greatest soldier, who have been our source of inspiration and gave us strength when we thought of giving up, who continually provide their moral, spiritual, emotional, and financial support. To our brothers, sisters, relatives, friends, and classmates who shared their words of advice and encouragement to complete this task. And lastly, I am dedicated to the Almighty, thank you for the guidance, strength, power of the mind, protection, and skills and giving us a healthy life. All of these, we offer to you.

ACKNOWLEDGEMENTS

I deeply acknowledge the support received by the Presidential Graduate Research Assistantship (PGRA) award and NSF PREM in aiming for enhancing graduate research and students' career development.

I would like to express my deep and sincere gratitude to my research supervisor, Dr. Karen Lozano, for allowing me to do research and providing invaluable guidance throughout this research. Her dynamism, vision, sincerity, motivation have deeply inspired me to carry out the research. It was a great privilege and honor to work and study under her guidance.
I would also like to mention my thesis committee members, Dr. Horacio Vasquez, Dr. Laura Benitez and Dr. Javier Ortega for their encouragement, insightful advice, and support. Besides, I want to acknowledge Dr. Victoria Padilla for her continuous help, intuitive approach to make my research the safest way possible. My special thanks to Dr. Swati Mohan for her collaborative research work and strategic techniques.

I am also grateful to all the master students to help me learning different equipment, data evaluation. I can’t help mentioning Raul Barbosa, Roberto Orrostieta, Ydana Virgen, Dulce Capitanachi, Alex Castillo for their tremendous support, love, and inspiration.

Finally, I would like to thank my parents, whose love and guidance are with me in whatever I pursue. Most importantly, I wish to thank my loving and supportive wife, Musfira, who provides unending inspiration.

TABLE OF CONTENTS

Page

LIST OF TABLES

Page

LIST OF FIGURES

Page

CHAPTER I

INTRODUCTION

The development of robust electromagnetic shielding materials has become a coherent goal alongside building miniature size electronic devices such as cellphone, different medical equipment, multipurpose sensors, and other telecommunication devices to maintain their efficient performance. Compatibility of the metallic materials with the electronic devices based on their environmental impact has certain limitations such as fast degradation in atmospheric parameter changing. Maintaining optimal shielding output with proper longevity can be offered by multilayered material. Besides, it can provide less weight while compensating for the higher shielding capacity derived from monolayer metallic coating or metal body.

Nylon 6 is one of the less biodegradable synthetic polymers suitable for a wide range of commercial, the industrial field for its higher elastic and tensile properties such as fatigue resistance. It possesses stretching, waterproofing, higher resistance to strain, abrasion, wear. It doesn't get affected easily by solvents derived from alkalis and weak acids. Free of toxicity makes it suitable for food, medical multilayered packaging. Several processes have been also conducted to develop PVA hydrogel and membranes for biomedical devices. Thermal stability under prolonged heating, better charge storage capacity, great dielectric strength has made it a potential candidate for electrical application. Incorporating conducting polymers like polyaniline (PANI), Polyindole (PIn) in Nylon 6 matrix can extend the electrical properties output in many

folds. The coercive force of this nanoparticle within the matrix can promote EMI shielding stability. Doping of conductive polymer with functional group incorporation can provide additional contribution in EMI shielding capacity. Also, due to great affinity between nylon and functional groups such as carboxyl, the coating of functionalized carbon nanotubes (CNTs) on nylon surface can provide a conductive surface offering great shielding capacity.

On the other side, Polyacrylonitrile (PAN) is a homopolymer and copolymer of high molecular weight. It is a thermoplastic synthetic polymer, doesn't melt under normal condition. PAN fibers are used as the precursor in the production of high-quality carbon fibers (CFs) [1]. Carbonization of PAN fiber produce wide variety of conductive property-based carbon fibers depending on the carbonization temperature while stabilization is required to cross-link the polymer and prevent relaxation of chain scission during carbonization. The obtained PAN fiber possesses less defects with high orientation of mechanical properties. It is superior thermal stability compared to Polyethylene (PE) fiber where its strength is not affected in environment above 130^{o} C. Besides, It has great anti-alkaline properties and light fastness [2]. Introducing nanoparticles within CFs such as Iron (III) Oxide (Magnetite) and Carbon Nanotubes (CNTs) may provide better magnetic and conductive properties respectively, therefore, enhance the electromagnetic shielding properties. Proper mixing and dispersion of NPs in polymer solution is necessary to produce homogenous distribution of NPs within polymer matrix.

Forcespinning® method can draw fiber several hundred times than the conventional fiber production technique. It is a novel method that makes use of centrifugal forces to produce nanofibers rapidly and at high yields without the requirements of electric fields. With the addition of magnetite (Fe_3O_4) and partially soluble amine functionalized multiwalled Carbon Nanotubes (MWCNTs) in PAN solution can execute doping of nanoparticles attached to polymer

filler surface. In a similar way, conductive Nylon 6 fiber mat can be prepared with an additional doping of PIn by in-situ polymerization.

The fabricated PIn based polymer mat can act as an intermediate layer of the multilayer composites. The other layers from PAN CFs had been developed in order to support the Nylon fiber mat by reducing thermal effects or degradation during heat compression procedure and provide mechanical rigidity in overall structure.

CHAPTER II

REVIEW OF LITERATURE

2.1 Background on Shielding

Since 1859, there was not even a little observation of electronic communication technology other than the telegraph. Generally, it is obvious to believe the non-existence of the concept of electromagnetic shielding. Other than that, before the evolution of communication technologies, the phenomenon of shifting the sun's magnetic poles is one way of understanding it which has precedence over other primitive concepts regarding electromagnetic interference. The magnetic field changing along with Sun's surface activity generates sunspots within a solar cycle causing giant eruptions which have a tremendous effect on the earth's telecommunication systems [3]. This effect is minimized by the earth's geomagnetic field as a protective barrier interacting with solar wind containing charged particles. Apart from this natural emission, the radio communication systems from their earliest inventions have added fatalistic effects on electrical circuits or the devices associated with it. Innovations of electronic equipment with the progress of telecommunication systems often require smooth, noise, or vibration-free features that allow today's consumers to grasp the benefits of products and services. Technologies utilized for telecommunications have transitioned greatly over the last 50 years. Along with it, major fundamental change in industrial and social structure has occurred in the architecture of telecommunication networks. The societal foundation is emboldened by the participation of

people across the globe disadvantaged by geography. The availability of digital communication is owned by an individual from minimally privileged area plays a vital role in overall communication platform where cost-effective, untroubled, lightweight features have become a function of a telecommunication network. Any disruption of this wide platform may severely affect the economy and social stability by the emissions. Apart from that the short-term or even long-term acute exposer can have drastic effects on human and biological systems [4-6].

The recent scientific knowledge stipulates easier means of the platform containing secured transmission with electromagnetic compatibility often required to reduce risk of operators of machines or provide safety to medical implants such as cardiac pacemakers, insulin pumps, and hearing aid from high-intensity EM radiation [7]. Besides, the proper functioning of the devices such as cellphones, electric circuits, and other wireless mediums depends on comprising of a preventive barrier. A barrier that can be denoted by wave absorbing materials. The increasing number of devices required by the growth of the human population always look for the highest capacity of shielding performance. The smaller size and faster-operating speeds of these components make it more challenging to manage EM pollution. Miniaturization of components shortens the propagation path between sources and receptors which is more prone to interference. Microchip destruction during handling may lead to electronic discharge causing concerns for aircraft and automobiles [8]. The shielding can prevent access to data stored on Radio-Frequency Identification (RFID) chips or embedded in other devices. It can be used in combination with air-gapped systems to extend and complement existing security features widely used in military, government, and financial facilities [9]. The general way in the present to shield electrical devices is reflection-based use of metallic sheets which has been being adopted for more than two centuries. Relying on the position of the emission source, the Faraday

cage operates from DC to the high frequency with the activity of reorganizing of electric charges in the shield conductor to dismiss the total electric field inside or outside the cage. On top of that, Faraday cage has no control over the magnetic field. The necessity of material possessing high permeable features can provide a similar shielding mechanism for the magnetic field. Polymer composites can offer lightweight, cost feasibility, easy shaping along with better shielding properties while combined with conductive nanoparticles [10]

Table 1. Shielding Modeling in Practice

Models	Dependency Parameters	Advantages	Disadvantages
Metallic Enclosure	Geometry, conductivity, permeability, correction factor	No inclusion of the effects of apertures or other discontinuities	Impractical use of the all-welded enclosure
EMI Gasket	Conductivity at interface, air or high resistance gaps, junction geometry, applied force	Preserve continuity of current flow,	Not practical for mechanical considerations, EM leakage through a seam in between gaskets and shield
Shield with Apertures	Apertures geometry	Excessive skin effect beyond 150 MHz	The presence of apertures such as windows, vents, seams, and joint degrade shielding effectiveness (SE)
Cavity Resonance	Reflecting cubicle of interior dimensions	Tight grounding, a capacitor between the signal line and the screen can shunt away high-frequency disturbance	Resonance of an empty metallic box can result in negative SE

2.2 History of EMI Shielding

In 1933, in an attempt to understand the long-term negative effects that can arise from radio frequency, the electromagnetic interference (EMI) field gained its recognition at a meeting of the International Electrotechnical Commission (IEC) in Paris under the name of CISPR (International Special Committee on Radio interference). From its emergence in 1820 by Morse, Henry, and Vail, the popularity of radio had elevated so high that it had become a must household appliance during the Depression. But the intentional and unintentional RF transmissions began affecting the other electrical systems, thus the awareness of EMI began to grow within the electronics community. In 1934, CISPR started producing and distributing requirements regarding the recommended allowable emissions and immunity limits for electronic devices, which have evolved into much of the world's EMC regulations. Researchers started investigating electromagnetic emissions progressively throughout the 1960s, 1970s, and 1980s. In 1967, Mil Standard 461A was established by the US military to test and verify the requirements for electronic devices used in Military applications as well as emissions and susceptibility limits for new Military electronic equipment. Besides, in 1979, legal limits were attributed to EM emissions for all digital equipment by the FCC in the USA. The regulations have been changed many times until they become faster, smaller, and more powerful having a greater disposition to interact with the operations of other electrical systems. For instance, in the mid-1980s, the European Union member states acquired "new approach" directives and standardized technical requirements for products without facing any barrier to trade within the EC. With the understanding of the creation of noise to minimize transmitting noise, engineers and scientists have been trying to build shielding enclosure more effective than typical Faraday cages. The researchers from different companies are also struggling to find long term solution to

avoid EM radiation to protect the electronic devices susceptible to EMI by designing a new type of structures and filtering. The accomplishment was gained by creating multiple professional certification levels to ensure electrical systems compatible with radiation. The regulations helped the professional to guide the inclusion of electrical components in the integrated systems without the fear of EMI issues. By following the EM regulations, the sensitive equipment is nearly out of risk of exposer from the EM radiation [11].

2.3 Definition of Electromagnetic Interference (EMI) Shielding

Electromagnetic interference (EMI) shielding can be defined as an incident where a wide frequency range of EMI pollution as a form of the wave is completely or partially blocked by an obstruction constructed of conductive materials which often refers to absorption or reflection of EM waves by shielding materials [12, 13]. According to Chung et al, it also refers to the reflection and/or adsorption of EM radiation by material which acts as a shield against the penetration of the radiation through the shield. And EMI shielding is different than magnetic shielding which dictates the shielding of the magnetic field at low frequencies [14]. Multifunctional properties of polymer composite materials have been showing their importance in aerospace, military, automobile, chip packaging, and other energy applications [15-17]. It also refers to the attenuation of EM waves using electrical conduction materials or material containing electric and magnetic dipoles. The material should possess electrical conductivity and magnetic characteristics in nature[18]. The EMI shielding effectiveness can also be defined as the ratio of transmitted power (P_t) to incident power (P_I): [19, 20]

$$\mathrm{SE_{total}(dB)} = -10 \log \frac{P_t}{P_I} \quad (1)$$

Composite materials having a higher thickness and electrical conductivity will give higher EMI shielding[21]. EM theory provides that high-frequency EM waves can only penetrate

a small thickness of electrically conducting material, known as the skin effect. It is defined by a depth at which the field intensity decreases to 1/e of the incident EM wave [22].

$$SE_A = 8.68\frac{t}{\delta} \tag{2}$$

$$\delta = \left(\frac{2}{\mu_r \omega \sigma}\right)^{\frac{1}{2}} \tag{3}$$

The EMI shielding material should possess some properties such as electrical conductivity(σ), magnetic permeability(μ), dielectric permittivity(ε), and the thickness(t) of the shielding material. Some of the relations are shown to understand the relationship between material properties on the major shielding mechanisms. It's unlikely to find all the properties at once in an individual material to perform as an efficient EMI shield that attenuates EM radiation by absorption [23].

2.4 EMI Shielding Mechanism

The total shielding consists of the reflection loss (SE_R), the absorption loss (SE_A), and the multiple reflection loss (SEM). The performance of the shield material is expressed in terms of total shielding effectiveness (SET). It is the summation of reflection, absorption & multiple reflection mechanisms shown in the following equation.

$$SE_T = R + A + MR \tag{4}$$

Shielding Effectiveness can also be defined by

$$SE_{total}(dB) = 20d\left(\frac{\mu_r \omega \sigma}{2}\right)^{\frac{1}{2}} \log_{10}(e) + 10\log_{10}\left(\frac{\sigma}{16\mu_r \omega \varepsilon_0}\right) \tag{5}$$

$$SE_A(dB) = 20d\left(\frac{\mu_r \omega \sigma}{2}\right)^{\frac{1}{2}} \log_{10}(e) \tag{6}$$

$$SE_R(dB) = 10\log_{10}\left(\frac{\sigma}{16\mu_r \omega \varepsilon_0}\right) \tag{7}$$

Where d is the thickness of the sample (cm), σ is the electrical conductivity (S/cm), μ_r is relative magnetic permeability, **ω** is the angular frequency, ε_0 is the dielectric constant of vacuum, and e is 2.718 [19-21, 24].

The following equations show the relationship between the material properties on three major shielding mechanism.

$$R = 20\log_{10}(0.0997\sqrt{\frac{\sigma}{f\mu_r\varepsilon_0}}) \quad (8)$$

$$A = 0.017258t\sqrt{f\mu_r\sigma} \quad (9)$$

$$MR = 20\log(1 - 10^{-\frac{A}{10}}) \quad (10)$$

Most of the EMI shielding materials stem from reflection and may result in secondary EMI pollution. So, it is necessary to develop material possessing good absorption quality. The EM radiation absorption material can be classified into two types: dielectric loss and magnetic loss materials [18].

2.4.1 Absorption

The absorption is generally considered for secondary EMI shielding mechanism. The shielding materials should have electric or magnetic or both dipoles which interact with EM radiation [14]. The absorption loss is defined as the attenuation due to dissipation of EM waves inside the shielding where electric and magnetic dipoles interact with EM waves [22, 25]. The absorption loss is a function of the product of electrical conductivity(σ_r) and relative magnetic permeability (μ_r) [14]. The complex permittivity ($\varepsilon=\varepsilon' - j\varepsilon''$)and permeability ($\mu=\mu' - j\mu''$) needs to be measured where the real part ε' and imaginary part ε'' of complex permittivity signify the electric field energy capacity and of dielectric loss ability respectively, while the real part μ' and

imaginary part μ″ of the complex permeability symbolize the magnetic field energy storage and magnetic loss-ability [22, 26, 27].

Dielectric tangent loss, $\tan\delta_E = \frac{\varepsilon''}{\varepsilon'}$ and magnetic tangent loss, $\tan\delta_M = \frac{\mu''}{\mu'}$ are used to evaluate the EM attenuation loss inducing the properties of EM microwave absorption[26, 28, 29]. Between these two types of tangent loss, the one with the higher value dominates the attenuation of EMW in the frequency range. The absorption is related to free charge carriers and electric dipoles of shielding material[30]. For example, a higher mass/volume fraction of dielectric parts compared to magnetic parts may show a dielectric loss dominant mechanism [27]. Microwave attenuation mainly caused by dielectric loss can be expressed by the following equation:

$$R_L = \log\left|\frac{Z_{in}-1}{Z_{in}+1}\right| \tag{11}$$

Where Zin is the normalized input impedance of the microwave absorption layer which can also be expressed as:

$$Z_{in} = \sqrt{\frac{\mu_r}{\varepsilon_r}}\tanh\left(j\frac{2\pi}{c}\sqrt{\mu_r\varepsilon_r}fd\right) \tag{12}$$

Where f, c, and d denote the microwave frequency, light velocity, and matching thickness of the absorber, respectively. μ_r and ε_r are complex permeability and permittivity [24, 27-29]. The absorption loss increases with increasing frequency. It is proportional to the thickness of the shielding materials [14]. When reflection values are less than -10 dB, it represents that 90% incident EMW could be absorbed by the materials [28, 31]. This incident occurs in the EAB range[27].

2.4.2 Reflection

Typically the primary mechanism of EMI is a reflection in which material possesses mobile charge carriers (electron or holes) interacting with the EM fields in the radiation [14]. The reflection loss may represent enhanced impedance mismatch between air and the solid material containing mobile charge carriers such as free-electron interacting with EM waves [22, 25], which correlates with their conductivity and unique structure [18]. The reflection loss is a ratio of the electrical conductivity(σ_r) and relative magnetic permeability (μ_r) [14]. The EMI SE increases with increased thickness. But the mechanism doesn't increase proportionately and in a similar way. The reflection may increase initially with increasing thickness and tends to increase slightly after a certain thickness, then it becomes constant. In the meantime, the absorption value becomes better due to increased interface areas that interacts with incoming power and dissipate more microwave energy [18]. Most of the popular EM shielding material are mostly based on reflection mechanism but they also cause secondary radiation pollution of EM waves [26]. It is caused by the impedance mismatch between air and the shield and closely related to the mobile charge carriers (electron or holes) [30]. A desirable feature recognized as effective absorption bandwidth (EAB) intensively affects the applicability of microwave absorbing material. According to the definition, a frequency where the minimum RL value of the absorbing material is less than -10dB is called EAB [27, 32]. The reflection loss has an inverse relation with frequency. It decreases with the increasing frequency according to Chung et al.[14]

2.4.3 Multiple Reflection

Multiple reflection (MR) loss is defined by the multiple scattering due to the presence of inhomogeneity within the shield having large surface areas or multilayers [22]. Porous or foam material and a large interface area of composite materials containing filler are a general example of MR shielding materials [14]. MR can reduce overall shielding efficiency if the thickness of the shielding material is smaller than the skin depth, otherwise, it can be ignored if the skin depth is lower than the thickness of the material [22]. MF is also neglected when total shielding is more than 15 dB [15, 26, 30] or shielding due to absorption is larger than 15 dB [19, 24]. MR losses are typically originated from sample microstructural characteristics like numerous mesopores [27].

2.5 Properties of EMI Shielding Materials

The EMI shielding material should possess some properties such as electrical conductivity(σ), magnetic permeability(μ), dielectric permittivity(ε), and the thickness(t) of the shielding material. Some of the relations are shown to understand the relationship between material properties on the major shielding mechanisms. It's unlikely to find all the properties at once in an individual material to perform as an efficient EMI shield that attenuates EM radiation by absorption [23].

2.5.1 Electrical Properties

The electrical conductivity plays a vital role in microwave attenuation [18, 33]. The reflection of EM radiation can be facilitated by enhanced electrical conductivity [18]. The composite having higher electrical conductivity may affect the ohmic loss associated with the energy attenuation through current flow via hoping, conduction, and tunneling mechanism[18,

34]. But the electrical conductivity is not the scientific criterion for shielding. Here, though conduction requires connectivity in the conduction path, shielding doesn't require connectivity. Shielding is enhanced by connectivity [14]. The electrical conductivity of nanocomposites can be calculated using

$$\sigma = 2\pi f \varepsilon''_r \varepsilon_0 \quad (13)$$

Where σ is the electrical conductivity of the material, f is the frequency, ε_0 is the permittivity of the free space, and the value is 8.85×10^{-12} F m^{-1} [35]. According to the EM theory, there is a direct correlation between EM SE and electrical conductivity [19].

Material with poor electrical or magnetic properties, their thickness needs to be large to achieve the desired EMI SE which may sacrifice flexible and lightweight characteristics [22]. At high frequency, the EM radiation inserts only the near-surface region of an electrical conductor which is known as the skin effect [14]. Chung et al. defined that the electric field of a plane wave drops exponentially after it penetrates a conductor with increasing depth into the conductor. The depth at which the field drops to 1/e of the total incident value is called skin depth [14]. The skin depth depends on the conductivity and magnetic permeability which implies small conductive and magnetic properties of the skin depth of shielding materials, thus greater thickness with small skin depth are not necessary [22]. The real part of permittivity enhances with the increase of layers. A high value of complex permittivity can be obtained by increasing the conductivity of microwave absorber according to free-electron theory [26, 36]. But this can be reduced by introducing low conductive NPs such as Fe_3O_4 with increasing testing frequencies [24]. Addition to filler on the conductivity of composite can be calculated using classical percolation power law

$$\sigma = \sigma_o(\emptyset - \emptyset_c)^t \quad (14)$$

Where σ, ϕ, t refers to conductivity, filler loading in volume, and conductivity exponent respectively [23, 37].

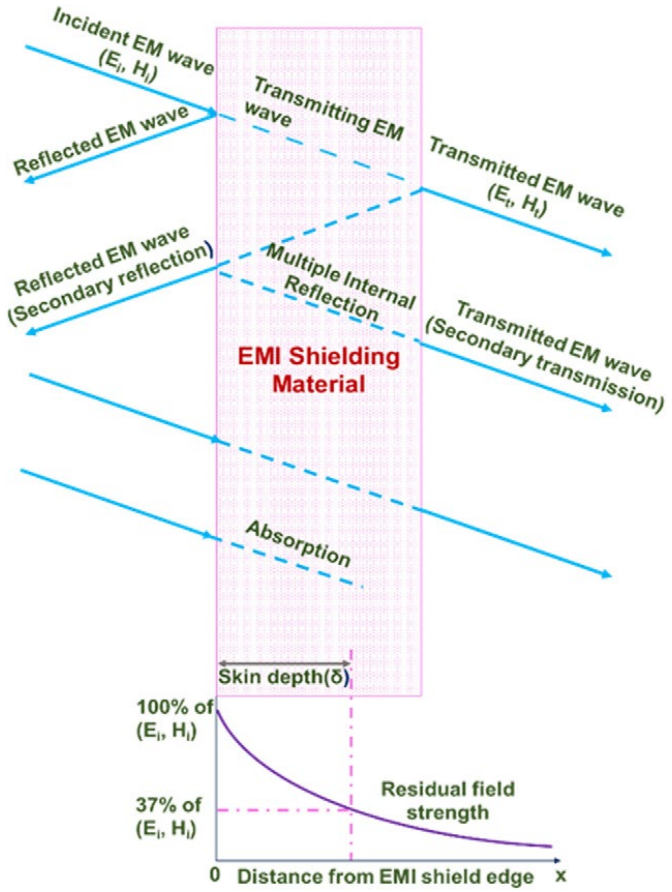

Figure 1: General visualization of Emi shielding mechanism and the skin depth of an EMI shielding material [4]

2.5.2 Dielectric Property

Dielectric loss is mainly attributed to different electronic processes such as electronic displacement, strong space charge, and orientation polarization in the composite [35, 38]. As if the polarization process doesn't affect the dielectric loss, the dielectric loss can be attributed to the conduction loss [24]. But dipolar polarization and interfacial polarization in the presence of microwave can affect the complex permittivity and also contribute to dielectric loss and induce

microwave absorption [26, 39]. According to the Debye theory for dielectrics [29, 32], ε'' is generally known as

$$\varepsilon'' = \frac{\varepsilon_s - \varepsilon_\infty}{1+\omega^2\tau^2}\omega\tau + \frac{\sigma}{\omega\varepsilon_0} \quad (15)$$

Here, ε_0 is the permittivity of a vacuum, $\boldsymbol{\omega}$ is the angular frequency, ε_s is the static permittivity, ε_∞ is the relative dielectric permittivity at the high-frequency limit, τ is the polarization relaxation time, and σ is the electrical conductivity of an absorber). Therefore, the dielectric loss comprises polarization loss and conduction loss. σ is considered as an important factor in the imaginary permittivity. Generally, σ may make an obvious contribution at a higher temperature [39].

The cole-cole semicircle where each part of the semicircle exhibits source of Debye relaxation expressed by the following equation: [27]

$$\left(\frac{\varepsilon - \varepsilon_\infty}{2}\right)^2 + \varepsilon''^2 \left(\frac{\varepsilon_s - \varepsilon_\infty}{2}\right)^2 \quad (16)$$

For example, if the sample has complicated polarization processes, the semicircle will be twisted including several semicircles [27]. The negative value of imaginary permeability means that the magnetic energy originated from the inner EM field due to the motion of charges is converted into electric energy. The magnetic loss which affects the EMWA is caused by the eddy current effects and natural ferromagnetic resonance and exchange resonance [39, 40]. The conduction loss is codetermined by electron hopping and migration within a conductive network of the 3D porous structure. They act as 'material genes' for energy conversion [39]. The debye theory was also expressed as the Debye relaxation process elsewhere to understand the effect on dielectric loss due to the polarization process [24].

2.5.3 Magnetic Property

The magnetic losses contain domain wall resonance, eddy current, exchange resonance, and natural resonance that emerged from the relaxation process during magnetization. The domain wall resonance only exists in low frequency which is less than 2 GHz [28, 41]. Magnetic loss of nanoparticles is caused by two main mechanisms which are magnetic hysteresis and eddy current [42]. When the skin depth is larger than the size of nanoparticle D, then the eddy current loss can be expressed as: [42, 43]

$$\frac{\mu''}{\mu} \propto \frac{\mu f D}{\rho} \tag{17}$$

Where f is the EMW frequency, ρ is the electric resistivity of NPs. Eddy current loss is dependent on the electrical conductivity [35]. The eddy current can be calculated from complex permeability [27]

$$C_0 = \mu''(\mu')^{-2} f^{-1} = 2\pi\mu_0 d^2 \sigma \tag{18}$$

C_0 would be held constant when the frequency is changing [28] if eddy current losses are considered a single source of magnetic losses of the sample. This is a criterion of skin-effect. Here, d is the thickness, μ_0 is vacuum permeability [27]. The electrical conductivity allows the flow of eddy current caused by magnetic field enhanced by magnetic component leading to absorption mechanism of radian [19, 44].

The saturation magnetization of samples containing Fe_3O_4 was less than the pure Fe_3O_4 due to the presence of 3D CF. With the increasing loading content of Fe_3O_4 NPs, the saturation magnetization can be enhanced [24]. The initial permeability (μ_i) can be expressed by the following equation:

$$\mu_i = \frac{M_s^2}{a\kappa H_c + b\lambda\xi} \tag{19}$$

Where a and b are constants of materials, κ is a proportionality coefficient, λ is the elastic strain parameter, and ξ is magnetostriction constant. The permeability can be improved by increasing M_s or decreasing H_c. The H_c has proportionality to magnetic NPs loading [24].

The real and imaginary part of permeability represents the store and dissipation of electric energy, and the real and imaginary part of complex permittivity describes the store and dissipation of magnetic energy [28, 29, 35]. The attenuation constants explaining impedance matching can be well described by the following equations:

$$\alpha = \frac{\sqrt{2}\pi f}{c}\sqrt{(\mu"\varepsilon" - \mu'\varepsilon') + \sqrt{(\mu"\varepsilon" - \mu'\varepsilon')^2 + (\mu'\varepsilon" - \mu"\varepsilon')^2}} \quad (20)$$

The porous structure could tune permittivity and is beneficial to impedance matching. Maxwell-Garnett (MG) theory has been shown:

$$\varepsilon_{eff}^{MG} = \varepsilon_1 \frac{(\varepsilon_2+2\varepsilon_1)+2p(\varepsilon_2-\varepsilon_1)}{(\varepsilon_2+2\varepsilon_1)-p(\varepsilon_2-\varepsilon_1)} \quad (21)$$

Where ε_1 and ε_2 is the dielectric constant of the solid and air, p is the volume fraction of the air in the materials. When ε_1 is greater than ε_2 ($\varepsilon_2 \approx 1$). Increasing pore volume may increase the value of p which causes a decline of the effective permittivity [28]. Under the condition of negative imaginary permittivity, with the long-range connectivity generated among the CNFs due to percolation, a large number of charge carriers are accumulated at the interfaces between conductive CNFs and non-conductive polymer matrix exhibiting strong interfacial polarization [35].

If the permittivity has an inverse relation with the frequency, they are favorable for low frequency and wide-band microwave absorption [29]. Bayat et al. mentioned some magnetic parameters such as remnant magnetization (M_r), saturation magnetization (M_s), and coercivity

(H_c) and their variation with the magnetic phase of magnetic NPs loading in the polymer matrix [19]. The permanent magnetization that occurred in strong applied fields results in the formation of hysteresis losses. The losses of domain wall resonance are observed in magnetic materials with multi-domain structures in less than GHz frequencies [27, 45]. Hysteresis loss is caused by the single domain nanoparticles with large effective anisotropy. The nanoparticle's size which doesn't exceed 128 nm remains in the single domain region [19]. As the interaction between the conductive network and EM radiation increases with increasing thickness, this leads to better shielding performance [19]. Another type of loss called natural-resonance losses in a sample at GHz frequency range can be obtained from nano dimensions of as-prepared magnetic nanoparticles [27]. Natural resonance losses can be expressed as following equation: [27, 45]

$$2\pi f_r r H_a \tag{22}$$

$$H_a = \frac{4|K_1|}{3\mu_0 M_s} \tag{23}$$

Where r is a constant related to gyromagnetic property, H_a is the anisotropic energy, and $|K_1|$ is the anisotropy's coefficient.

2.6 EMI Shielding Materials

Considering the attenuation principle, shielding materials are two types: wave-reflection dominant materials and wave-absorption dominant materials. Metal is generally wave-reflection dominant materials having enormous mobile charge carriers that interacts with the electric vector of incident EM radiation. Wave absorption dominant materials consist of magnetic materials such as carbonyl iron and ferrites [46-49], dielectric materials such as barium Titanate [46, 50]. It has been reported by Jiang et al. [4] that conductive polymer composite has their enhanced EM

absorption due to their segregated structure [51], double percolation structure [52], layer-by-layer assembly [53], multilayer structures [54], foam structures [55].

The precise understanding of the shielding function of the “sandwich” structure has been described by Fei et al. They prepared C-MIL-88B/GNP composite film to explain the properties. The BMWs strike the surface of the multilayer film, the C-MIL-88B NP in the film surface derived magnetic component, and graphitic carbon induces a strong loss against absorbing and attenuating BMWs. Because of the magnetic and considerable conductive property of the C-MIL-88B film, it acts as a suitable impedance matching to reduce EMW reflection. The penetrating waves imping the high conductivity layer of CNP which promotes EM conversion to generate current and induces an Ohmic loss in the energy of BMWs. The remaining EMWS encounter the C-MIL-88B and GNP interface, therefore, energy dissipation occurs due to the simultaneous existence of electric and magnetic phases in the interface inducing interfacial polarization and relaxation. At the same time, internal scattering and MF happens in the reflected surface when an EM wave strikes a highly conductive layer. Then the remaining EMWs go through another magnetic layer and induce further magnetic loss. The attenuation of EMWs repeats the same absorption technique as the EMWs pass more layers. Eventually, they are completely absorbed by the multilayer composite films [26]. As the dielectric loss component is more significant than the magnetic loss for microwave absorption, porous CNF with magnetic NPs is expected to provide superior microwave absorption [35].

2.6.1 Polymers used in EMI Shielding

Polymers are preferred due to their lightweight, corrosion resistance, low cost, flexibility, electrically insulated characteristics [23]. Polymer-based materials using thermoplastic polymer such as polyurethane(TPU) [16], poly (vinylidene fluoride) [18], Polymethylmethacrylate

(PMMA) [35], Poly-dimethylsiloxane (PDMS) [17, 30, 35], polyacrylonitrile (PAN) [29]. Highly permeable, moderate conductivity of polymer composite having both conductive and magnetic filler makes them good EM absorber [23]. Besides, The pyrolysis process converts the as-spun nanofibers such as PAN into electrical conductive carbon nanofiber [19]. Nanoporous carbon composite having a high surface and effective porosity can provide more active sites for reflection and scattering of microwave [26]. There is an inverse relationship between electrical conductivity and surface area, with increasing surface area due to rising structure defect, the electrical conductivity is reduced [27, 56]. 3D carbon fiber mats(CFM) have a remarkable specific area, porous structure, and lower resistivity compared with conventional carbon fibers [24]. A small number of NPs dispersion in a polymer matrix such as epoxy may present less contribution to electrical conductivity [57]. NPs blended with epoxy resin has been investigated for EMI shielding performance [25]. The EME SE of the epoxy-based composite has proportionality with the sample thickness. This can be attributed to the reduction of the transmitted portion of the received microwave from the rear of composite owing to placing additional wave attenuative component in front of the incident EM waves with the increasing thickness of the composites [27]. Electrical percolation of nanocomposites is affected by parameters such as molecular weight, crystallinity, surface tension, and polarity of the polymer. With higher surface tension with higher filler loading, percolation threshold can be reached. The higher the surface tension of the polymer, the lower the polymer filler interfacial tension, thus polymer can wet nanofillers. Good wetting leads to better dispersion of the nanofillers within polymer matrix which improves the filler loading to reach percolation threshold [35, 58].

2.6.2 Metals

For EMI shielding, metals are commonly used as they function mainly by reflection due to free electrons in them [14]. Bulk metals had been highly used in the past as EMI shielding materials as they possess high conductivity and dielectric constant [59]. But, they are likely to be suffering from various drawbacks such as corrosion, complex fabrication technique, high density, reflection dominant mechanism [23]. The electrical conductivity of the composite containing carbonaceous nanoparticles (NPs) is not very high compared to metals if the free electron is not present on the surface. Therefore, the reflection of EM waves from the surface will be small while attenuation of inserted EM waves would be higher [18]. Even though bulk metals such as silver, copper, gold, Aluminum, etc. provide superior conductivity and EMI shielding performance [12], they are susceptible to corrosion, wear, and scratch [4, 14], adding weight [60] to garment making them uncomfortable to wear [61]. Due to their bulk nature, their coatings are commonly made by electroplating, electroless plating, or vacuum deposition. But the coating tends to suffer from their poor wear or scratch resistance[14]. Carbon Nanofibers decorated with metal or metal oxides show a better microwave absorption than a single component because of interfaces and their associated relaxation loss [24, 35, 62]. The polymerization can be performed on various metal coating carbon fiber such as nickel coated carbon fiber(Ni/CF) [63]. Metal NPs such as Copper, nickel etc can be used as a second phase material with conducting polymer composites [4, 64].

Table 2. EMI Shielding Effectiveness (SE) at 1-2 GHz of polyethersulfone (PES)-matrix composites with various fillers[12]		
Filler	Vol.%	EMI shielding effectiveness (dB)
Al flakes ($15 \times 15 \times 0.5$ μm)	20	26
Steel fibers (1.6 μm dia.$\times$ 30~56μm)	20	42
Ni Particles (1~5μm dia.)	9.4	23
Ni fibers (20 μm $dia.\times 1\ mm$)	19	5
Ni fibers (2 μ$m\ dia.\times 2mm$)	7	58
Ni filaments (0.4 μ$m\ dia.\times >$ 100μm)	7	87

2.6.3 Intrinsically Conducting Polymer (ICPs)

Conductive polymers are attractive candidates since they have been discovered in 1977 [65]. Adding conductivity to fabrics depends on coating or embedding the fabric with a conductive material such as metal [61]. Organic conductive polymer(CPs) embedded on fabrics has been reported to improve electrical properties such as reducing sheet resistance [61] but lesser shielding efficiency [60] to fabrics. They have potential application in energy storage, optoelectronic devices, textile technology [61] electrochromic, organic photovoltaic. They provide Magnetic, optical, and electronic properties and retain the processability and flexibility of conventional polymers. It becomes a great interest of research on enhancing dielectric properties, thermal durability [66-68], solvent penetration, processability than synthesizing other polymeric material [69]. Polyacetylene (PaN), polyaniline (PANI), Polypyrrole (PPy) etc has been studied extensively in EMI shielding applications except for polyindole (PIn). Investigations are being undergone on electrical conduction, dielectric behavior with varying

temperature and frequency [70]. They sometimes are considered ‘synthetic metals’, often known as π-conjugated conducting polymers due to having a conjugate network with delocalized pi electrons [67] and possesses the ability to merge with semiconductors [67], metals with mechanical and chemical properties of polymers or metal to semiconductor transitions [61]. Besides, EMI shielding application, they draw great attention to antistatic coating, compact capacitors, smart windows, corrosion protection [66], actuators, chemical sensors, polymer batteries [71]. They can show the simultaneous physical and chemical properties of organic polymers and electrical characteristics of metals [71] by making conducting an electrical pathway [61]. The electrical conductivity depends on the reaction parameters during polymerization. For example, the longer the reaction time of the polymerization, the greater the amount of conducting polymers with increasing conductivity [4, 72]. The movement of charge carriers in the ICP backbone can be restricted by the presence of metal oxides at the interface. As the charge accumulates, there is an improvement in capacitance of ICP/metal oxide composites leading to an increase of the dielectric constant [4]. The mobile charges (polarons and bipolarons) and bound charges (dipoles) at the ICP backbone can promote EMI shielding ability (both reflection and absorption) [4, 73]. The polymers have their limitations sometimes such as insolubility and infusibility of PPy may restrict its fabrication and show poor mechanical properties [59, 74].

2.6.4 Carbonaceous NPs incorporated Composites

The metal or carbon-based materials are used heavily due to their great mechanical strength and electrical conductivity at low percolation [46, 75, 76]. Carbon Nanofibers decorated with metal or metal oxides show a better microwave absorption than a single component because of interfaces and their associated relaxation loss [24, 62]. Density, solid volume fraction, and

electrical conductivity are the structural parameters of CNF that played important roles in high-performance EMI materials [24]. EM shielding material may present multifunctional and interactive new generation structure blocks low-density radiation and microwave radiation to protect electronic equipment from signal loss[13] or to separate internal electronics from the surroundings[46]. The conducting polymer composites made from carbon nanostructures (CNT, CF), pristine graphene(G), graphene oxide(GO), reduced graphene oxide(rGO) filled within an insulating polymer matrix provide excellent performance for EMI shielding [16] due to their lightweight, excellent shaping capability, reducing weight, chemical stability, design flexibility advantage [18, 26, 77]. Micro-sized CFs are widely used conductive additives due to their great mechanical, electrical, and numerous source [22]. As a dielectric component, carbon-based nanofiller can be used within a polymer matrix but these carbon-based nanofillers require relatively complicated processing with a high production cost [46]. Higher filler loadings would be an easy strategy to enhance the EMI SE of composites [16]. But the drawback of high filler loading promotes large weight density for composite materials [39]. Electron movement at gaps causes its conductive characteristics where conductivity is highly anisotropic. As it has a semi-crystalline structure, the conductivity also depends on the bridge formation along the crystalline and amorphous regions. Then the tunneling of charge carrier happens between conductive and non-conductive regions [13, 78]. Expansion of new fabrication techniques minimizes its substandard reaction control and processability sorted by typical morphology while leading to the higher surface area, solvent processability, controlled morphology, corrosion resistance, the formation of conducting pathways [60]. The non-magnetic nature of CFs and CNTs can show secondary EM pollution as they are not so efficient in high-performance absorption [27]. But the carbon nanostructure has a lightweight, well-regulated aspect ratio, and flexibility that

compensate for the performance of absorption [4, 73]. Multiwalled CNT(MWCNT) can provide interconnection between ICP grains coated on MWCNT while increasing coherence, the coupling between the chains, and interchain transport, thereby improve electrical conductivity[4, 79]. Enhanced adhesion of well-oriented functionalized CNTs such as fluorinated CNTs in PANI fiber was shown to provide an improved EMI shielding mechanism [80].

2.7 Properties

2.7.1 Properties of Nylon 6

Nylons were first introduced to the market in the late 1930s. A part of a family of synthetic polymers termed as "nylon" was first produced in 1935 by Gerard J. Berchet of Wallace Carothers' research group at Dupont in Delaware [81]. About 1939/1940 nylon 6 fibers were developed by I.G Farbenindustrie in Germany [82]. Due to its good mechanical properties and smooth fiber like skin, it is widely used as plastic and synthetic fiber [83]. It has a glass transition temperature of 47^{o}C and melting point of 220^{o}C and a density of 1.13 g/cm^{3}.

Nylon is a term used to describe a family of organic polymers called polyamides containing the amide (-CONH) group. Nylon 6 is made by polymerization of aminocaproic acid ($H_2N(CH_2)_5COOH$) having blocks of methylene ($-CH_2$) groups joined by amide (-CONH) groups [81]. A wide variety of techniques such as electrospinning, wet spinning, Forcespinning® have been used to synthesize nylon 6 [84-86]. Depending on collecting speed, thermal treatment, and thermo-mechanical history, the synthesized Nylon 6 fibers have two common crystalline forms, the thermodynamically stable α form and the less stable γ form [87]. Some process conditions such as temperature, take-up speed, humidity, and molecular weight may control the structure of the as-spun nylon 6 fibers [84]. It has been reported that take-up speed has proportionality with a uniform increase of young modulus of fiber. γ formation became

predominant speed up to 9 km/min. α form occurred between 9-12 km/min with an increase in crystal perfection [88]. γ-phase nylon crystallites with the layer normal parallel to the fiber axis are mostly found in all the electrospun products [84].

Dielectric relaxation spectroscopy and Differential Scanning Calorimetry (DSC) of nylon-12 with 30% crystallinity show that it's annealing below the melting point results in crystallization to the phase associated with a change in its electrical properties. The phase transformation increases the dc conductivity and decreases the contribution to its orientation polarization without altering the shape of the relaxation spectrum. Above the glass transition temperature (Tg) of the partially amorphous phase, two processes were observed which could be responsible for total orientation polarization in nylon-12 [89]. Nylon 6's higher adhesion and excellent insulation properties made it a suitable candidate for surface modification in developing microwave absorbing material. But the insulative nylon membrane may suppress permittivity by increasing resistivity and prevent the formation of an electrical conduction path[90]. With chemical oxidative polymerization (COP), conductive textile fabrics have been prepared using non-conductive nylon 6 matrix [59, 91]. As the activation energy for nylon 6 is less, it makes it less cooperative compared to other polymers. The conduction in nylon includes ionization of N-H bonds and greatest in the direction of hydrogen bonding [92]. The ultrafine structure provides a tunneling current which can be related to the existence of negative differential resistance (NDR) in nylon 6 nanofibers [93]. Fiber diameter has effects on pore size, Brunauer-Emmett-Teller (BET), surface area, and gas transport property of nylon 6 nonwoven mats [83]. It has excellent compatibility with acid-chloride modified single-walled CNTs (SWCNTs) to form nylon 6 grafted-SWCNTs [94, 95].

Table 3. Summary of properties of Nylon 6			
Property	value	Units	Ref
Repeating Unit	(-NH-CH_2-CH_2-CH_2-CH_2-CH_2-CO-)	N/A	[96]
Chemical Formula	$(C_6H_{11}NO)n$	N/A	[96]
Glass transition temperature	47	ºC	[96]
Melting temperature	220	ºC	[96]
Autoignition Temperature	434	ºC	[96]
Density	1.13	g cm^{-3}	[97]
Amorphous Density	1.084	g/ml	
Refraction Index	1.53	N/A	[97]
Water Absorption	0.300-7.00	%	[98]
Moisture Absorption at Equilibrium	1.00-3.00	%	[98]
Ultimate Tensile Strength	50-90	MPa	[98]
Tensile Yield Strength	40-100	MPa	[98]
Compressive Yield Strength	6-162	MPa	[98]
Creep Strength	6-24	MPa	[98]
Modulus of Elasticity	1.3-4.20	GPa	[98]
Coefficient of Friction	0.04-0.6	N/A	[98]

Electrical Resistivity	10^{12}-10^{15}	ohm-cm	[98]
Surface Resistance	10^{10}-10^{13}	ohm	[98]
Dielectric Constant	3.10-12.0	N/A	[98]
Dielectric Loss Index	0.012-0.14	N/A	[98]
Thermal Conductivity	0.230-0.342	W/m-k	[98]
Upper working temperature (C)	80-160	^{o}C	[97]

2.7.2 Properties of Polyacrylonitrile (PAN)

The polymerization of acrylonitrile had been familiar since the 1890s. The commercial production of PAN fiber did not start until the 1940s after Ray C. Houtz of E. I du Pont de Nemours & company discovered a spinning solvent that could dissolve the polymer [99]. In 1930, Hans Fikentscher and Claus Heuck first synthesized it in the Ludwigshafen works of the German chemical conglomerate IG Farben [100]. In 1938, Herbert Rein spun the first fibers based on PAN using aqueous solutions of quaternary ammonium sodium thiocyanate and aluminum perchlorate for the production process with other solvents including dimethylformamide (DMF) [101]. Though carbon fibers are generally obtained from acrylonitrile copolymers [102], PAN has been a widely used precursor for producing high-performance carbon fiber [103]. 90% of carbon fiber is produced from PAN [104]. The presence of polar nitrile groups at an intramolecular distance of a few tenths of an nm provides the dominant characteristic of the PAN molecule [105]. It has been reported that PAN has excellent barrier properties due to its relatively high permeability to helium and low activation energies for permeation. The rate-determining transport step for fixed gases in and through this particular

polymer can relate to the small size of the fluctuating free volume elements [106]. The effects on the properties of PAN precursor and its resultant carbon fiber such as obtaining great mechanical properties providing good relation between tenacity and modulus of PAN fiber by different contents of comonomers have been reported [103] such as methacrylate, methyl methacrylate, vinyl acetate, etc [102]. Carbon fiber derived from a PAN-based precursor heat treated to between 1000ºC and 2800ºC had been examined to investigate the change in resistivity, thermoelectric, and magnetoresistance with some fundamental structural change. The formation of graphite-type crystallites within the carbon-fiber structure during processing temperature around 1750ºC which helped to provide systematic explanation of electron spin resonance (ESR). The resistivity of graphitizing carbons is higher than carbon fibers in lower heat treatment temperature. The lower resistivity of carbon fibers can be associated with the preferential alignment of graphitic crystallites along the fiber axis. Also, the nominal non-graphitizing nature may offer these fibers with favorable mechanical properties owing to their industrial importance, ease of experimental manipulation, thus, making it a good candidate for experimentation[107]. The properties of CF can be improved by increasing the molecular weight of PAN precursor which plays a role in the glass transition temperature, exotherm temperature. Also, the spinnability, crystal size of PAN fiber increases with polymer concentration and molecular weight while decreasing the pore diameter [108].

The range of glass transition temperature (Tg) of PAN varies from 80 to 100ºC[102, 109]. DMA analysis of Tg of unoriented samples exhibited two main mechanical-loss peaks in the range of 90-100ºC and 140-170ºC[102, 110]. Two Tg can be represented by two relaxation peak which describes two types of intermolecular interaction such as van der Walls forces (transition at 90º) and dipole-dipole interaction between polar nitrile groups (transition at 140ºC)

[102, 110, 111]. The dipole-dipole interaction of nitrile groups had been interpreted in terms of low molecular weight model by Henrici-Olive et al. The fiber response to stress (such as elongation of fiber up to 40%) mechanism can be explained in the temperature below Tg. The other mechanism of stress response becomes available in temperature above Tg. When the PAN fibers or films are under sufficient stretching, individual untwisted macromolecules may be packed side-by-side and bonded by intermolecular dipolar interactions [105].

Some literature reported that PAN fibers are not categorized as crystalline [102, 112-115] but have paracrystalline ordering [102, 116, 117]. Its structure was described as 'laterally ordered' [102, 114, 115] or condis-crystal structure [118]. Kalashnik et al. reported that it can form one or two phases having ordered mesophase or amorphous phase respectively. They investigated the mechanism of molecular motion in PAN fibers using DMA and TMA methods [102].

Table 4. Summary of properties of Polyacrylonitrile (PAN)

Property	Value	Units	Ref
Chemical formula	$(C_3H_3N)_n$	N/A	[119]
Density	1,184	g/cm^3	[119]
Glass transition Temperature	~95	°C	[120]
Melting point	300	°C	[119]
Boiling point	Degrades	°C	[119]

Solubility in Water	Insoluble	N/A	[120]
Solubility Parameters	26.09 (25ºC)	$\sqrt{MPa}$	[119]
Dielectric Constants	5.5 (1 kHz,25ºC), 4.2 (1 MHz,25ºC)	N/A	[119]

2.8 Enhancing the EMI Shielding Performance

Most of the EMI shielding material stems from reflection and may result in secondary EMI pollution [18]. EM wave absorbing materials suffer from narrow bandwidth, weak absorption, thick matching thickness, and high density[28]. To achieve the desired ability to exhibit desired absorptive losses, the material should possess high magnetic permeability, good electrical conductivity [23], large internal surface area to improve impedance matching [17, 21, 22]. The 3D porous structure could improve impedance matching while reducing reflectivity and enhancing multi-interface for on the materials [42]. Due to the inverse relation between electrical conductivity and surface area [56], it can be attributed to CFs for its high electrical conductivity that the reduction of electrical conductivity can help to increase impedance matching between nanocomposite structure and incident EM wave [27]. Due to high density, brittleness, poor environmental adaptability, magnetic, and ferrites were restricted extensively on the application of conventional EMI shielding materials [24]. The absence of magnetic properties for CFs restricts their application in which absorption loss plays a pivotal part to avoid secondary mechanism [22]. The impedance mismatch between free space and the shield caused due to high electrical conductivity results in a strong reflection of EM wave while high absorption is less likely to occur [22]. High complex permittivity and low permeability could cause impedance

mismatch easily while limiting the application of the pure carbon materials in EM wave absorbing materials [28]. Dielectric and magnetic loss materials generally fall into the category of EM absorption materials [18].

2.8.1 Magnetite (Fe_3O_4) doping

Incorporating of superparamagnetic NPs may induce EM loss, dielectric loss from interface polarization [16] and enhance complex permittivity and complex permeability[22]. The chemical formula of Fe_3O_4 is $Fe^{3+}{}_A\,[Fe^{2+}, Fe^{3+}]_B O^{2-}4$, where Fe occupy interstices of a face-centered cubic closed packed frame of oxygen ions, and A and B denote the tetrahedral sites and octahedral sites, respectively [29, 121]. So, the possibility of polarization would include electronic displacement polarization and space charge polarization while the charge would also gather in the interfaces between NPs and NFs [29, 122]. It also generates defects which are beneficial in absorbing microwave energy [35, 122]. The addition of these NPs increases the permeability and magnetic loss of the absorber [28]. The shielding performance of any composite material highly depends on the intrinsic properties of its filler [19, 123]. Fe_3O_4 NPs increase graphitization degree as well as conductivity of NF due to catalytic graphitization effect [29, 35]. Fe_3O_4 possesses great magnetic and dielectric properties, thus made it a favorable candidate for magnetic attenuation sources in EMI shielding composites [24]. It has additional exceptional features such as uncomplicated, inexpensive fabrication, strong spin polarization, high magnetic losses, non-toxicity [27]. Important parameters such as controlled shape, dispersion of NPs, and the matching between magnetic and dielectric components were key factors [24]. Fe_3O_4 has inexpensive, less toxicity, good biocompatibility, and great wave absorbing properties [18, 21, 29, 57]. It can also improve thermal stability, the flame retardant property of polymer matrix[124]. The effect of the impedance matching may cause abundant

interfacial polarization and increased magnetic loss resulting from Fe_3O_4 NPs [18, 125]. The variation of enhanced surface area, number of dangling bond atoms, unsaturated coordination on the surface of the particles in nanometer size range lead to interface polarization and multiple scattering, thus provide absorption EM radiation [19, 123, 126]. But, the instability, ease of oxidation, and intrinsic weakness may restrict the practical applications of Fe_3O_4 [32, 39]. It also has the advantages of high magnetism, eco-friendliness, rich mineral reserves [30]. It were widely used in magnetic resonance imaging, photocatalysis, drug delivery, adsorption, etc. [24]. Magnetic materials have better MW attenuation properties at lower frequencies [27, 127]. Pure single-phase carbon-filled nanocomposite has a limitation of EM absorption due to less effectiveness of magnetic hysteresis loss effect [18]. Without conductive filler, this material is not as effective as it may seem [19, 21]. It is not an optimal solution to build only a high conductive network to design ideal EM shielding material [26, 128]. The NPs tends to aggregate in the polymer matrix as it has strong magnetic particle interaction [22]. The presence of this nanoparticle can prevent the skin effect of conductive materials allowing easy penetration of EM waves [21, 129].While the techniques of incorporating filler have them the limitation of the increase of filler loading in EMI SE materials, some studies focused on the orientation of filler such as Hong et al. investigated on magnetic responsive filler materials portraying higher EMI(250%) of in-plane aligned composite over randomly oriented composite using Fe_3O_4 NPs with reduced graphene oxide(RGO) via solution casting method coupled with or without external magnetic field[16]. Reduction of GO cannot retain pristine properties of graphene [23, 130]. Fe_3O_4@GNP hybrid nanostructures were synthesized in situ by co-precipitation technique where GNPs is termed as intermediate between graphene and graphite [23]. The hybrid nanoparticles doesn't exhibit a percolated electrical network even though the content loading is above

percolation threshold for GNP epoxy system [23]. Cellulose/rGO/ Fe_3O_4 aerogels prepared from the co-precipitation process shows strong EM absorption resulting from multireflection of microwave and impedance matching with increasing sample thickness [21]. PVDF/ Fe_3O_4/carbon films were prepared via solution processing and compression molding. The large interfacial area given by Fe_3O_4 and GNPs is responsible for enhanced microwave attenuation. Shielding by absorption increased from 64 to 83% with an addition of Fe_3O_4 due to its magnetic property including natural resonance and eddy-current loss [18]. Chen et al. showed increases of conductivity and decrease of the skin depth with increasing Fe_3O_4 NPs loading by homogenously dispersed Fe_3O_4 in the epoxy matrix after surface modification by using silane coupling agent to improve the dispersion and enhance compatibility. The CF veil is impregnated with NPs/epoxy via a vacuum bagging process. The multilayer construction of the CF veil favors multiple reflections as the incident wave is multiply reflected and scattered many times by layered architecture. The layered structure increases the propagation path of waves in the multiscale composites which interacts with magnetic particles frequently thus increasing the absorption loss. At constant frequency, the complex permittivity increases with NPs loading. Complex permeability also increases with NPs loading along with matching of input impedance which may decrease surface reflection. The skin depth decreases with increasing NPs as microwave conductivity and complex permeability also increases [22]. In-situ growth of hollow Fe_3O_4 sphere on three-dimensional graphene foam (GF) surface filled with PDMS was fabricated to investigate thermal interface materials (TIM) for chip cooling. 22 dB enhancement occurred by loading of GF/h- Fe_3O_4 up to 12 wt%. The generation of localized currents in conductive interconnected GF networks where the polarization/relaxation process of dipoles and free charges at the interface of graphene and Fe_3O_4 takes place. The energy dissipation happens due

to the inner/outer surface of h- Fe_3O_4 which causes absorption attenuation as a dominating mechanism [17]. The synergistic effects of dielectric, magnetic loss and multilayer structure have given improved microwave absorption and attenuation properties for metal-organic frameworks (MOFs) derived Fe_3O_4 carbon-based materials and GNPs via filtration assisted self-assembly method [26]. Random stacking of few-layered structure is performed using cellulose nanofiber (CNF) because of its sustainable nature and colloidal stability [26, 131]. Fe_3O_4/thermally annealed graphene aerogel/epoxy nanocomposites (Fe_3O_4)/TAGA/epoxy) were prepared by ethylenediamine functionalized Fe_3O_4 (NH_2- Fe_3O_4) NPs and GO followed by addition of L-ascorbic acid via template-casting method. Thermal annealing treatment can remove most of oxygen containing groups [57]. Three-dimensional Fe_3O_4/carbon micro-flowers has been prepared by simple hydrothermal method with subsequent calcination step. The synergistic effect of Fe_3O_4 and carbon combined with a hierarchically porous and 3D structure showed strong and tunable EMW absorption performance. The filler loading showed remarkably great EMWA performance. The porous structure is responsible for the resonance due to many sites, e.g., pores, interfaces and defects, serving as polarization centers. Magnetic loss, conduction loss due to Fe_3O_4 and Carbon respectively along with porous structure offered excellent EMWA performance [39]. Polyvinyl alcohol/ Fe_3O_4 fibers were prepared by magnetic electrospinning process to manufacture partially aligned nanofiber. The addition of 0.5% wt% Fe_3O_4 NPs improved the alignment of nanofibers. The fiber diameter decreased due to applied magnetic field [132]. Fe_3O_4 graphene foam (GF) in PDMS showed excellent shielding even after repeated bending for 10000 cycles. The increasing filler content to build conductive network may lead to difficult processing and poor mechanical properties. Hexadecyl trimethyle ammonium bromide (CTAB) decorated magnetic Fe_3O_4 nanoparticles were used on electronic conductive GF on the

role of mutual electrostatic attraction in the aqueous medium. The NPs have any weakening or strengthening effect on the contact resistance of the fixed shaped graphene in the 3D structural Fe_3O_4/GF composite. The higher temperature than the room temperature is used to increase the path of CTAB-modified Fe_3O_4 NPs on the surface of GF. The large surface and interfacial area of 3D GF promotes scattering which allows high performance multiple reflection within the material leading absorption dominant EM shielding. It has been shown that uniform distribution of Fe_3O_4 NPs on the GF surface obtained strong absorption to incident EM wave that the Fe_3O_4 in Fe_3O_4/PDMS/PTFE composite. Adding PDMS reduced electrical conductivity of Fe_3O_4/Gf and added density of composite (0.13 gcm^{-3}). These composite manifests synergistic effect between conductive graphene and magnetic Fe_3O_4 NPs in EME SE. Fe_3O_4 didn't have influence on electronic contact of highly conductive graphene sheets, thus the reflection shielding wasn't influenced[30]. 200-250 diameter Fe_3O_4 nanosphere coating was done uniformly on the surface of 3D CNF using surface modification due to a few functional groups on the outside surface. A thin layer formed on the surface of 3D CFM by self-polymerization of dopamine, thus forming abundant -NH_2 and -OH groups on the outside surface of CFM followed by a coating of Fe_3O_4 NPs via solvothermal route. 2.5 mm thickness showed reflectivity of -47 dB at 10 GHz. Further incorporation of Fe_3O_4 NPs into epoxy resin gave 23 dB EMI shielding performance in the range of 8.2-12.4 GHz. It is challenging to develop a reliable synthetic route to prepare structure-controlled and efficient CF/ Fe_3O_4 hybrid EMI materials. The real part of permeability was slightly enhanced due to loading content of magnetite. Dielectric loss is responsible for this microwave attenuation. The well matched magnetic and dielectric loss gave the best result having low reflectivity and low density. Controlled 3D morphology of CF help obtaining good impedance matching allowing EM radiation to enter absorber properly [24]. Bio derived EMW

absorbing material such as porous carbon foam derived from fish skin has been synthesized. The Fe_3O_4 nanospheres were uniformly embedded into the carbon matrix via refluxing and annealing treatment. Bio-derived absorbers suffer from thicker matching thickness which limits their application. Combining carbon materials with magnetic materials could improve the dielectric performance of magnetic materials and the interfacial relaxation between different components become beneficial to the attenuation of EMW. Annealed materials still hold original porous morphology under high temperature which is better for MF and scattering of EMW. Too much Fe_3O_4 could decrease pore volume affecting impedance matching. -52.9 dB at 6 mm and -29.4dB at 6.3mm showed the worst performance due to the excessive Fe_3O_4 loading. It also causes a collapse state and disrupted pore distribution in porous structures due to the accumulation of NPs. The EMW after entering the absorber, it transformed into heat energy through a various forms like interfacial, dipole polarization, dielectric, magnetic loss [28]. Mesoporous CNF and Fe_3O_4 NPs with absorption properties of PDMS has been prepared by co-electrospinning process with a stabilization (250^oC) and carbonization at elevated temperature (900^oC) to investigate mesoporous and hollow CNF. The magnetic moment of any material depends on the number of magnetic domains per unit volume. Long range conductivity is generated among the CNFs due to the percolation. Dipolar and interfacial polarization contributes to dielectric constant of Nanofibers. Electrical conductivity increases with NF and NPs loading. Nanostructured magnetic materials create a more unsaturated bond on hollow CF indicating the existence of large number of dipoles which are responsible for enhanced dielectric loss. Entrapped air within the hollow nanofiber increases polymer filler interfacial tension to achieve great percolation threshold at lower filler loading[35]. Fe_3O_4/carbon composite nanofibers prepared by electrospinning of Polyacrylonitrile (PAN)/acetyl acetone iron (AAI)/dimethyl formamide (DMF) solution followed

by stabilization and carbonization. Raising carbonization temperature can improve electrical conductivity. Catalytic graphitization effect of Fe_3O_4 are better at 800ºC than lower carbonization temperature. Excessive content of NPs may be harmful for the continuity of fiber, hinders the formation of graphite layers. Dispersion condition could be enhanced due to loading of NPs which is beneficial for MWA [29]. Hybrid multifunctional Fe_3O_4/CNF showed absorption dominant mechanism for the contribution of both magnetic and dielectric losses due to incorporation of magnetic NPs with 3 and 5 wt% loading within conducting CNF matrix with aspect ratio structure and randomly aligned NFs. There was an addition of elastomeric PDMS coating to strength its structure and Triton x-100 surfactants was used. Electrospinning process was involved along with stabilization at 250ºC and carbonization at 700 and 900ºC. 600% weight loss was found due to pyrolysis at 900. Firstly, the addition of Fe_3O_4 in the carbon fiber is well-known to enhance the catalytic growth of crystallin graphite during the carbonizing process leading higher electrical conductivity. It also enhanced magnetic parameters such as remnant magnetization (M_r), saturation magnetization (M_s), and coercivity (H_c) and their variation with the magnetic phase of magnetic NPs loading in the polymer matrix. Increasing electrical conductivity minimizes the microwave power transmitted by the shield. The specific nanofibrous structure of NF with a higher aspect ratio and highly porous structure contributes to absorption than reflection [19]. RGO@Fe_3O_4/EP nanocomposite was prepared using electrostatic self-assembly and co-precipitation technique, magnetic reduced graphene oxide (RGO)@Fe_3O_4 Nanoplatelets by applying an external magnetic field to align the Nanoplatelets during epoxy curing. This composite reflects the dominant EMI shielding mechanism[25]. Fe_3O_4@graphene aerogel was prepared via bioinspired by mussel by introducing Fe^{3+}/Fe^{2+} while high hardness and extensibility were achieved by hydroxyl/amine-Fe^{3+} chelation cross-links. Then pyrolysis under

800ºC was performed to provide the desired electrical conductivity but decrease mechanical property. Flower-like Fe_3O_4 was beneficial for dielectric and magnetic polarity [42].

2.8.2 Incorporating Carbon Nanotubes

Several investigations have been performed to produce Carbon Nanotube (CNT) reinforced polymer composites for good electrical and mechanical properties through Forcespinning®. To take full advantage of the superior tensile properties of reinforcements, an optimum interface between the filler and polymer matrix is required to ensure adequate stress transfer. The weak interfacial adhesion between the filler and polymer matrix increases the stress concentration at the filler/polymer interface leading to composite failure. Stress might be transferred from a polymer matrix to filler directly, or through an interfacial layer of polymer that has different characteristics than the bulk polymer. CNT is often bundled together by strong van der Waals interactions between the nanotubes [133]. The mechanical resistance of the mono-component samples is higher than that of the composites containing two types of polymers in different ratios. The presence of the second component caused the inhomogeneity of the samples thus creating a looser and less homogeneous fiber structure of lower tensile strength. Even the presence of halogen in fiber can reduce its mechanical strength by occupying the free volume holes of the polymer bigger than its molecular size [134]. The fiber structure shows buffering effects to mitigate volume changes associated with Si during the alloying/dealloying process [135]. Even lower rpm can result in ductile feature in fiber while higher rpm provides more stiffness and strength due to a more aligned chain in the direction of tension [136]. Weng et al. showed that a high concentration of CNTs in PAN [137], in PMMA [138] can lead to higher tensile strength followed by a step carbonization process. Drying the fibrous mats under a vacuum environment before carbonization is necessary. Adding CNTs can result 210%, 338%,

150% improvement of tensile strength in CNT/PMMA [138], hierarchical CNT-Nylon NFs [86], PVB NFs matrix [133] respectively. Carbonized CNT/PAN fibers show superior improvement in electrical conductivity than only carbonized PAN fibers as the formation of the continuous and well-aligned network by CNTs within the matrix. The limited solubility of CNTs in solvent like Chloroform [138] where dispersion of CNTs is necessary to promote conductivity in CNT based polymer matrices, functionalized CNTs prepared by chemical or physical dispersion method [133] is required to reduce aggregation and enhance affinity to polymers, sometimes acts as plasticizers [139]. Due to fewer CNTs attachment to a hydrophobic polymer such as Nylon NF [86], surfactants like NaCl [140] can be used in polymer to reduce surface tension (contact angel) to decrease hydrophobicity. Increasing surface roughness by incorporating metal oxide particles can improve hydrophobicity. The repel effect of hydrophobicity may occur if the particles disperse in pores, grooves & wrinkles [141]. Even though the surfactants residue can negatively affect the electrical conductivity of CNTs, surfactants such as NaCl addition in PAN can improve graphitization in fibers [140]. The surface morphology of the composite NFs with concentrations higher than 9 wt% of CNT is rougher than those of pure PVB NFs. The CNTs are well dispersed in the polymer matrix without agglomeration. Improvement in tensile strength of most CNT/polymer composites are accompanied with a reduction in strain at break of the composite [133]. Fabrication of nanocomposites consisting MWCNTs and Fe_3O_4 onto carbon fibers was obtained through an electrophoretic co-deposition process (EPD). -17.1 dB maximum reflection loss was found for sample with 2 mm thickness. An MWA composite containing only magnetic or dielectric materials will not offer a good MW attenuation performance due to insufficient MW attenuative mechanism. Composite with only dielectric parts such as MWCNTs or CFs due to non-magnetic nature in them, a huge portion of received EMW will be reflected

after interaction with its surface and the material cannot supply a high EM waves protection performance. High surface area provides more actives sites for dissipating, scattering[27].

2.8.3 Incorporating PolyIndole (PIn)

Conductive polymers show some superior properties over conventional polymers as they can induce charge and electron transfer through their chemical structures, called conjugated structures. They owe facile preparation, ease of surface modification. The pristine PIn electrical conductivity was reported $(1.15 \pm 0.28) \times 10^{-3} \mathrm{S\ cm^{-1}}$ [142, 143] by emulsion polymerization. It can be synthesized by both chemical and electrochemical methods [144].

Via in situ polymerization(IP) of indol on the surface of MWCNT with an addition of metal oxide(ZnO) Nanoparticles, synthesize of electrode materials(ZnO/PIn-MWCNT) may be used for enzymatic biofuel cells(EBFCs) resulting in immobilizing glucose oxidase(GOx) and mediator(Ferritin) [145](*polyindole functionalized). Graphene-based material/polyindole prepared from IP may facilitate homogenous dispersion of graphene in the polymer matrix to provide great electrical conductivity acting as methanol sensor [142]. Interacting with crystalline particles such as zinc ferrite can enhance alternating current, DC conductivity, fast ammonia gas response. Conductivity and polymerization of PIn efficiency are lower compared to other conducting polymer although having good environmental stability, high redox activity, low toxicity, low cost, good thermal stability, thermal properties, optical properties [67], and slower degradation rate compared to other CPs [68, 69, 144, 146, 147]. It shows the properties of both polypyrrole and polyaniline[144]. The lower electrical conductivity, electroactivity happen due to its relatively irregular structure of the polymer chain [144]. Also, add to Cu-Al_2O_3 can improve alternating current conductivity, dielectric constant, current-voltage characteristics and also cause the restriction of mobility of polymeric chain by the attachment of nanoparticles in the

macromolecular chain resulting in increased glass transition temperature [67]. It is the least investigated CP having both benzene and pyrrole rings [66, 146]. It is a promising pseudocapacitive electrode material for its higher interactive behavior [146]. Synthesis of PIn based nanocomposites in other studies show poor dispersion of filler in the polymer matrix [69, 148] due to agglomeration [67]. Doping of Cu in PIn/PVAc can reduce dielectric constant and dielectric loss with increasing frequency. Frequency-dependent AC conductivity in disordered polymers/CP can be found by interfacial polarization at the contacts, grain boundaries, and other present homogeneities. The mentioned electrical properties may depend on the weight percentage of oxidant concentrations [70] or weight fractions of filler in polymer matrix [67]. PIn fiber prepared via electrospinning method shows pH dependent Cu (II) adsorption, adsorption capacity decrease with PIn nanofiber diameter increase. This study investigate potential application for Cu(II) removal in wastewater management [71]. It's nanocomposites are suitable for rechargeable batteries, supercapacitor, solar cells, gas sensors, corrosion inhibitors [67, 144, 149]. Dimple fracture and droplet-like nanostructure with a small hole were visible along with the microvoid in the ternary blend revealing mesoporous nanostructure, which can be a great conductive material [146]. The increase of crystallinity of PIn and the addition of nanometal-oxide such as MoO_3 and WO_3 was reported for electronics and optoelectronics applications requiring semiconductor materials. The hopping distance of the charge carrier also increased due to an increase in activation energy[144]. A combination of nano metal oxide with polymer chain increase degradation temperature than PIn [144, 150]. Fe_3O_4 suffers from aggregation caused by their surface to volume ratio and attractive force decreases their superparamagnetic properties[68]. In PIn/Ag-CeO_2 were prepared using PIn as reducing agent [149].

CHAPTER III

EXPERIMENTAL TECHNIQUES

3.1 Force spinning®

Centrifugal spinning (CS) has become an efficient approach to producing nanofibers from various materials because it can eliminate some drawbacks of electrospinning (ES), such as low production rate, high-voltage setup requirement, the dielectric solution to promote optimum fiber formation. Thus, nanofiber structures can be fabricated into an aligned 3D structure or any arbitrary shape by varying the collector geometry, fiber morphology (beaded, textured, or smooth), fiber diameters and web porosity can be manipulated by altering the process variables, fiber fabrication is independent of solution conductivity, easily applicable to polymer emulsions and suspensions, and capable of substantially higher production rates as compared to standard electrospinning [151]. Besides, an important feature of this process is that it does not require a positive displacement feed system to deliver the melt through the orifice. The polymer mass flow rate through the spinneret is partially governed by pressure-driven flow from the outward centrifugal force acting on the melt at the spinneret entrance [152]. It eliminates the need for the charged solution, test materials having high dielectric constant [153]. Using the same amount of solution CS shows more loosely packed fiber mats compared to ES [154]. A schematic diagram to interpret Force spinning® of polymer nanofibers is shown in Figure 2. The general setup for FS, called Cyclone machine [155] has been discussed in several articles [152, 156, 157]. A

spinneret is mounted on a shaft which is connected to an electric motor. In this way, the applied centrifugal force is mainly responsible to drive the material through a designed set of orifices on the spinneret to produce the fibers. The collector system gives the flexibility to collect fibers either as a free-standing mat [135], to deposit fibers on a substrate, or to prepare 3D configurations. The processing variables that play an important role in the FS process are spinneret design, angular velocity, and aerodynamics of the chamber. It is a novel method that makes use of centrifugal forces to produce nanofibers rapidly and at high yields. The phenomenon of centrifugal force-based spinning is based on the principle of a cotton candy machine, few reports are demonstrating its capabilities as an NF manufacturing technology [133]. No electric fields are needed; therefore, restrictions imposed on materials with low dielectric constants are eliminated [158]. This method ejects fibers radially outward onto a collector producing nanofibers already confirmed experimentally to be as small as 50 nm in diameter. When producing nanofibers by Forcespinning®, it is required that the polymer is in liquid form; this can be done by either preparing a polymer solution or by melting [152, 159]. The polymer is loaded into a special spinneret that rotates the fluid which is then expelled as nanofibers onto a collector a certain distance away from the center [156, 160, 161]. For melt spinning, both upper and bottom heater rings must be engaged to melt polymer [159]. As the spinneret is rotated at an angular velocity, a thin polymer jet is ejected from the orifice and continues to thin out as it travels in a spiral path, and the formation of a jet with a curved centerline happens [162] before reaching the collector. In the context of surface instability, the polymer jet formation instead of droplets is caused due to the viscoelasticity of polymer solution [163]. The exiting polymer jet undergoes a large pressure drop at the orifice followed by strong extensional and shear forces, which results in fiber formation through deformation, extension,

and reorientation of the polymer chains [157]. The imbalance among centrifugal force, viscous force & surface force can induce the jet to be broken up [154]. The properties associated with the polymer solution or melt play a significant role in determining the resulting fiber diameter and morphology.

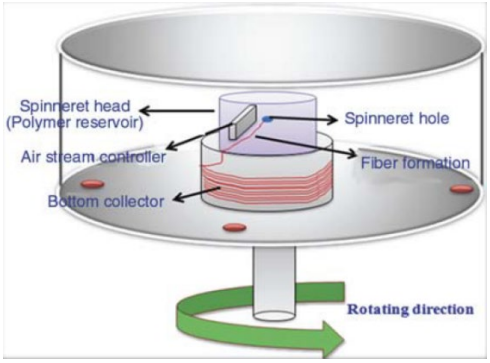

Figure 2: Schematic diagram of in-house developed centrifugal spinning setup and I benchtop instrument [164]

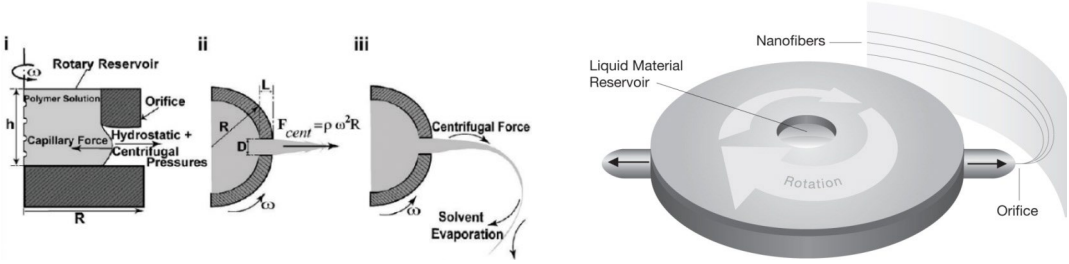

Figure 3: Magnified view of the formation mechanism of nanoscale fiber through Centrifugal Spinning [151, 158, 159]

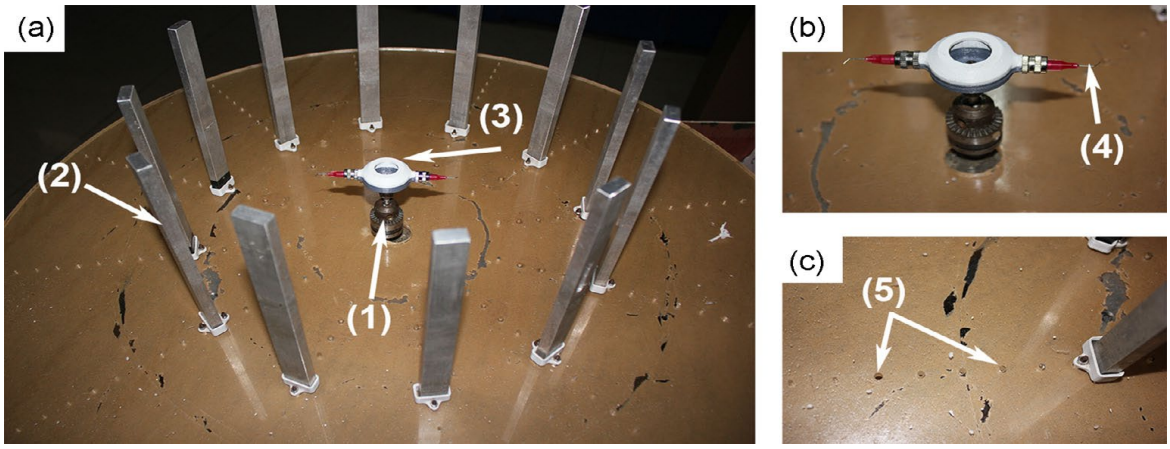

Figure 4: CS set-up used. (a) The overall appearance of the device: (1) High rotational speed supply, (2) collector, and (3) spinneret. (b) Spinneret structure(4) Nozzle (c) Baseplate(5) apertures can provide for changing the nozzle-to-collector distance[165]

Badrossamay et al. [151] described rotary jet-spinning (RJS) where the RJS system consisted of a reservoir with two sidewall orifices that were attached to the shaft of a motor with controllable rotation speed. To facilitate the fiber collection a flexible airfoil is placed on the shaft above the reservoir. The polymer solution is continuously fed to the reservoir at a rate enough to maintain constant hydrostatic pressure and continuous flow. Dual-chamber reservoir (DCR) for example, a feature in the RJS system in controlling mechanical properties, well fiber dispersion & spinning multi polymer in same nano fabric [166]. The resulting fibers are collected either on a stationary, surrounding cylindrical collector or on coverslips which were held against the collector wall. The fiber production process is composed of (i) jet-initiation to induce the flow of the polymer solution through the orifice, (ii) jet-extension to increase the surface area of the propelled polymer stream, and (iii) solvent evaporation to solidify and shrink the polymer jet. The steps are also mentioned in other sources as well [167].

At first, a combination of hydrostatic pressure and centrifugal pressure at the far end of the capillary overcomes the flow-resistant capillary forces and propels the polymer liquid through the nozzle capillary as a jet. The outward radial centrifugal force stretches the polymer

jet as it is projected toward the collector wall, but the jet travels in a curled trajectory due to rotation-dependent inertia. Stretching of the extruded polymer jet is critical in reducing jet diameter over the distance from the nozzle to the collector. Concurrently, the solvent in the polymer solution evaporates, solidifying, and contracting the jet.

3.1.1 Parameter Investigation

3.1.1.1 Concentration

Polymer concentration has a stronger effect on fiber characteristics. The increase in polymer concentration leads to fiber formation with larger diameters [133]. For centrifugal spinning, an optimal range of solution concentration is required to form fiber, resisting beading. At low polymer concentration, bead formation occurs but with increased concentration, it leads to a mixture of beads and fiber firstly and above critical concentration continuous fiber formation due to sufficient chain entanglement [151]. The more polymer concentration appears the more overlapping of polymer chains shows sufficient entanglement networks of polymer chains [163] introducing viscoelastic effect [168]. The viscoelastic property of Chitosan/Polyamide (CP) can be described by inserting Chitosan into polyamide solution [169]. At the concentration when the fiber starts showing uniform, continuous, bead-free fiber is called critical concentration. The presence of beads along the fiber can be eliminated by increasing polymer concentration reported by Cremar et al. [170]. An optimum concentration is defined by a concentration that is required to form bead-free fiber with the most uniform morphology. Even exceeding the optimum concentration can reform beaded fiber. PVP shows such trends while concentration is increased from 16 % to 18% [167]. Even higher concentration leads no formation of fiber due to nozzle clogging from high viscous effect [141]. To prevent such clogging, the self-cleaning behavior of channeled nozzles with geometries must be considered [171]. Minimal concentration is required

for a suitable and critical polymer chain entanglement that promotes fiber formation [172]. The optimal solution to form fiber for cellulose-based polymer fiber is 46-50 % w/w [173]. The entanglement concentration (C_e) can be determined from the data of specific viscosity to understand the correlation between Ce and centrifugal spinnability. Depending on the rich amylopectin content in starches, the weakening entanglement behavior can be explained by amylopectin's highly branched structure. Formation of fiber can be done when the spinning solution reaches critical concentration [165]. Exceeding of Critical concentration by adding ionic compound such as NaCl can decrease fiber diameter[140] (74). The C_e can be identified by the critical chain overlap concentration (C*). The point at which the concentration inside a single macromolecular chain is equal to the solution concentration, or C*, can be estimated as $C^* \sim 1/[\eta]$, where $[\eta]$ is the intrinsic viscosity of the polymer solution, later was used to separate different solution regimes [174].

For polymer gel, to overcome attractive force between gel and spinneret material, lower adhesiveness is required. The adhesiveness calculation helps detection of spinneret concentration of cellulose gel of different concentration [173]. Increasing solvent volatility leads to increased polymer concentration [175]. Amorphous ring or discrete diffraction caused by the alignment of polymer chains can be controlled by polymer concentration which is attributed to increased crystalline morphology resulting in brittleness of nanofiber [176]. In comparison to the inorganic piezoelectric ceramics, co-polymer can be suitable in terms of brittleness [166]. Changing concentration can yield various surfaces including porous, smooth, wrinkled, and the intermediate state between pore & wrinkle called groove features [141].

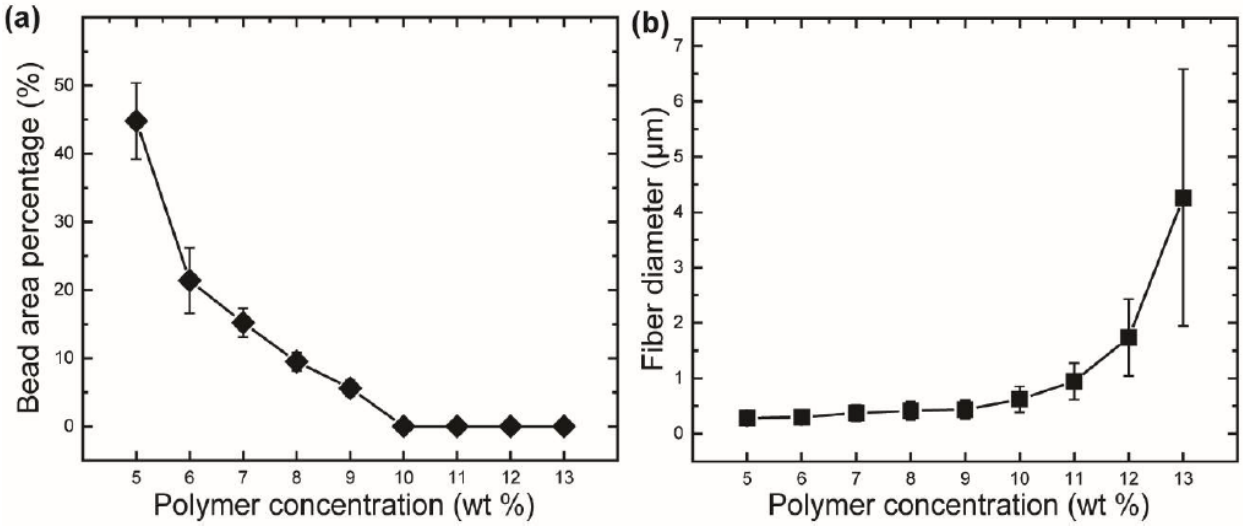

Figure 5: Variation of (a) bead area percentage and (b) fiber diameter of rPET fibers fabricated from various polymer concentrations [173]

The contraction of PEO fiber trajectories can be defined by increasing its concentration which indicates the opposite relationship between jet speed and concentration [162]. Even though the previous fact, the concentration variation presents minimal effects on surface tension but the significant change of viscosity which has been shown by data found from PEO [163].

3.1.1.2 Molecular Weight

The continuity of fiber morphology is also dependent on polymer molecular weight which facilitates polymer chain entanglement. Critical chain overlap determined by the minimum molecular weight shows an impact on the fiber morphology [163]. It is found that the molecular weight of polymers has inversed effects on the optimum concentration range for spinning processes. The Mw along with polydispersity degree is necessary to explain complex interplay among the other parameters involved in morphology examination [171].

The spinnability of the polymer blend is favored by molecular weight. To avoid droplet formation, a polymer having a higher molecular weight is required. Otherwise, a higher

concentration is necessary to compensate for the effect of the low molecular weight of the polymer.

3.1.1.3 Viscosity

The viscous polymer solution is necessary for maintaining the required spinning characteristic to produce desirable nanofiber. Beyond this optimal range, the higher solution viscosity limits solvent evaporation and necking, resulting in thicker fibers [151]. The viscosity of the polymer solution can be interpreted to be a measure of the extent of polymer chain entanglement. With an increasing degree of polymer chain entanglement, the viscosity of the polymer solution increases [177]. Prolonged stress relaxation time is a side phenomenon in a highly viscous solution which offers limited evaporation of solvents and prevent jet fracturing, elongation and thinning, finally promotes large fiber diameter [141]. The viscosity changes of the polymer are in good agreement with the results of the microstructural characterization based on the o-Ps lifetime values described by Sebe et al. [134]. They stated a high level of viscosity in the hydrogels derived from C spun polymer resulting in less presence of halogen contents in resultant fiber. Viscosity changes with polymer concentration can be governed by a power law [175]. Viscosity increases with the increase of solution concentration for different starches containing various percentages of amylose content described by Li et al. The dynamic viscosity of biohybrid solutions increased with increasing protein content [178]. The viscosity found from some fibers has an inverse relation to mechanical property like shear rates [165]. Long-chain of polymer is responsible for such higher viscosity making the dissolution more difficult [179].

But increasing concentration beyond a certain limit can arise the phase separation to drop the viscosity. The concentration above 20% cooled polymer solution of Lignin/TPU can display the upshot [180]. With the fast crystallization kinetics of PBT, the difference between the process

and crystallization temperature likely has a more dominant effect than viscosity in controlling the fiber diameter population [152]. Increasing the temperature could lead to faster solvent evaporation but it will further decrease the viscosity [133]. The low viscosity can be attributed to a concentration lower than critical concentration resulting in low binding energy in the polymer chain. The intrinsic viscosity of polymer solution can be determined by using the Huggins and Kraemer equations [174]. For melt-spun fiber, different data of viscosity measurement assists in studying the development of fiber morphology. It appears that fiber needs to be formed abundantly with a higher temperature range to overcome viscosity. The higher viscous PCL solution sometimes results large, broken or necking type behavior for both thick and thin fiber[181]. Jet speed increases as the viscosity decreases [162]. Reduction in shear viscosity can be found while reducing concentration using the shear rate as a parameter in dynamic shear experiments [133]. A local abnormal increase in viscosity can intensify fiber coalescence and produce irregular fiber diameter [171].

3.1.1.4 Surface Tension

To produce nanofibers with the Forcespinning® method the force due to surface tension must be overcome by the centrifugal force[158, 160, 161]. As the jet is stretched, the surface tension of the polymer solution can cause the jet to break to produce droplets [182, 183] or jet to become unstable [167]. Bead formation occurs because surface tension is minimized in a spherical geometry[175]. Surface tension induced bead formation can be compensated by varying polymer concentration [151]. Nanofiber from starch also shows such surfaced tension induced by Rayleigh-Taylor instability to form beads [165]. The addition of sodium chloride to PAN fibers can reduce its surface tension resulting significant decrease in fiber diameter. It happens due to the percentage decrease of Nitrogen with an increase of salt content identified by

comparing the surface composition of nitrogen and nitrogen-to-carbon ratio in different samples [140]. The formation of thin veils stimulated by the addition of salt to polymer solution might be another fact to consider [184].

3.1.1.5 Flow rate/Feed rate

Processing parameters such as angular velocity, flow rate, time, and nozzle size and geometry should be evaluated to determine optimal processing parameters for the development of fibers with small diameters, narrow distribution, and absence of beads. Since the polymers also possess elastic properties, the stretching rates and relaxation times must also be considered. Another important factor is the rate of solvent evaporation, which influences the polymer's viscosity and elasticity. Including those factors, the collector diameter, radius of needle orifice is also required for the modeling of fiber formation with the determination of trajectory and final diameter size [158]. Viscoelasticity is a time-dependent polymer property influenced by external force and time constant. The smaller/larger time constant shows the more elastic or viscous response of the polymer chains respectively [163]. The flow rate of polymer melt solution plays a major role in nanofiber formation and uniformity. The polymer mass flow rate through the spinneret is partially governed by a pressure-driven flow from the outward centrifugal force acting on the solution at the spinneret entrance [133]. With increased Melt flow rate (MFR), the average fiber diameter decreases [159]. The slower volumetric flow rate leads the solvent evaporation for a prolonged period during the spinning process [168]. It's another indication about the fluid fill level that the material feeding changes the pressure within the container, somewhat, connected with the mass of fluid present [136].

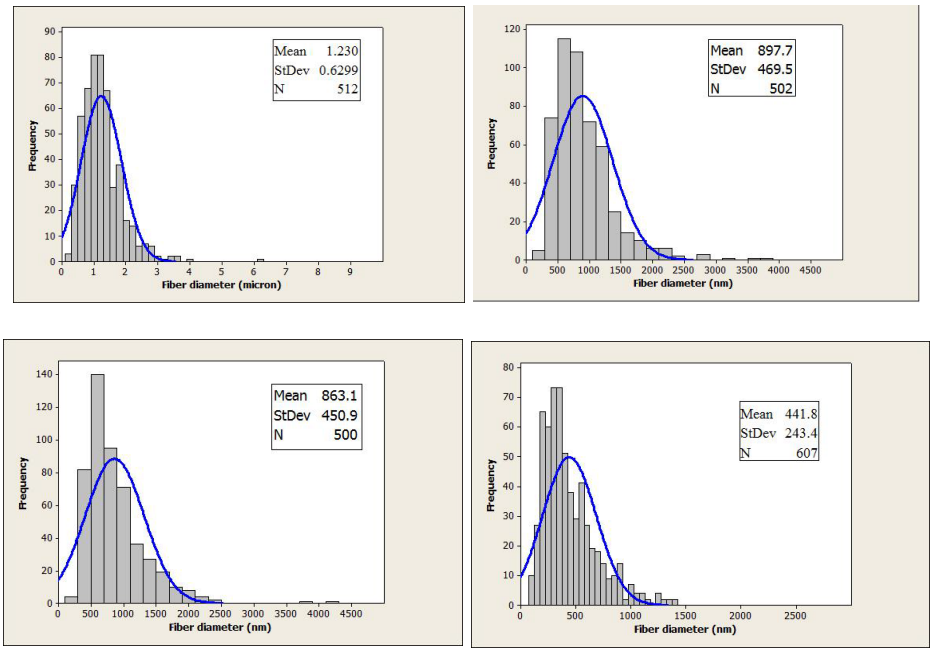

Figure 6: Fiber distribution showing fiber diameter change with MFR change [159]

3.1.1.6 Ambient Parameters

The solvent evaporation rate depends on its volatility. If the solvent is highly volatile, the jets form thicker fibers as the rapidly evaporating solvent potentiates rapid solidification, hindering the jet extension [151]. Shanmuganathan et al. described temperature as a factor having a stronger effect on fiber characteristics relative to other factors. Increasing the spinneret temperature led to a significant increase in the percentage of submicrometer fibers. Increasing the extrusion temperature allows the polymer jet to remain in a molten state for a longer period promoting additional stretching before solidification by crystallization. They also supported the inverse relationship between temperature and viscosity by showing an order of magnitude reduction in shear viscosity of PBT polymer with increasing temperature [152]. The crystallization under molecular orientation inherits the process of structural changes, can be maximized by a strong dependency on temperature. In melt-spun PP fiber, at the exit of the nozzle undergo rapid cooling resulting temperature drop which is due to the air stream caused by

the rotating spinneret. This rapid cooling promotes the extensive formation of crystals [159], beads [181]. The solvent evaporation makes the temperature change of the polymeric jet change despite the pressurized gyration process happening at ambient temperature. The elongation viscosity is surely affected by evaporating the solvent through heat or frictional loss induced by high rpm which is more likely to be used to measure final fiber diameter and distribution [163].

The temperature and humidity level of the area had been fixed within 70–75 °C and 40–45% respectively to produce AIP/PVA composite fibers [185]. Fibers should be covered and stored under desiccation to achieve a low humidity. At lower humidity levels, clean homogenous, individual fibers are formed with no interconnections. Thin-film formation in the collector will likely occur due to the inhibition of fiber formation at a higher humidity level [184]. So, it's necessary to spin at lower humidity to produce homogeneous, continuous fiber. But some studies are also performed at higher humidity reported elsewhere [167].

3.1.2 Type of Collectors

Generally, the fibers are collected onset of column collectors [186], Vacuum collecting system [187], deep-dish fiber collector with equally distanced vertical steel pillars [133, 172] [188] in a form of web. They can be deposited on a polypropylene [188] substrate using a vacuum box to obtain nonwoven fibrous membranes [172]. To directly deposit MPFs onto Ti substrate, Ti foil cut into the required dimension is fastened onto alumina collectors with polytetrafluoroethylene (PTFE) tape before the FS process [189]. Fiber can be collected in a rotating cylindrical collector mounted on a linear motor [166]. Polypropylene sticks are placed equally in a circular pattern.

3.2 Characterization

3.2.1 Scanning Electron Microscopy Analysis

The Scanning Electron Microscope (SEM) is a piece of topographic characterization equipment, which scans the sample by shooting electrons using an electron beam to the surface and analyzes the signals coming from the interaction between electrons and atoms from the sample. The detection system provides information on the topography and composition of the sample which translates to an image visible up to the nano level and sometimes even smaller. The function of the SEM is based on the electron behavior after electron-sample interaction. An electron beam that carries electrons with a significant amount of kinetic energy interacts with the sample materials. Some of these accelerated electrons pass through the sample and some scatter elastically and inelastically. The electrons passing through the sample without interaction can be used for Transmittance Electron Microscopy (TEM). The elastic or inelastic scattering of electrons results in different signals including secondary electrons (SE), backscattered electrons (BSE), characteristics X-rays, auger electrons, visible lights, and heat. Some of these signals provide imaging, quantitative, and semiquantitative information of the sample. Secondary electrons are mostly advantageous for morphological and topological information. On the other hand, backscattered electrons are advantageous for the distribution of information about various elements in the sample. The signals are detected with electron detectors and processed for a detailed image of the sample surface.

An SEM mainly consists of an Electron source (also called electron gun), Electron Lenses, a sample chamber, an electron optical column, detectors for all signal of interest, display or data output devices, and other infrastructure requirements like power supply, vacuum system, cooling system, vibration-free floor, etc. Firstly, the electron gun on the top of the column

introduces an electron beam. Constructing an electron gun is generally done by pulling the electrons from “V” shaped electron clouds when the electrons are attracted by the positively charged anode. Due to the divergence characteristics of a beam, a condenser lens is introduced to render the divergent beam from the point source into a converging beam. Then it passes through a spray aperture which is usually a high precision drilled hole used to avoid scattering. Then again, a second condenser lens is used to converge the scatter free beam. The magnetic characteristics of the condenser lens help bend the electron beam when necessary. In the next step, more than one deflector coils are introduced to push the electron beam backward and forwards across any sample. To avoid further scattering, another final lens aperture helps enhance the quality of the beam. The beam of electrons hits the surface of a sample which is mounted on a stage in the chamber area. Some of the electrons in the beam bounce back from the sample. As the sample is made up of atoms, some new electrons also come off it as well. The electrons that come from the sample are attracted by a device called a detector. This beam is scanned in a rectangular raster over the sample specimen and the intensities of various signals created by interactions between the beam electrons and the sample are measured and stored in computer memory. To generate an image on the screen, the electron beam needs to move in horizontal lines backward and forwards across the sample. Each horizontal line is a series of steps. Depending on the height, and the shape, of the sample at each step we get black, grey, or white dots that create the image on the screen. For the low vacuum operation, both the column and chamber are evacuated by a vacuum pump. The Figure 7 shows the stepwise operating mechanism described above.

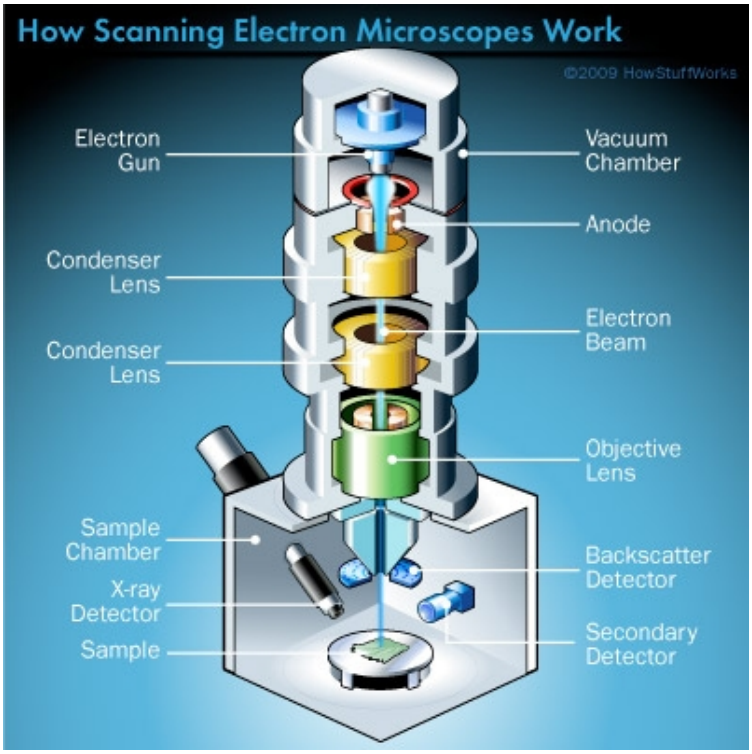

Figure 7: Schematic of the Scanning Electron Microscope [189]

3.2.1.1 EDAX/X-Ray Detector

Energy Dispersive X-ray analysis (EDAX) is an integrated feature of a Scanning Electron Microscope (SEM) which is used to identify the elemental composition of a specimen. Each element is identified by its unique amounts of energy in an X-ray that was released by the specimen during electron beam bombardment. During the bombardment, electrons collide with each other knocking electrons out of their orbits. A higher-energy electron from an outer shell replaces an inner shell electron that was knocked out. The transferring of the higher-energy electron to the inner shell emits an X-ray. The X-ray that is emitted has a fixed wavelength which is related to the difference in energy levels of electrons in different shells for a given element.

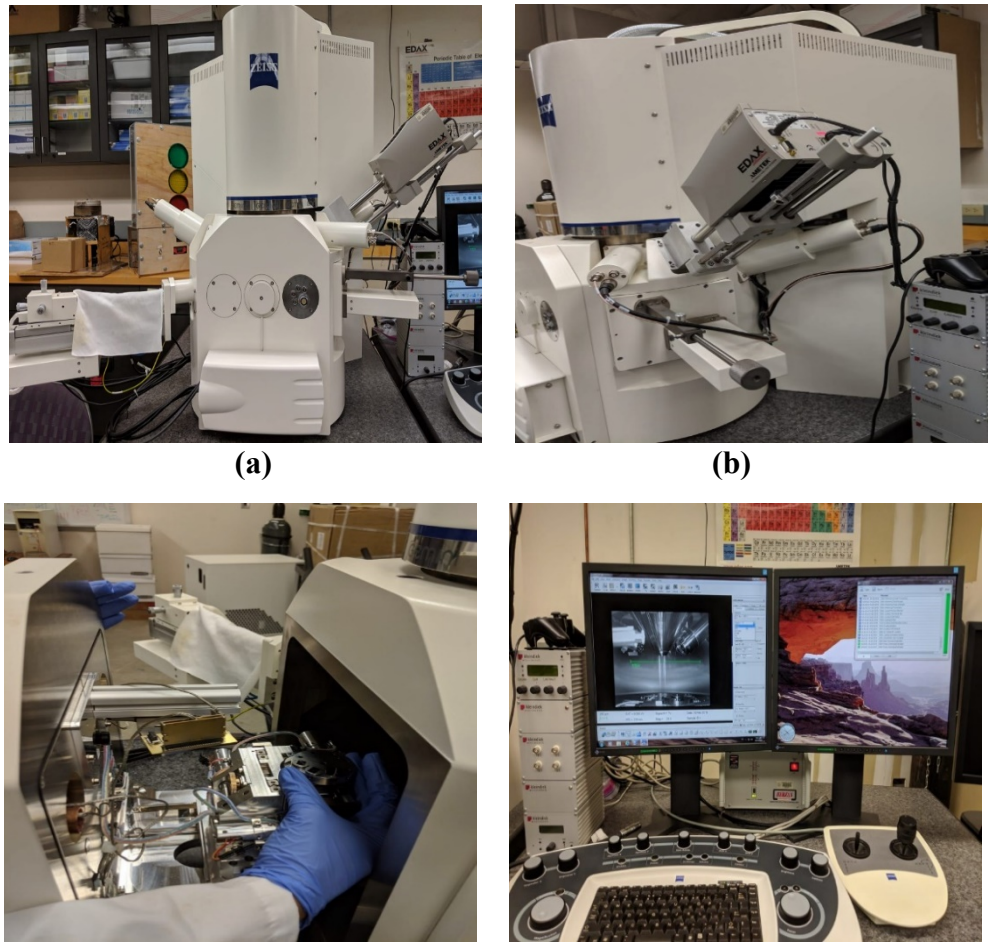

Figure 8: Outer structure of an SEM (a) Front view (b) side view (c) Inside view of SEM (d) Display/data output device

Chemical transformation within fiber can be validated by EDX by keeping its consistency with other elemental composition analysis. In the case of PVP/Iron Nitrate solution used for FS of nanofibers, after calcination of obtained fiber to eliminate organic compound, EDX showed the formation of Iron Oxide fiber [190]. The successful removal of sulfuric acid impurities was confirmed by energy-dispersive X-ray spectroscopy [176]. Studying visible structure obtained from SEM to identify polymer can be performed by EDX [191]. The deconvoluted spectra from EDS provide a bonding position between atoms on the surface of particles [135].

3.2.2 Fourier Transform Infrared (FTIR) Spectrum

Fourier transform infrared spectroscopy is a method that is used to identify organic, inorganic, and polymeric materials utilizing infrared light for scanning the samples. The common components of FTIR spectrometer are a source, interferometer, sample compartment, detector, amplifier, A/D converter, and a computer [192]. During analyzing a sample, the infrared radiation from the source is passed through the sample while some part of radiation gets absorbed and later converted into vibrational or rotation energy. The rest of the radiation is transmitted through the sample.

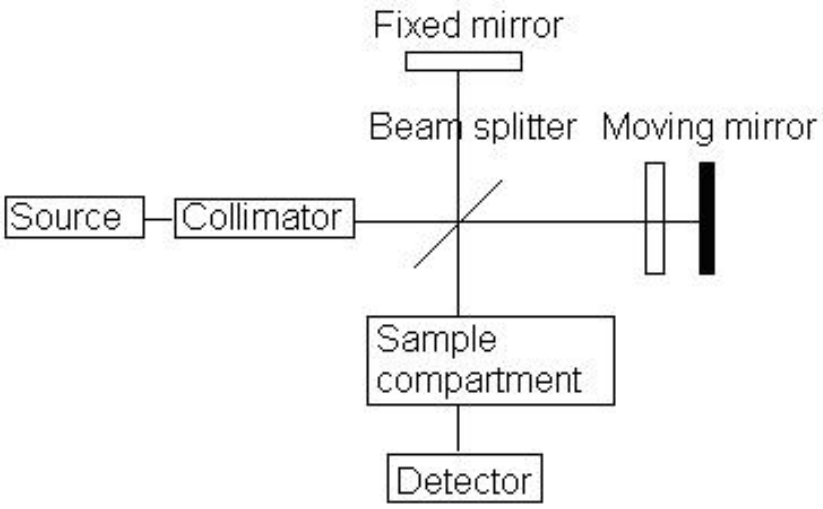

Figure 9: Block diagram of an FTIR spectrometer [191]

Attenuated Total Reflectance-Fourier Transform Infrared (ATR-FTIR) spectroscopy of polymer, Polymer/collagen, and Polymer/gelatin scaffolds can be obtained on a spectrometer system over a range of resolution. FT-IR spectroscopy imaging can be obtained on the FTIR spectrometer and Varian imaging microscope equipped with a liquid nitrogen-cooled focal plane array (FPA) detector. The samples are mounted on gold-coated wafers. The distilled water-soaked fiber needs to be dried in an oven before putting in FT-IR spectroscopy to quantify the

time rate of change of composition on the fiber surface [178]. FT-IR analysis can be attributed to molecular bond (pie-pie interaction, hydrogen bond) within composite polymer matrix [133], atomic bond stretching [189], structural evolution [193].

3.3 EMI Shielding Testing

The total EMI SE (SE_T) is a summation of EMI SE reflection (SE_R) and EMI SE absorption (SE_A) while EMI SE reflection was determined based on the measurement parameters. Scattering parameters for EMI SE absorption can be obtained by subtracting S11 and S21 from 1 [18, 19, 22, 26]

$$\mathrm{R} = |\mathrm{S11}|^2 \quad \mathrm{T} = |\mathrm{S21}|^2$$

$$\mathrm{A} = 1 - \mathrm{R} - \mathrm{T}$$

$$\mathrm{SE_A} = -10\log(1 - \mathrm{R})$$

$$\mathrm{SE_R} = -10\log\frac{\mathrm{T}}{1 - \mathrm{R}}$$

$$\mathrm{SE_T} = \mathrm{SE_R} + \mathrm{SE_A}$$

S12 and S21 are equal and known as the transmitted part of the received MW from the back of material [27]

$$SE_A = 8.7t\sqrt{\pi f \mu \sigma}$$

$$SE_R = 20\log\left(\frac{\sqrt{\mu_0 \sigma}}{4\sqrt{2\pi f \mu \varepsilon_0}}\right)$$

3.3.1 Concept of Vector Network Analyzer (VNA)

Measurement of impedance at low frequency can be done by various equipment such as voltmeter, current meter, sine wave generator, etc. For high-frequency impedance measurement, a network analyzer is typically used. The light ray incident on the lens device can explain the concept of VNA. As some incident light passes through the lens, others reflect. If there is another obstacle after the lens, then the transmitted rays reflect (A2) to the lens. Then the light gets split into two parts viz. They get merged with original reflection (B1) and transmitted light (B2) respectively.

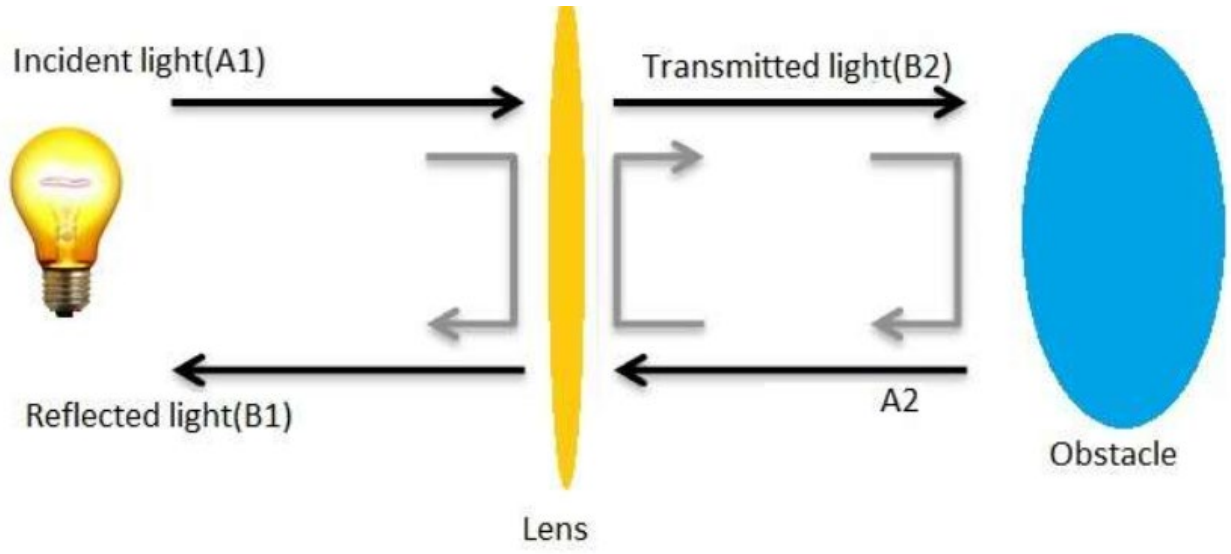

Figure 10: Concept of vector network analyzer in terms of light ray incident [193]

CHAPTER IV

METHODOLOGY

4.1 Solution Preparation

Solvents: N, N-Dimethylformamide (DMF) (anhydrous. 99.8%), formic acid (≥95%, reagent grade) were purchased from Sigma Aldrich. Absolute Ethanol Fisher Scientific

Polymer: Nylon 6 pellets, Polyacrylonitrile (PAN) (Mw 150,000) from Sigma Aldrich

Dopants: Ferroferric oxide (Fe_3O_4) nanopowder (50-100 nm particle size, 97% trace metals basis), amino-functionalized multi-walled carbon nanotubes (MWCNTs) (carbon purity > 99 wt%, average outside diameter <20nm, length 1-12μm), Carboxyl (COOH) functionalized multi-walled carbon nanotubes (MWCNTs) (carbon purity > 95wt%, average outside diameter < 8 nm, length 10-30 μm) from cheap Tubes.

Polymerization Materials:

Oxidant: Ammonium peroxydisulfate, ACS, 98% min from Thermo Fisher Scientific

Monomer: Aniline, Indole (≥99%, Mw=117.15)

Acid: Sulfuric Acid, Hydrochloric acid, 37%, for analysis (max. 0.000001% Hg) (Mw=36.45) from Acros Organics.

4.1.1 PAN Solution

The concentration of 12 wt% PAN was taken as a control and DMF was taken as the solvent throughout the experiment. To prepare a 10 g solution, 8.8g of DMF was measured by calculating the mass of the liquid volume of the solvent with its density of 0.944 cm^3/g. Also, by using a pipette, DMF can be weighted on the four-scale electronic scale to avoid calculation while placing it inside a 20mL glass vial. Then a magnetic stirrer was placed in the solvents.

After that, 1.2 g of PAN powder was weighted on the same scale and added to the DMF solvents. The above sequence is mostly followed in the experiment to skip the complexity of the magnetic stirrer to rotate freely from the beginning. The mixed solution was sonicated in the ultrasonication bath for 30 mins and then put on the magnetic plate for 12-24 hours between 30-40 ^oC.

4.1.2 Fe_3O_4 doped PAN Solution

Solutions containing PAN and Fe_3O_4 in DMF were prepared. The 5,10,15,20 wt% of Fe_3O_4 were measured with respect to PAN weight in the electronic scale where the equivalent weights are 0.06,0.12,0.18 and 0.24 g respectively. The weighted dopants were then dispersed in 8.8g of DMF in an ultrasonic bath in separate vials for 2 hours and were then mechanically agitated for 10 min. Subsequently, PAN (12 wt%) was added to the Fe_3O_4 dispersion. The obtained solutions were subjected to magnetic stirring at 30-40 ^oC for 12-24 hours.

4.1.3 Amine functionalized multi-walled carbon nanotubes (MWCNTs-NH_2) doped PAN solution

Four different doped solutions containing MWCNTs-NH_2 were prepared. The weight percentage of MWCNT-NH_2 are 5,10,15,20 which are 0.06,0.12,0.18,0.24g respectively. The measured dopants were dispersed in an ultrasonic bath and mechanically agitated in a similar pattern as described in the previous section. After placing the magnetic stirrer, 12 wt% PAN powder were added to each of the solutions with different concentration of MWCNT-NH2. The solutions were kept stirring at 30-40 ^oC for 12-24 hours.

4.1.4 Nylon 6 solution

25 wt % Nylon solution was prepared which has been used in two layers among a total of four layers of the final single system composite material. About 4.25 g nylon pellets were added to 13.5 mL of formic acid in a 20 mL vial which was calculated by weighting the mass of the volume of the solvent. After sonicating the solution for 30 minutes, the solution was mechanically agitated for 5-10 minutes. The solution was then magnetically stirred for 24 hours at room temperature.

4.2 Solution Spinning

Cyclone L100M from Fibrio Technology Corp has been used to perform Force spinning® (FS) of PAN, Nylon 6 based solution. Angular velocity (RPM) is one of the major parameters of the FS machine to yield fiber. Generally, higher temperature and lower humidity favor evaporation rate in which the solution requires less RPM to produce fiber and vice versa. The more the viscous solution the higher RPM it needs. For every spinning cycle, 1.5 ml to 2 ml of solution was injected into the metal spinneret inside the cyclone using a 3 mL syringe. 30G

needles were screwed on each side of the spinneret as the solution should come out of the exit having a smaller diameter.

There are eight metal stands used as collectors which were placed on a circular metal structure at an equal distance from the center. Before spinning, the inside chamber of the machine and the collectors were wrapped in aluminum foil to avoid contamination of the different fibers for the next user.

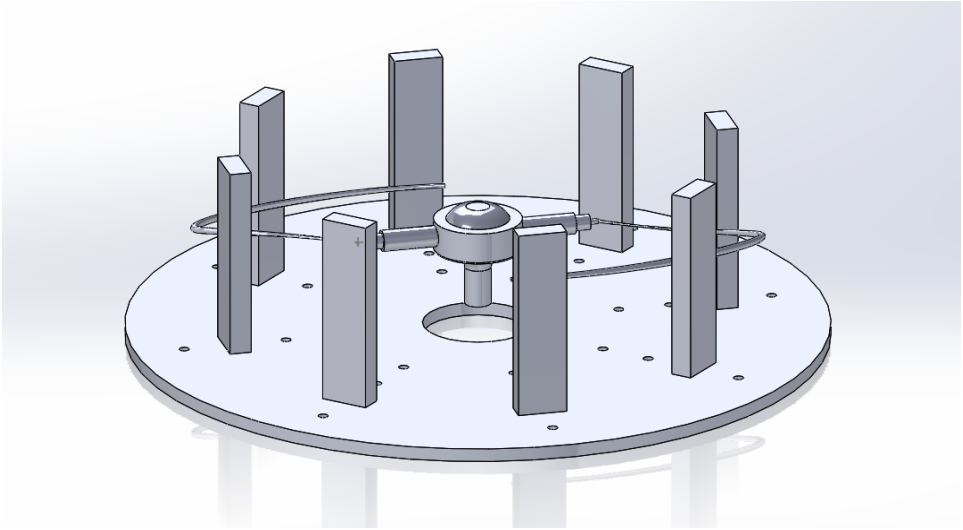

Figure 11: Representation of Forcespinning® technique

4.2.1 PAN Solution Spinning

Relative humidity between 50-58 with a temperature around 75º F is suitable for PAN fiber. The basic rpm requires for a 12 wt% PAN solution is from 8000 to 9000 pm with a run time from 30 sec to 1 minute. More run time produces a thicker mat attached to the collector in every cycle. In less humidity, the run time is set low as 20 seconds to avoid drawing the fiber to the center of the spinneret due to the air produced by the spinneret. Lower rpm may produce less amount of fiber while the collector must be placed close to the spinneret to reduce the travel time of the polymer jet. The collector's distance from the spinneret may vary from 8-12 inches.

4.2.2 Fe_3O_4 doped PAN Solution Spinning

PAN solution containing 5,10,15,20 wt% of Fe_3O_4 has been spun under the same condition as PAN solution. The filler loading has an impact on the viscosity of the solution. So, the rpm greater than 8500 is suitable under the relative humidity around 55. The magnetic nanoparticles have an affinity towards magnets so it's better to pull out the magnet from the solution before spinning. Otherwise, the solution becomes non-homogeneous due to the agglomeration of NPs toward the magnetic stirrer. Other parameters such as run time, collector distance is kept the same.

4.2.3 Amine functionalized MWCNTs doped PAN Solution Spinning

PAN solution containing 5,10,15,20 wt% MWCNTs-NH_2 has been spun under the same condition as PAN solution. The filler loading has an impact on the viscosity of the solution. So, the rpm greater than 8500 is suitable under the relative humidity around 55 under same run time, collector distance is kept the same.

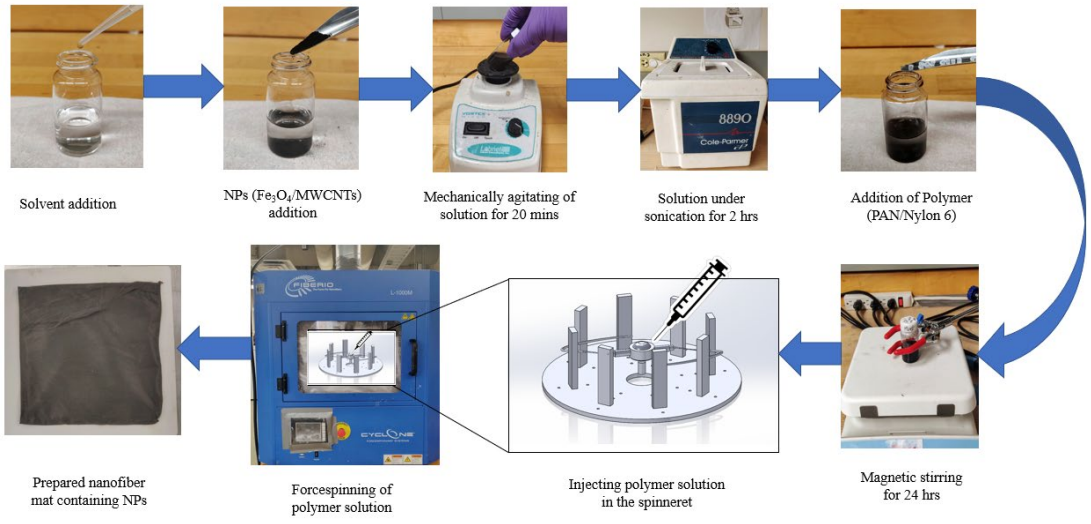

Figure 12: Preparation of NPs (Fe_3O_4/MWCNTs) doped PAN nanofiber mat

4.2.4 Nylon 6 Solution Spinning

The spinning of 25 wt% nylon 6 requires humidity less than 55 to produce the desired amount of fiber. The rpm range is from 7000 to 9000 in humidity between 25 to 50. Lower humidity favors nylon to yield more fiber than higher humidity. In low humidity, it's required to use higher rpm to reduce the travel time between container and collector due to its faster evaporation rate, otherwise, the fiber may be grounded on the collector circular structure. At higher humidity, the collectors are set far from the spinneret to increase the travel time to promote evaporation time.

After the conclusion of the spinning both solutions in every cycle, fibers caught on the metal collectors are collected by an aluminum wrapped cardboard mounted on a plastic frame. The cardboard frame is passed through carefully between the collectors one next to the other to cut the fibers in a rectangular section while maintaining the alignment without tearing them apart. The fibers are laid flat on the cardboard frame to create fiber mats. The mats were kept between the weight papers before wrapping them in aluminum foil paper.

Table 5. Fiber making condition for 25 wt% Nylon 6 or Nylon 6 with fillers

Material	RPM	Relative Humidity	Run Time (min)	Quality	Comments
Nylon 6	8000-8500	27	4-6	Very good	More fiber
Nylon 6	8500-9000	22-24	2	Very good	More fiber
Nylon 6	9000	40	2	Very good	More fiber
Nylon 6	9000-10000	52-53	2	Good	Moderate fiber
Nylon 6	7500- 8000	54	5	Medium	Less fiber

Nylon 6	7500	52-53	5	Good	Moderate fiber
Nylon+$AgNO_3$(l) (0.2g)	2000-9000	52-55	3-5	Bad	No fiber
Nylon 6+SWCNT(0.05wt %)	7500	51	5	Good	Moderate fiber
Nylon 6+ SWCNT (0.1 wt%)	7800-8000	54	5	Good	Moderate fiber

4.3 Fiber Coating

To enhance the conductive properties of nylon 6 nanofiber, they were coated with a conductive polymer and functionalized multiwalled carbon nanotubes. Three different types of conductive polymer and functionalized carbon nanotube have been applied on the surface of the fiber mats. For conducting polymer coating, in-situ polymerization has been performed.

4.3.1 Polyaniline (PANI) Coated Nylon 6 Mat

Chemical oxidative polymerization was performed for the polymerization of aniline[194]. 1M HCl solution has been prepared by adding 12M of 16.7 ml HCl to 200 ml distilled water. Then 4.564g APS is added little by little to the 1M HCl while stirring the solution in a big flask. Nylon 6 mat is cut into rectangular section and 3 ml aniline monomer is added dropwise on nylon 6 nanofiber and let it soak for 24 hr. The aniline soaked nylon mat is placed in the solution of the flask. The glass flask covered by aluminum foil containing submerged nylon mat into the solution is kept under shaking for 2-3 hours using an orbital shaker and leave it for 24 hours to complete the polymerization. The obtained green-colored nanofiber mat was taken out from the

solution, washed with 0.1M HCl, ethanol, and distilled water several times, and dried at room temperature for 24 hr.

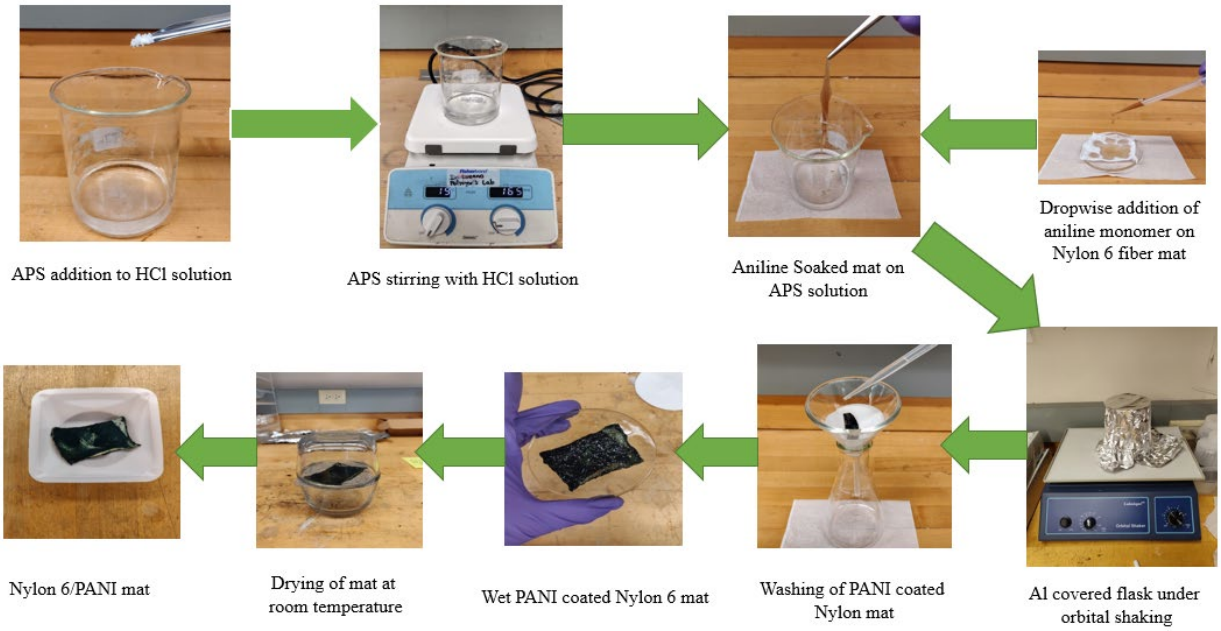

Figure 13: Preparation of Nylon 6-PANI mat

4.3.2 Polyindole (PIn) Coated Nylon 6 Mat

To prepare 0.2M/0.1M/0.05M APS solution, approximately 2.281g/1.1405g/0.57025g APS is added to 46 ml of distilled water little by little. Then a 0.1M/0.05M/0.25M indole monomer solution was prepared by adding 0.585g/0.2925g/0.14625g indole in 4 ml of ethanol and leaving it stirring. A nylon 6 mat was cut into a circular section and placed inside a glass flask. The mat was wetted with indole solution and APS solution was added dropwise with the help of a pipette. The glass flask covered by aluminum foil containing submerged nylon mat into the solution is kept under shaking for 2-3 hours using an orbital shaker and leave it for 24 hours to complete the polymerization. The nylon mat is then removed from the solution and cleaned with 0.2M of H_2SO_4 and distilled water several times. A light green coated mat is obtained after drying it at room temperature for 24 hours.

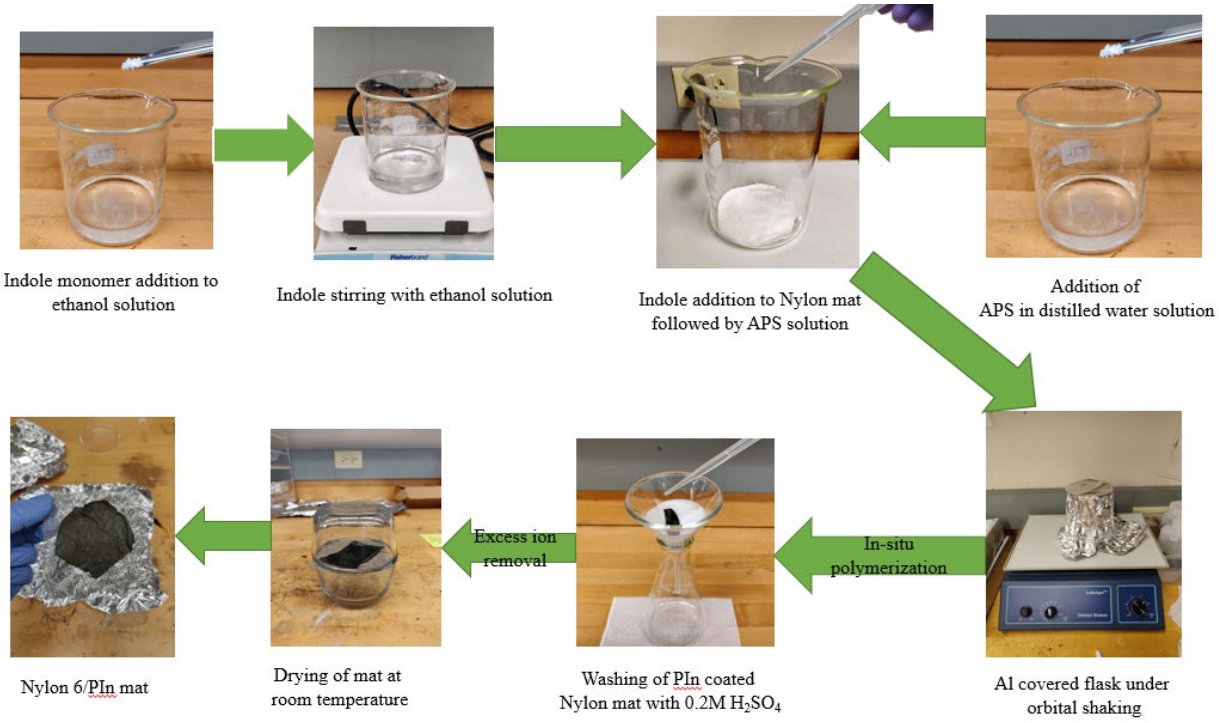

Figure 14: Preparation of Nylon 6-PIn mat

Table 6. PIn mat preparation with various concentration of monomer and oxidant

Sample Name	Ethanol (ml)	Indole (g)	APS	Comment
PIn_Mat 1	4	0.585	2.281	Brittle
PIn_Mat 2	4	0.2925	1.1405	Flexible and well decorated
PIn_Mat 3	4	0.14625	0.57025	Flexible but less polymer content

(a) **(b)** **(c)**

Figure 15: (a)PIn_Mat 1 (b)PIn_Mat 2 (c)PIn_Mat 3 prepared from different concentration of monomer

4.3.3 Functionalized Multiwalled Carbon Nanotubes (MWCNTs) Coated Nylon 6 mat

Three different functionalized MWCNTs aqueous suspensions were prepared by adding 0.5wt% of carboxyl/amino/fluorine functionalized MWCNTs in distilled water in three separate vials. Using an ultrasonic bath, the MWCNTs suspensions are sonicated for 1 hour for homogenous dispersion of CNTs. The nylon mats are rolled and inserted in the CNTs dispersed suspension in the vials. 5wt% 2,2,2-Trifluoroethanol (TFE) is added into the solution to promote attachment of CNTs onto the Nylon NFs. The vials are then placed horizontally over a rolling machine and kept under rolling for 24 hours. Then they are pulled out followed by rinsing them with deionized water and dried at 60^{o}C for 12 hours.

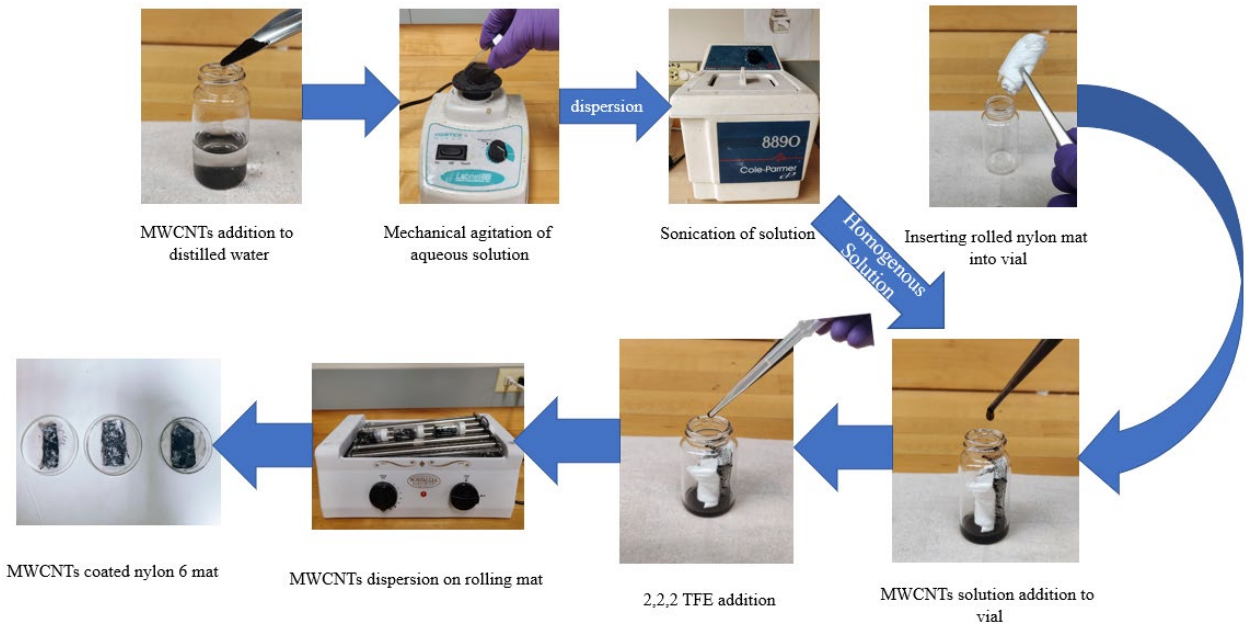

Figure 16: Preparation of functionalized MWCNTs coated nylon 6 fiber mats

4.4 Carbon Nanofibers (CNFs) Preparation

An OFT-1200 machine from MTI Corp has been used to perform heat treatment of the nanofibers. Before performing every heat treatment procedure for every sample, the inside of the tube furnace is cleaned with ethanol wetted Kim wipes. Then, the samples are placed inside the tube furnace on a thin ceramic square plate. Also, based on the polymer nature, a program containing different time length stabilization and carbonization temperature are set consequently.

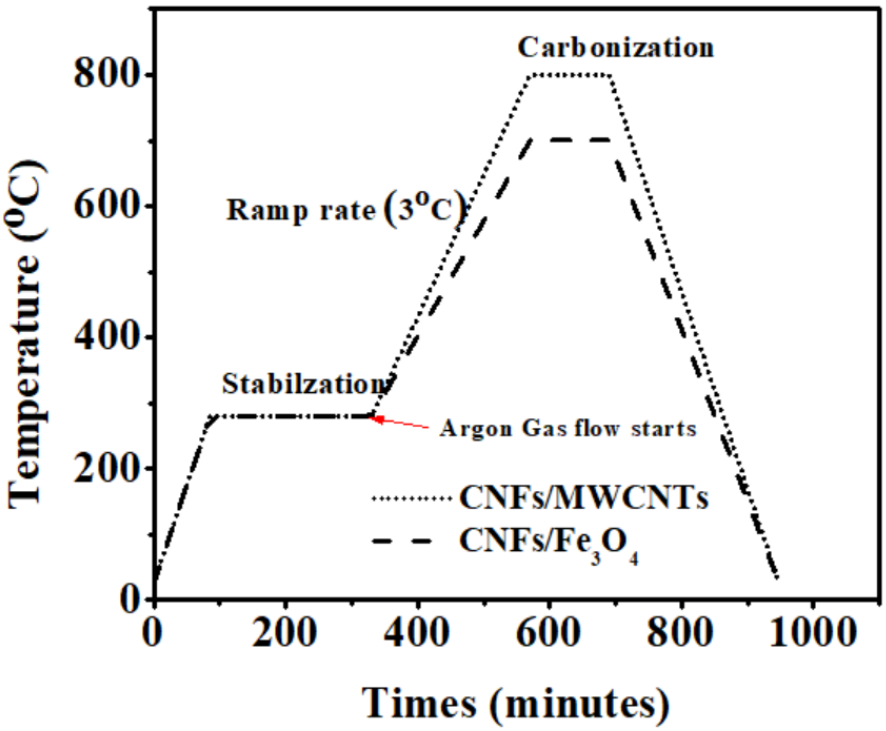

Figure 17: Heat treatment steps of NFs

4.4.1 Fe_3O_4 doped CNFs

The obtained force spun fibers are used to prepare pre-oxidized nanofibers. The fibers are heat-treated at the stabilization temperature at 280ºC for 6 hours. After 6 hours of stabilization temperature, both sides of the tube furnace are closed with a steel cap and argon flow is induced through the nozzle of the cap. The carbonization temperature was selected as 700ºC for 2 hours with the heating rate of $3^{o}C \cdot min^{-1}$ under an argon environment (Figure 17). As the temperature reaches room temperature, the argon flow is closely followed by taking out the CFs from the furnace.

4.4.2 MWCNTs doped CNFs

The obtained force spun fibers are used to prepare pre-oxidized nanofibers. The fibers are heat-treated at the stabilization temperature at 280ºC for 6 hours. After 6 hours of stabilization temperature, both sides of the tube furnace are closed with a steel cap and argon flow is induced through the nozzle of the cap. The carbonization temperature was selected as 800ºC for 2 hours with the heating rate of $3^{o}C \cdot min^{-1}$ under an argon environment (Figure 17). As the temperature reaches room temperature, the argon flow is closely followed by taking out the CFs from the furnace.

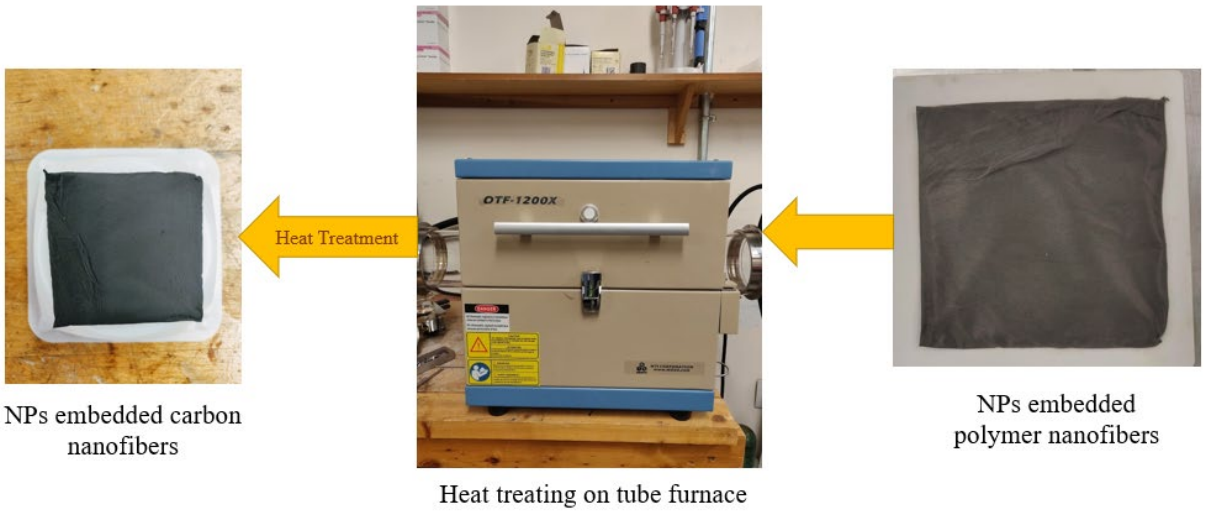

Figure 18: Carbon Nanofiber preparation

4.5 Preparation of Multilayered Composite (MLC)

To fabricate a multilayered composite of a single system, four different layers of fiber mat have been chosen from all the produced composite with a variety of nanoparticle percentages. The lay-up stacking sequence contains Carbon nanofibers with 10 wt% of Fe_3O_4, Nylon 6/MWCNTs-COOH, Nylon 6/PIn & Carbon nanofibers with 5 wt% of MWCNTs. Four laminates contained by the composites are denoted by MLC1 (multilayered composite 1) in a single system. For the

double system, the fabricated MLC2 (multilayered composite 2) contains a total of eight layers with the repetition of stacking the layers for the second time).

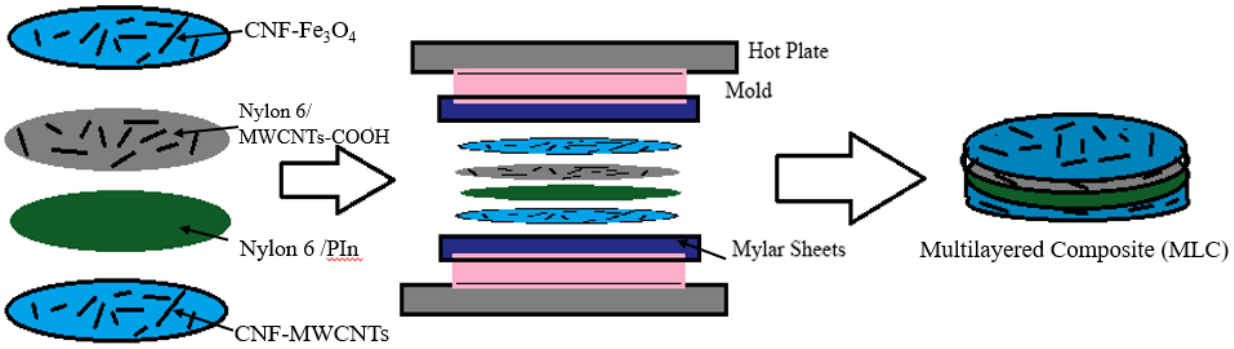

(a)

(b)

(c)

Figure 19: (a) Schematic representation of the fabrication process of multilayered composite; Digital picture of (b) & (c) a resultant MLC1(single system) from MWCNTs, Fe_3O_4 and PIn filled nanofiber mats

A liquid epoxy and curing agent were mixed in a 2:1 ratio according to weight percentage and placed between the interlayers to establish a bond between the surfaces. The composite was put inside a vacuum for 1 hour to eliminate the presence of air void trapped between layers. The stacked multilayers were compression molded at 7 MPa at room temperature for 24 hours. Mylar sheets were placed on the upper and lower side of the composite to avoid sticking to the compression mold.

4.6 Electromagnetic Interference (EMI) Shielding Testing

The EMI SE measurements were performed using a Hewlett-Packard 8712C network analyzer with a working frequency range from 0.3 MHz to 1300 MHz accompanying a procedure described by Vasquez et al. [195].

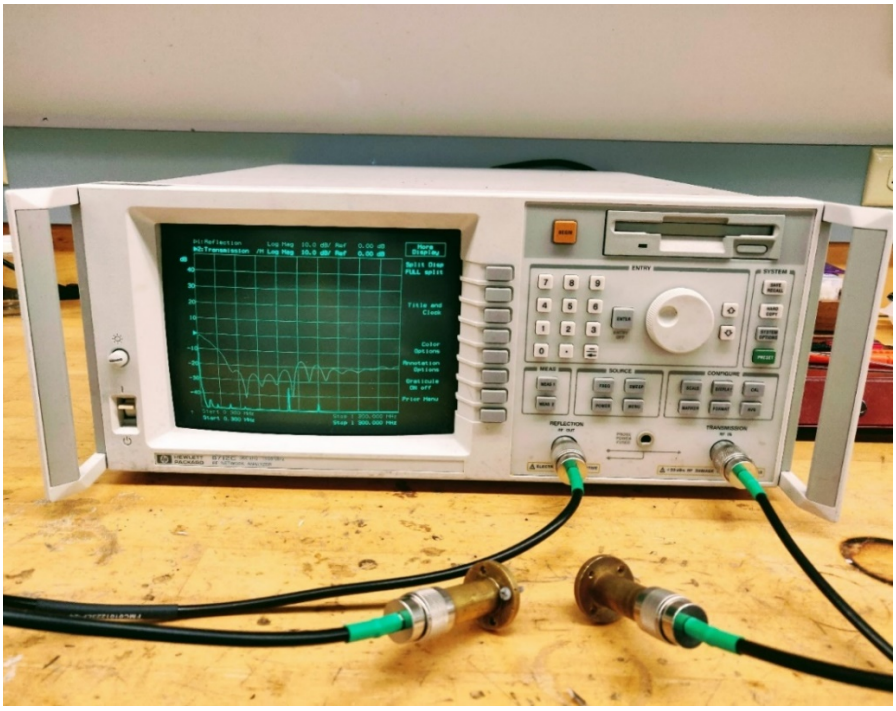

Figure 20: Vector network analyzer (VNA) set up for EMI shielding testing

In this procedure, a reference specimen and a loaded specimen from the same material were geometrically made according to the dimensions [15, 195](Figure 22) to be measured. The specimen is then placed in between two attenuators coupled with the coaxial cables to the VNA through which the EM signal goes through. The newly developed testers (Figure 21) minimize the complexity of previous testing procedure ASTM D4935-99 where the new tested can extract data using smaller sample at higher frequency [195].

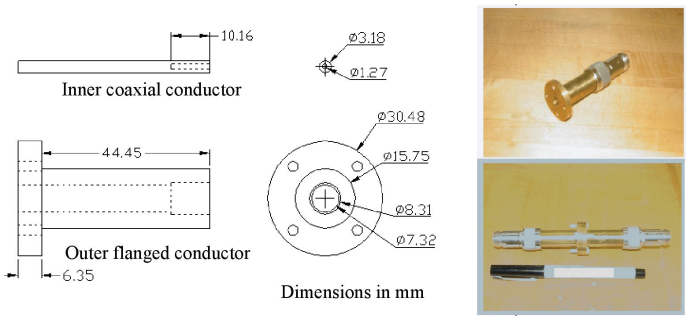

(a)

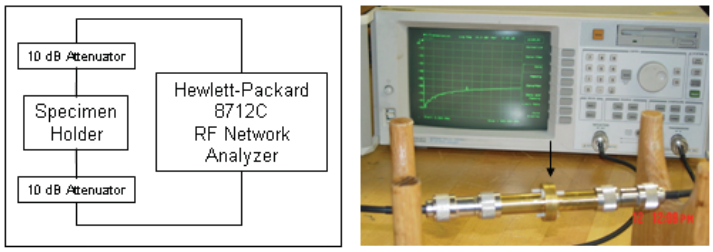

(b)

Figure 21. (a) Manufacturing drawing and photos of the newly developed SE tester (b) Setup of EMI SE testing [195]

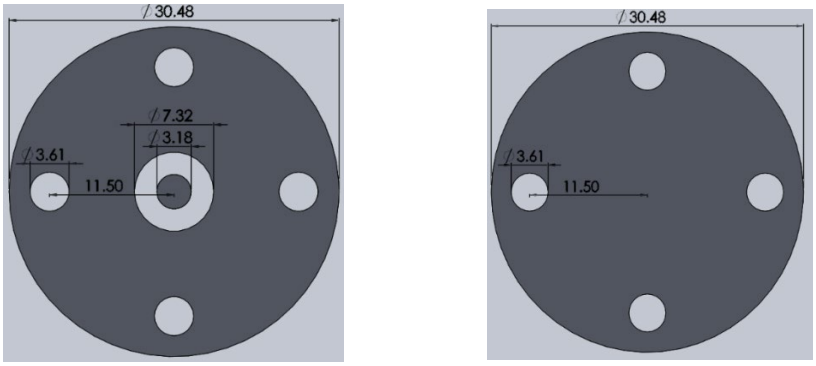

(a) **(b)**

Figure 22: (a) Reference (b) Load specimen (dimensions are in mm) for testing electromagnetic interference (EMI) shielding effectiveness[195]

4.7 Electrical Conductivity Testing

The surface resistivity of PANI, PIn coated Nylon 6, nanoparticles filled carbon nanofibers mats containing different percentage of magnetite and carbon nanotubes are measured using an R-CHEK RC2175 four-point probe surface resistivity meter (EDTM, Inc., Toledo, OH, USA) at room temperature. Ten measurements of sheet resistance at different locations in each sample were obtained to measure the average sheet resistance. The following equation has been used to calculate the in-plane conductivity from sheet resistance and the thickness (t in cm) of the sample. The electrical conductivity was measured using the four-point probe method with the following expression: [19]

$$\sigma = \frac{L}{t \times R \times w} \tag{24}$$

Where σ is the electrical conductivity in S/cm, R is electrical resistance in Ω/sq, t is the thickness of the sample, w is the width of the sample and L is the distance between electrodes (all in cm)

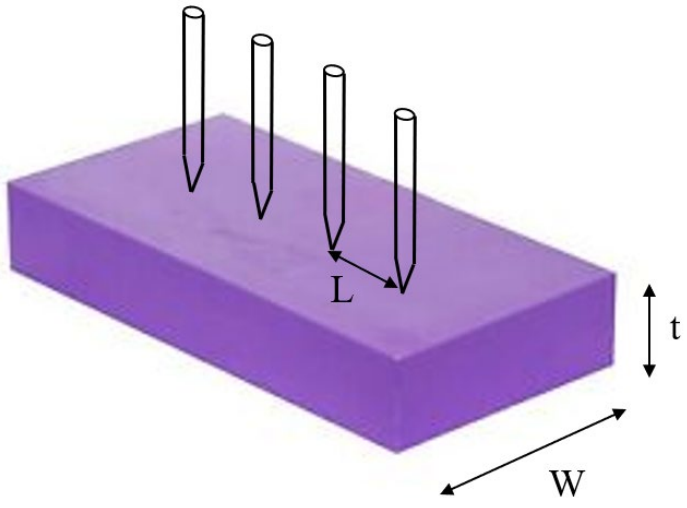

Figure 23. Four probe point mechanism

Figure 24: Four-point meter for in-plane conductivity measurement

4.8 Characterization

4.8.1 SEM analysis

The morphology, average diameter of fibers was investigated using a Zeiss EVO LS10 Electron Microscope operated at 1-3kV.

4.8.2 Electrical Conductivity Analysis

The samples' electrical conductivity was calculated by obtaining surface resistivity using the R-CHEK RC-2175 4-Point Sheet resistance meter from EDTM.

4.8.3 EMI SE Analysis

The samples' EMI shielding effectiveness was measured by a Hewlett Packard RF network Analyzer 8712C.

4.8.4 Energy Dispersive X-ray analysis (EDAX)

The elemental analysis of composite layers was investigated using a Zeiss EVO LS10 Electron Microscope operated at 6 kV.

CHAPTER V

RESULTS AND DISCUSSION

5.1 Fiber production

5.1.1 SEM Analysis

After the spun fibers are collected in the cardboard frame, the samples were gold-sputtered to produce a conductive surface for better morphology and elemental analysis depending on the nature of the coating variations. Controlled fibers need to be ensured better gold sputtering except for those fibers already having a conductive coating. The image provided below were taken using the Zeiss EVO LS10 Electron Microscope, with a charged voltage range from 1kV to 7kV, and an SE2 signal lens.

Figure 25 shows the control Nylon 6 fibers with or without the grafting of PANI and PIn conducting polymer. In figure 25 (a) & (b), the fibers are randomly oriented as the fibers are collected manually in different orientation pattern. They show a smooth surface morphology with some exceptions of beads in the fiber. The micrograph of Nylon 6/PANI fabric (Figure 25 c & d) shows a well deposited PANI on the fiber surface. According to the image, PANI on the fiber surface is evenly distributed and densely grafted along the length of the fiber. A further magnified view of the image (Figure 25 d) reveals a cluster form of nano morphology of PANI without confining to any specific shape. The micrograph also indicates PANI deposited onto the fiber mat consists of a continuous network of nanofibers while creating a rough surface.

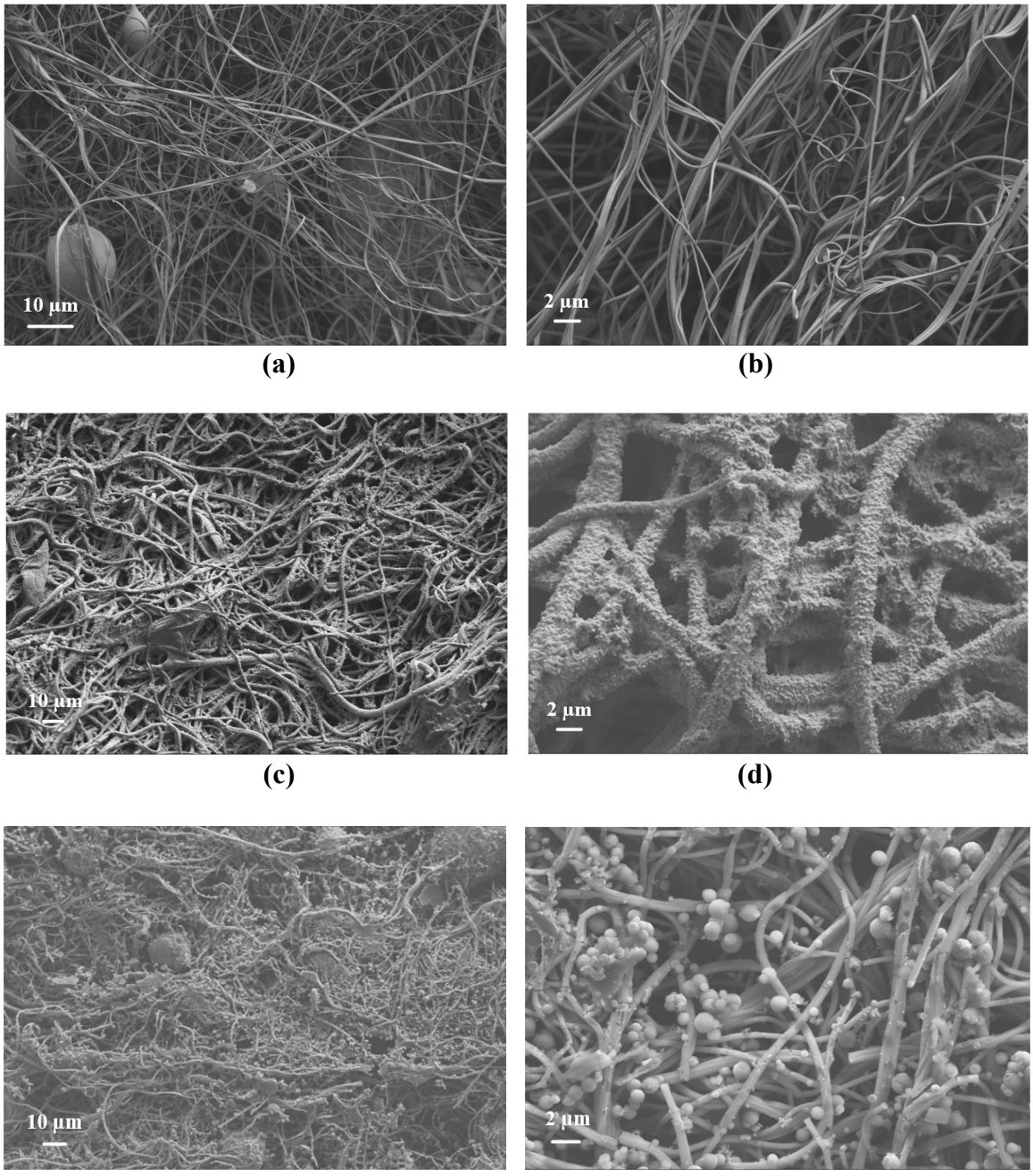

Figure 25: Fiber SEM micrographs at different scales (a) & (b) Nylon 6 control, (c) & (d)Polyaniline coated Nylon 6, (e) & (f) Polyindole (PIn) coated Nylon 6

Figure 25 (e) & (f) shows PIn grafted on nylon 6 fiber surface fabricated by chemical polymerization. It presents the globular or granular particles with rough morphology according to other reports [144, 196]. The obtained particles on the surface had a spherical agglomeration [143] shape within most of the fiber regions and some flaky shape. The density of PIn was observed to be higher due to the polymerization process associated with a high packed polymeric chain[197]. The incorporation of PIn NPs within the porous region did not hamper the regular interconnected network of the fiber. This morphology also appears to have a rougher texture, and the presence of alignment is lacking. Figure 26 shows the morphology of carboxylic functionalized multiwall carbon nanotube coated nylon 6 fiber. The fibers were not uniformly coated along their length (Figure 26 b). From the resultant structure, it can be observed that the wrapped CNTs on fibers are due to the addition of TFE (Figure 26 a). The pores on the Nylon surface were highly occupied by CNTs resulting negligible amount of mesopores. The mats may exhibit some micropores resulting from the CNTs, thus offer increased surface area. The alignment of fibers is more randomly oriented here compared to the control fiber.

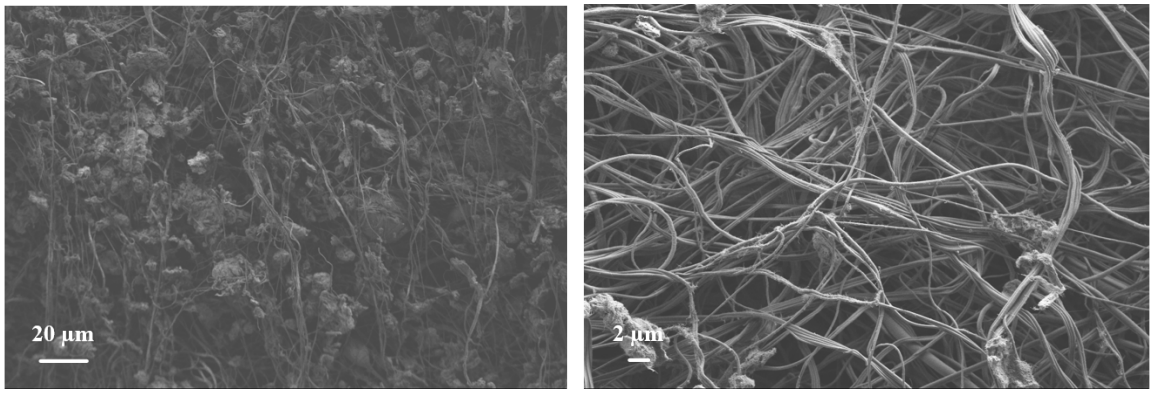

(a) **(b)**

Figure 26 : SEM images of (a) 500 X & (b) 2.00 KX magnification view of MWCNTs coated Nylon 6

Figure 27 shows the micrograph of control PAN fibers with or without different NPs contents. The control PAN fiber (Figure a & b) are more oriented in the same direction. Figure 27 (c) & (d) respectively showing MWCNTs and Fe_3O_4 embedded on PAN morphology resulting in aligned orientation. All the morphology exhibits a long, beadless, and continuous morphology. It is also observed that the homogeneity of the spun fibers was not affected by the addition of Fe_3O_4 or MWCNTs NPs. From Figure 27 (c) & (d) in SEM image of 5 wt% CNTs, 10 wt% magnetite sample, it appears that the NPs (CNTs and Fe_3O_4) are extruded out from the polymer matrix and wetted by the PAN polymer matrix. The NPs are well dispersed in the matrix without any aggregation.

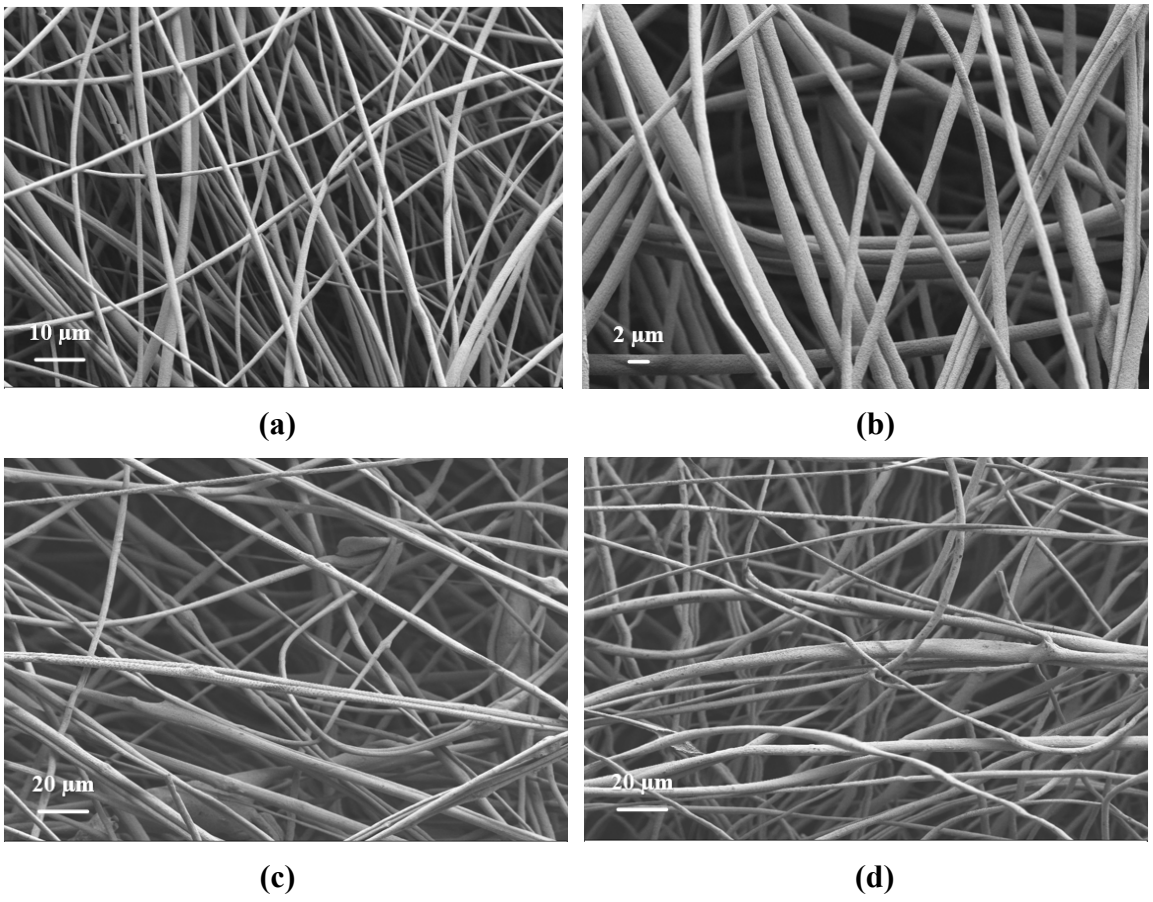

Figure 27 : SEM micrograph of (a) & (b) control PAN NFs (c)PAN/MWCNTs (5 wt%) (d) PAN/Fe_3O_4 (10 wt%)

Figure 28 represents the SEM image of the carbonized PAN with or without magnetite/CNTs at two different temperatures (700ºC & 800ºC). The fibers are aligned in a different direction, meaning they are randomly oriented. Both CNFs at both the temperature maintain the continuous fiber network within the surface while the Fe_3O_4 doped CNFs shows discontinuity of fiber with many porous regions along the length (Figure 28 b). Some rough surface appears in CNF fiber at a carbonizing temperature of 800ºC due to the rapid evaporation of residual solvent during the pyrolysis process (Figure 28 c). The reason for the residual solvent is due to the particle presence along the fiber network promoting the slow rate of solvent evaporation during spinning (vapor-induced phase separation)[157, 198]. In Figure (d), it appears that the MWCNTs are entrapped within the nanofiber network. The volatility of DMF may promote surface roughening of PAN fiber.

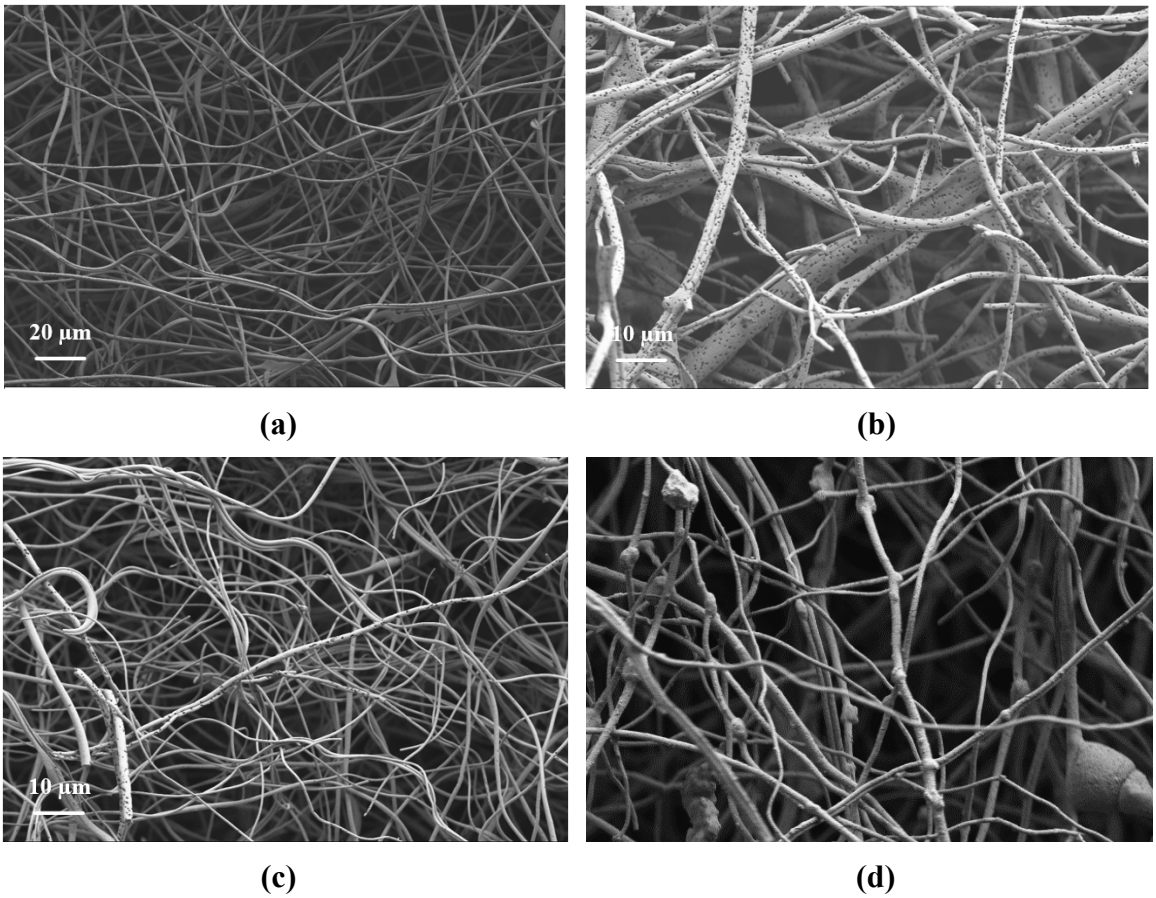

Figure 28 : SEM micrograph of (a) CNF (b) CNF/Fe_3O_4 (10 wt%) carbonized at 700ºC (c) CNF (d) CNF/MWCNTs (5 wt%) carbonized at 800ºC

The evaporation of DMF did not occur completely, the CNTs particles contained solvent traces residing inside them before their deposition. The aggregation off-MWCNTs is less likely to be occurred due to their good dispersion capability in the solvent while enhancing their affinity towards the polymer[139] with a formation of interfacial bonding[199]. The CNTs were well aligned along the axis of the nanofibers as the CNTs along with the polymer traveled through the spinneret and the orifice promotes the alignment of the polymeric molecular chains as well[158].

5.1.2 Fiber diameter analysis

The average fiber diameter and other associated data are based on the measurements obtained on over 120 fibers per sample with random image sampling.

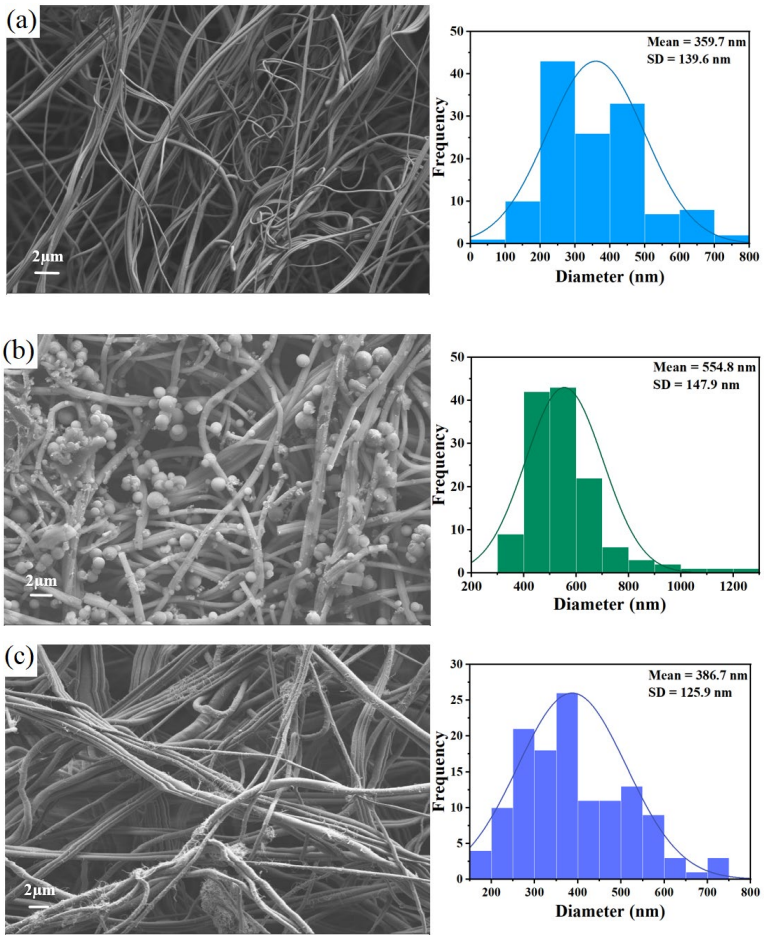

Figure 29 : Diameter distribution of (a) Nylon 6, (b) PIn & (c) MWCNTs-COOH decorated Nylon 6 fiber mat

Figure 29 shows the corresponding diameter distribution of Nylon 6 NFs and conductive polymer NPs, CNTs doped Nylon NFs. Nylon 6 has a randomly oriented, continuous morphology with a mean diameter of 360 nm with a standard deviation of 140 nm (Figure 29 a). After the incorporation of PIn NPs by in-situ polymerization, a well-distributed coating over the Nylon 6 surface was observed resulting in the fiber diameter increased about 555±148 nm (Figure 29 b). As shown in Figure 29 (c), a slight increase in the mean diameter of approximately 387±126 nm was displayed in the MWCNTs doped nylon 6.

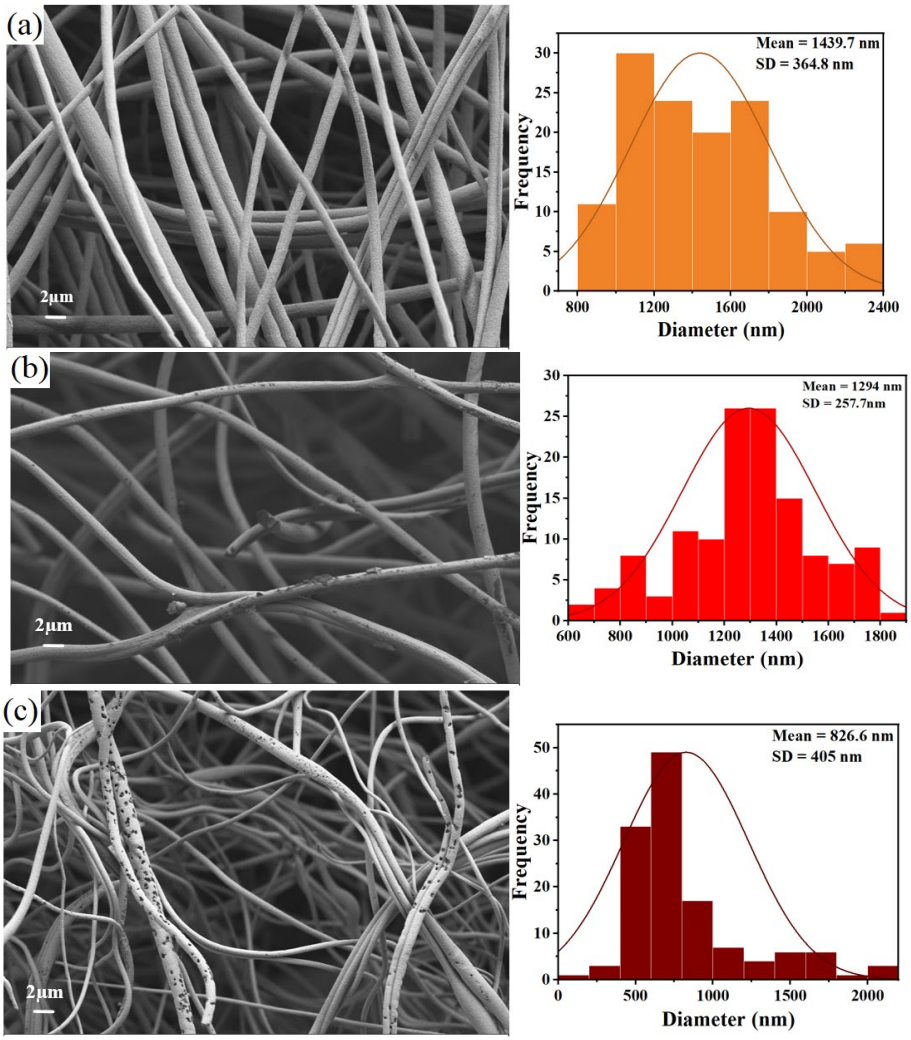

Figure 30 : Diameter distribution of (a) PAN NFs, (b) CNFs at 700ºC (c) CNFs at 800ºC

The diameter distribution of PAN NFs, NFs carbonized at two different temperature contents is shown in Figure 30. PAN NFs exhibits a continuous interconnected network with an average diameter of 1440 nm (Figure 30 a). The diameter of CNFs at 700ºC & 800ºC gradually reduced to 1294±258 and 827±405 nm respectively. The shrinkage of fiber diameter happens due to the heat treatment for removal of organic compound[155], sintering[185], or pyrolysis[200, 201]. Figure 31 shows, the fiber diameter of CNFs/Fe_3O_4 and CNFs/MWCNTs which are 2064±1052 and 1638±381 respectively. In addition to nanoparticles in the polymer solution increases the surface tension of the jet ejecting from the spinneret nozzle resulting in large diameter fiber (Figure S1). For loading of magnetite, the size of the Fe_3O_4 may increase during the carbonizing process [201] causing the rise of the diameter of the CNFs/Fe_3O_4 sample (Figure 31 a). The addition of filler (MWCNTs) can increase the viscosity of polymer solution promoting fiber diameter increase [137] (Figure 31 b).

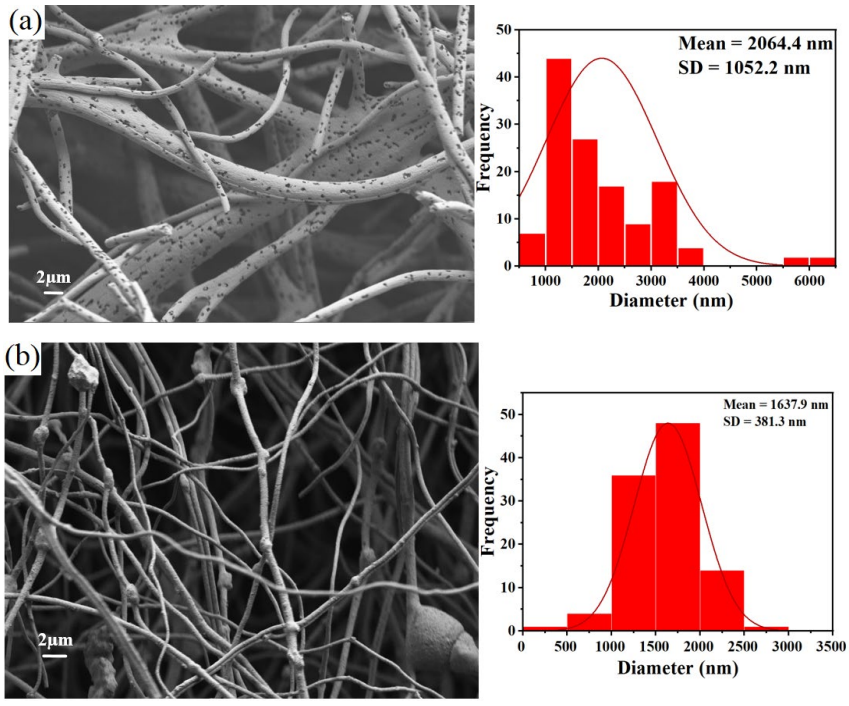

Figure 31 : Diameter distribution of (a) CNFs/Fe_3O_4 at 700ºC, (b) CNFs/MWCNTs at 800ºC

SEM micrographs of some of the developed polymer composites are shown in Figure 32. PIn embedded nanofibers are appeared across the cross-sections exhibiting a homogenous dispersion (Figure 32 a). To promote percolation homogenous dispersion is needed to develop a conductive network [15]. In Figure 32 (c), the nylon mat layers are parallelly intercalated between the CNFs layers. Three interfaces of four layered composite is visible in the SEM view (Figure 32 c). Different magnification of sectional view was presented on figure S3 (Appendix A).

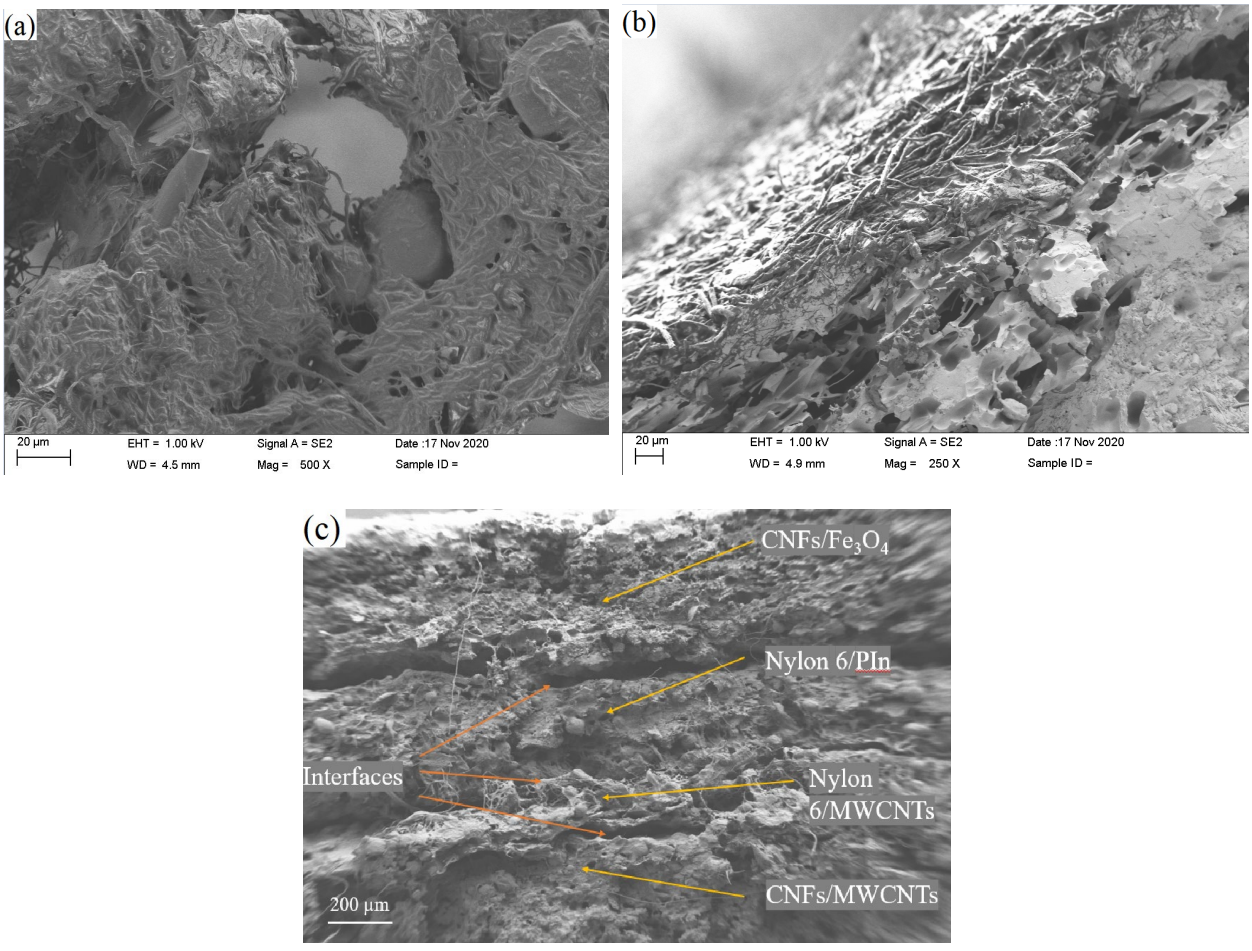

Figure 32. SEM image of cross-section of (a) PIn Embedded NFs mat (b) Carbon Nanofibers (CNFs) intercalated with nylon mat layer (c) Four layers of multilayer composite showing stacked sequence

5.1.3 EDAX Analysis

From figure 33, the elemental mapping has been performed on the multilayered composite in order to differentiate the layers. The (a) layers shows random dispersion of magnetite with some aggregation. The aggregated area shows a higher amount of Fe with the presence of oxygen. The next layer from bottom to top (b) presents higher percentage of nitrogen content due to the presence of PIn Nps while the nitrogen in the nylon 6 is also contributing to this region. The layer (c) has a great amount of oxygen content with a slight increase of carbon content due to the carboxyl group attached to the CNTs. Some traces of nitrogen are visible as amide group of nylon structure is present. In the layer (d), due to the high temperature carbonization of nanofiber and the presence of carbon nanotube, the carbon percentage is superior compared to the and other elements. A slight presence of oxygen could possibly occur from the interfacial area of the

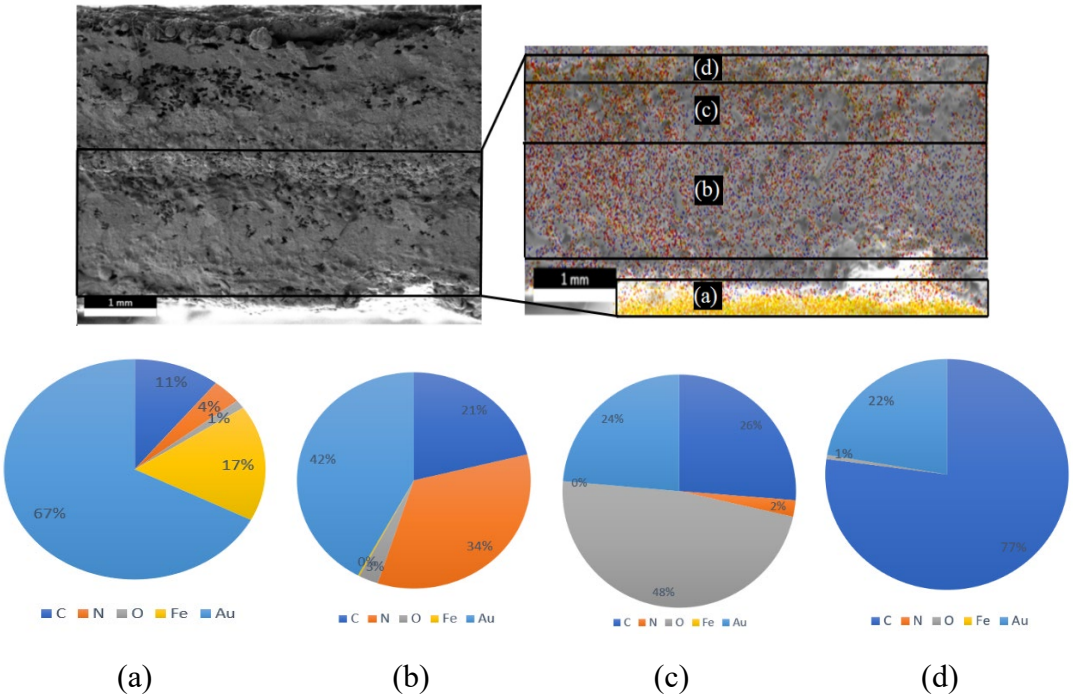

Figure 33. Elemental Analysis of (a) CNFs/Fe_3O_4 (b) Nylon 6/PIn (c)Nylon 6/MWCNTs-COOH (d) CNFs/MWCNTs of the Multilayered Composite (MLC)

adjacent layers of magnetite or carboxylated carbon nanotubes.

5.2 EMI Shielding Analysis

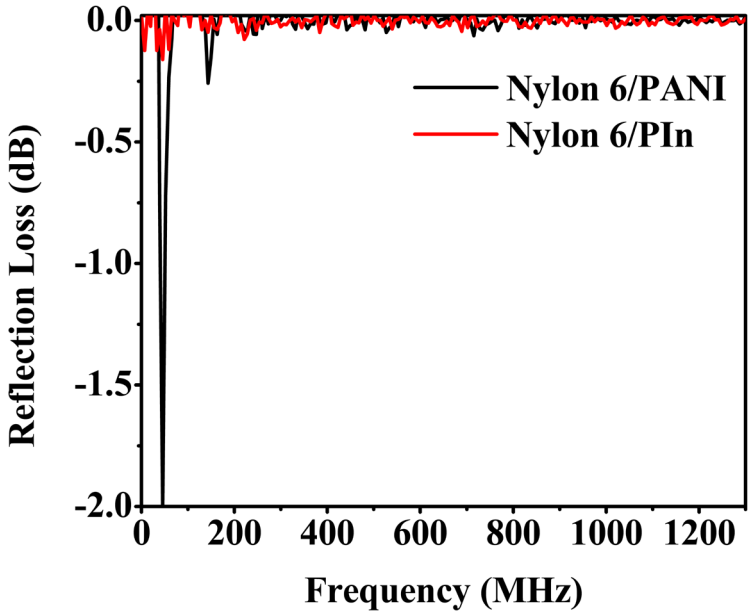

(a)

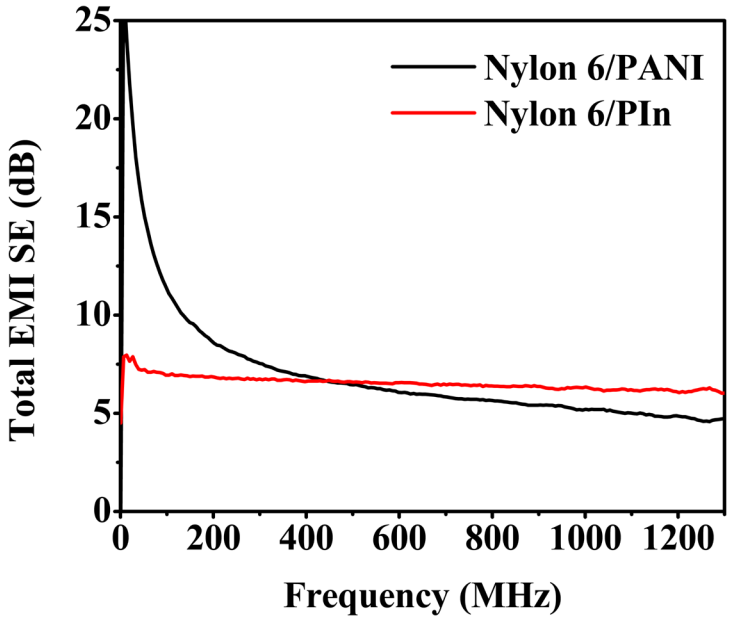

(b)

Figure 34 : (a) Reflection loss & (b) Total EMI Shielding Effectiveness of Nylon 6/PANI, Nylon 6/PIn

As observed in Figure 34, conducting polymer (PANI or PIn) coated Nylon 6 shows absorption dominant shielding mechanism as almost no reflection loss was observed along with the frequency range. The shielding of Nylon 6/PANI starts to decrease with the increase of frequency and went lower compared to Nylon 6/PIn at a higher frequency. Though conductivity doesn't always play a direct role to enhance EMI shielding, the density of the charge-carrying surface may contribute greatly in this regard. The PIn NPs within the surface increase the interfacial sites. Multiple reflections are most likely to occur as the total shielding for both composites is less than 10 dB.

Figure 35 displays the EMI SE for Nylon 6 mat coated with different functionalized MWCNTs. The minimum reflection loss of -30.737 dB and -29.881 dB was observed at 812.612 MHz, and 403.207 MHz respectively for Nylon 6/MWCNTs-NH_2 (Figure 35 a) with 1.136 mm thickness (Table 7) which depicts over 90 percent EM microwave absorption. The plot also shows the higher aspect ratio (L/D) of carboxyl functionalized CNTs (>1250-3750) compared to amine-functionalized CNTs (>50-600) has shown more reflection other than wave absorption. From Figure 35 (b), MWCNTs-COOH coated nylon mat shows more shielding performance around 10 dB more than Nylon 6/MWCNTs-F or Nylon 6/NH_2 fiber mat. The carboxyl group present in the MWCNTs-COOH can readily react with the amine group in nylon[202]. Also, this oxygen-containing functional group induces solubility in the polar solvent. This may create a more affinity between fiber and nanoparticles leading to a well-coated surface with conductive properties. The MWCNTs-COOH was able to form the continuous conductive network through covalent adsorption on the surface of Nylon 6. Therefore, the surface conductivity is 5 times higher than the MWCNTs-NH_2 coated mat (Table 7). Nylon/MWCNTs-F has an EMI shielding value of 3-7dB in the 200-1300 MHz range.

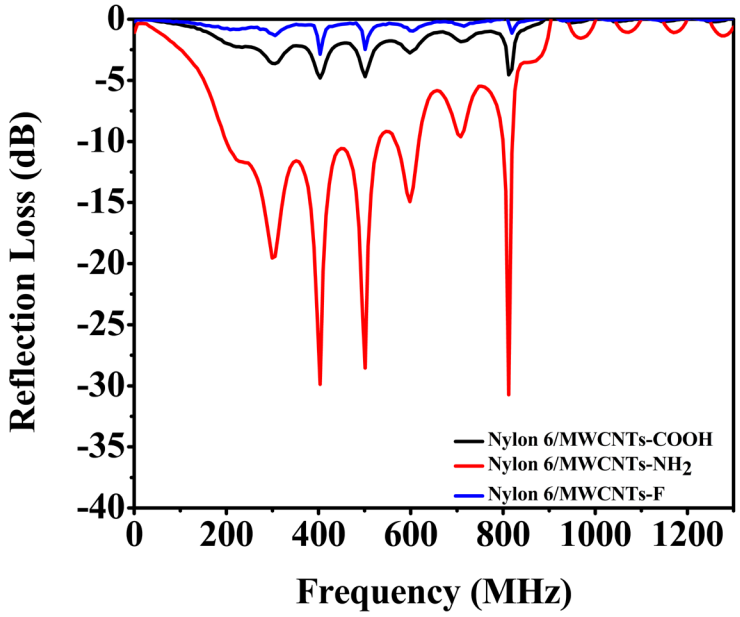

(a)

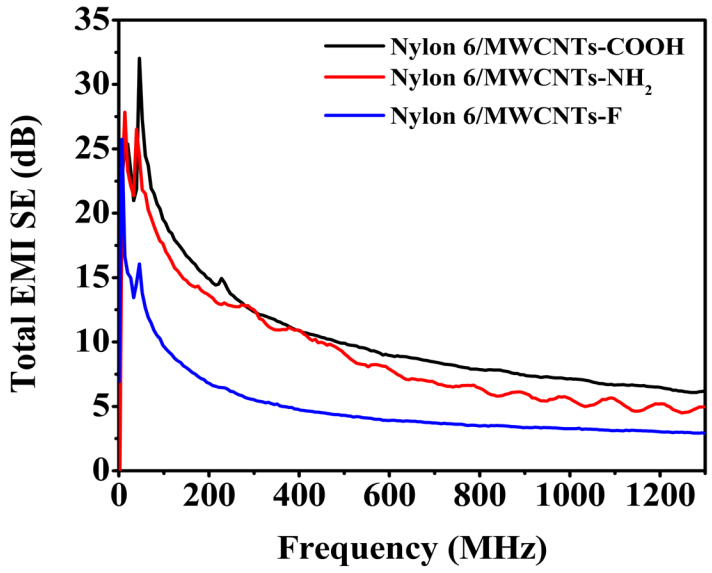

(b)

Figure 35 : (a) Reflection Loss & (b) Total EMI Shielding Effectiveness of Nylon 6/MWCNTs-COOH, Nylon 6/MWCNTs-NH2, and Nylon 6/MWCNTs-F

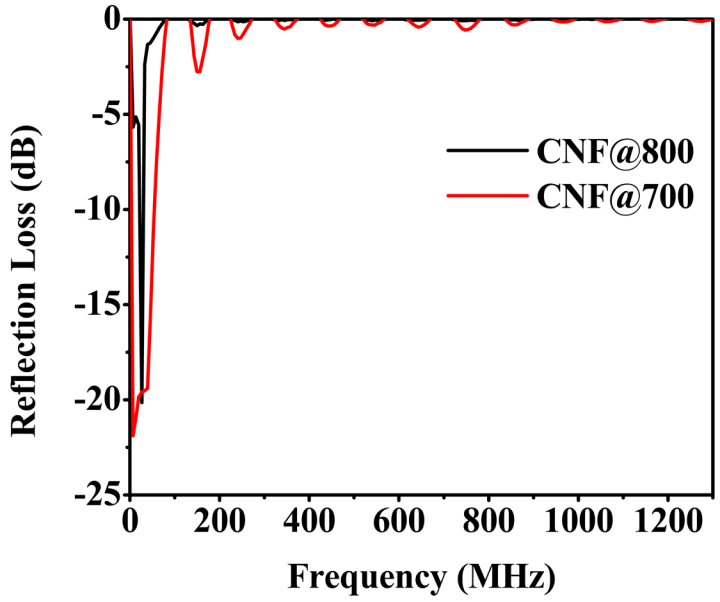

(a)

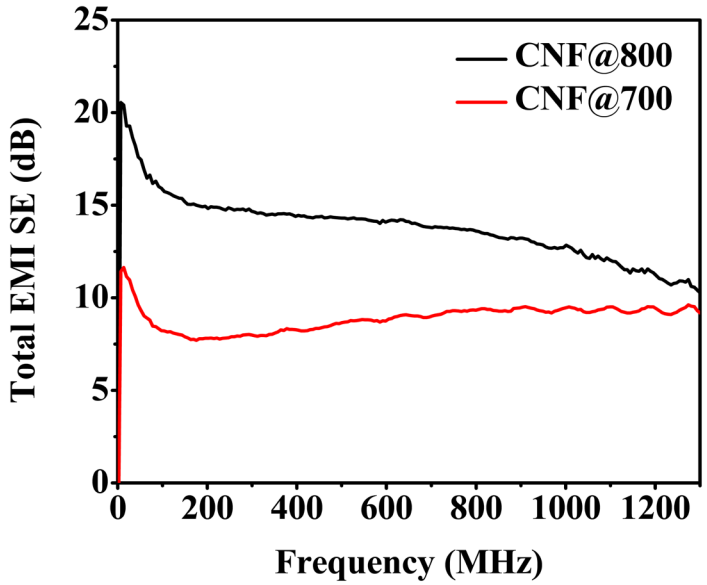

(b)

Figure 36 : (a) Reflection loss & (b) Total EMI Shielding Effectiveness of CNF@800 & CNF@700

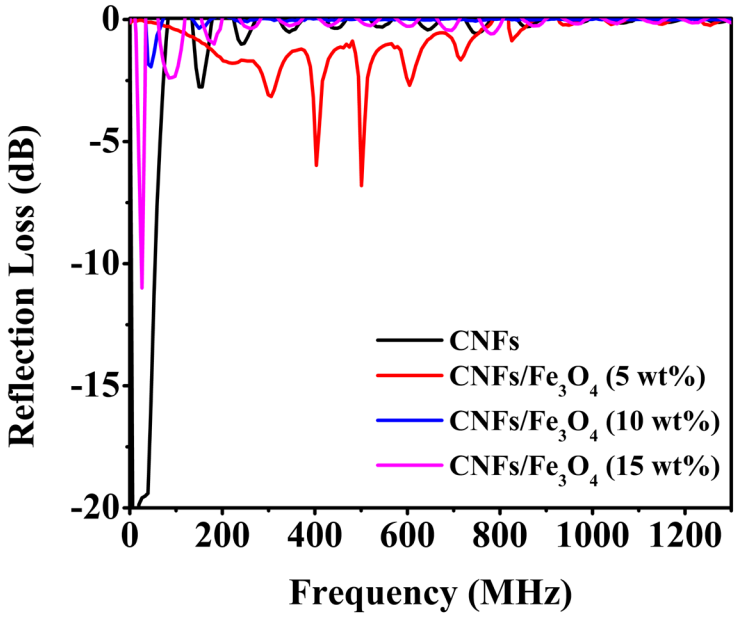

(a)

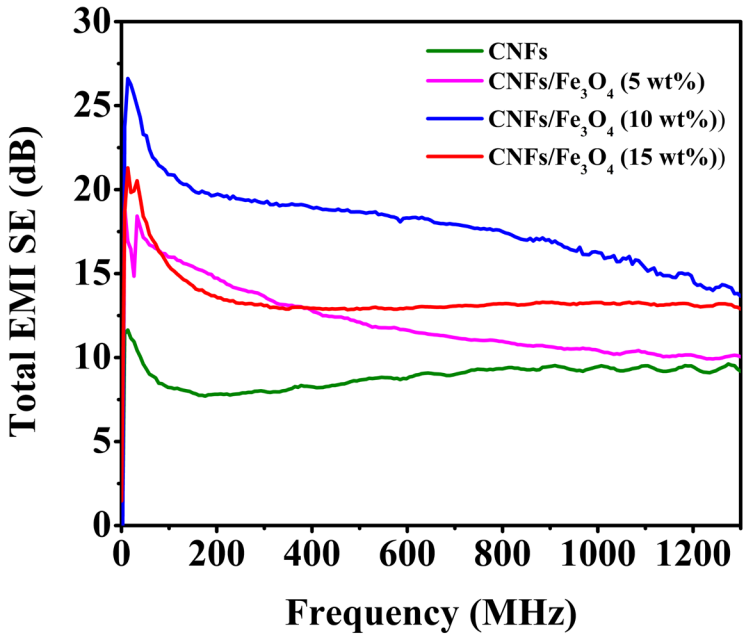

(b)

Figure 37 : (a) Reflection loss & (b) Total EMI Shielding Effectiveness of CNF with 0, 5,10,15 wt % of Fe_3O_4

In figure 36, temperature dependency on the shielding carbon nanofibers was presented. The shielding performance of CNFs increased with increasing the pyrolysis temperature from 700 to 800ºC as the degree of graphitization enhanced at the higher temperature. When the pyrolysis temperature of CNFs is 700ºC, the shielding is 10 dB or less, for which some reflection loss peak was observed in the reflection curve (Figure 36 a). CNF at 800ºC shows enhanced total shielding of 11 to 15 dB (Figure 36 b) or an average of 14 dB (Table 11) while showing a reflection dominant mechanism with no reflection loss.

In Figure 37, CNFs with 10 wt% loadings of Fe_3O_4 reached to total EMI shielding of 15 dB to 20 dB, greater than 5 wt% loadings in the frequency range of 0.2 to 1.3 MHz range. The reason could be the enhanced surface conductivity (Table 8) due to enhanced graphitization during heat treatment [201]. The complex permittivity enhancement due to the addition of NPs might play another contribution. With the increase of filler loading, less EMI shielding performance is obtained which is around 13 dB for 15 wt% loadings of magnetite. Aggregation of Fe_3O_4 NPs is a possible phenomenon due to its strong magnetic particle interaction [22] causing the lack of proper dispersion of additional filler loading to obtain a homogenous distribution within the fiber matrix and reduces their superparamagnetic properties [68]. The excess filler loading might also hamper the formation of the graphite layer [29]. From SEM (Figure S2) micrograph, CNF/Fe_3O_4 displays porous structure offering wave absorbing characteristics [39]. The number of pores on CNF/Fe_3O_4 (10wt%) is larger compared to the other magnetite percentage. This interstitial sites such as pores often are required for interface polarization and multiple scattering [19, 123, 126].

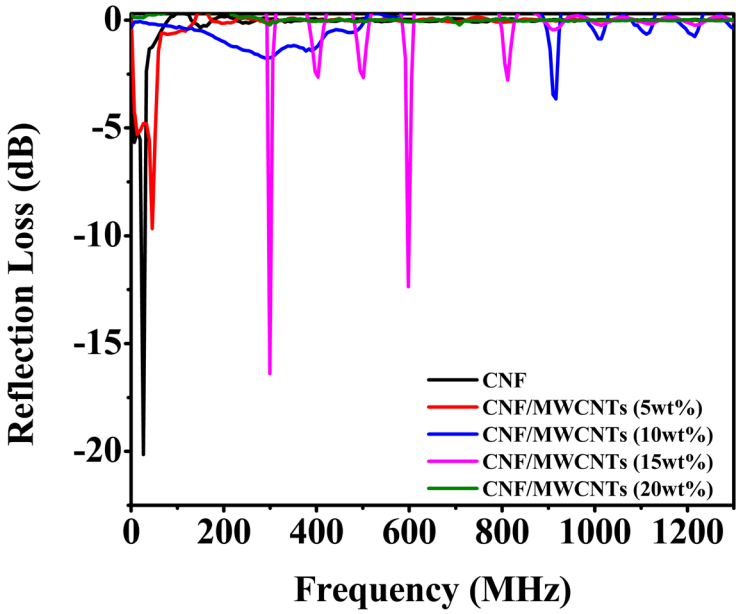

(a)

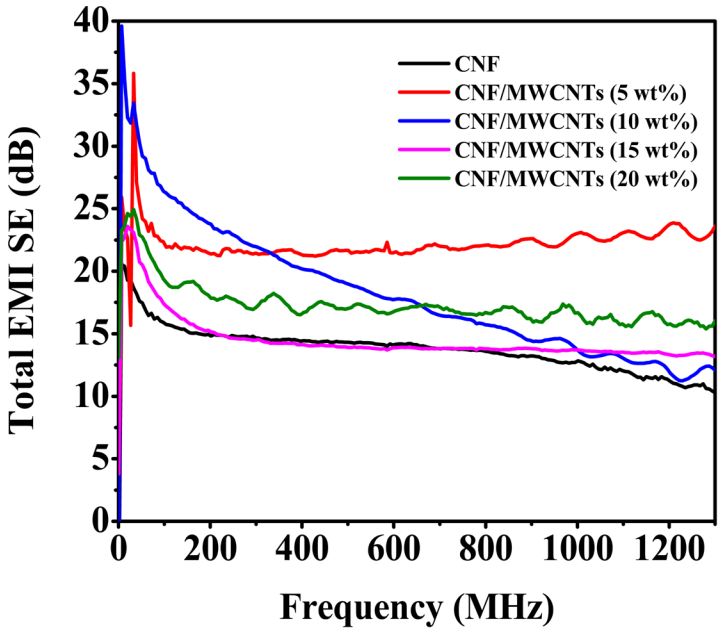

(b)

Figure 38 : (a) Reflection Loss & (b) Total EMI Shielding Effectiveness of CNF, CNF/MWCNTs(5 wt%), CNF/MWCNTs(10 wt%), CNF/MWCNTs(15 wt%) & CNF/MWCNTs(20 wt%)

Figure 38 shows the variation of the EMI SE of CNFs/MWCNTs nanocomposites on various MWCNTs loading with frequency under consideration. CNFs loaded with CNTs show enhanced shielding performance than neat CNFs (at 800°C). 5 wt% addition of MWCNTs was showing the highest EMI shielding of 21-23 dB. A further addition to CNTs (10 wt %), shielding increases to 21-25 dB on a frequency less than 300 MHz. Then in the frequency range 300 MHz-1.3 GHz, the shielding reduces from 21-12 dB. For 15 wt % CNTs addition. Some minimum reflection loss peak appears on 300 MHz & 600 MHz for 10, 15 wt% addition of MWCNTs depicting their absorption mechanism in the corresponding frequencies. A further addition to CNTs (20 wt%),

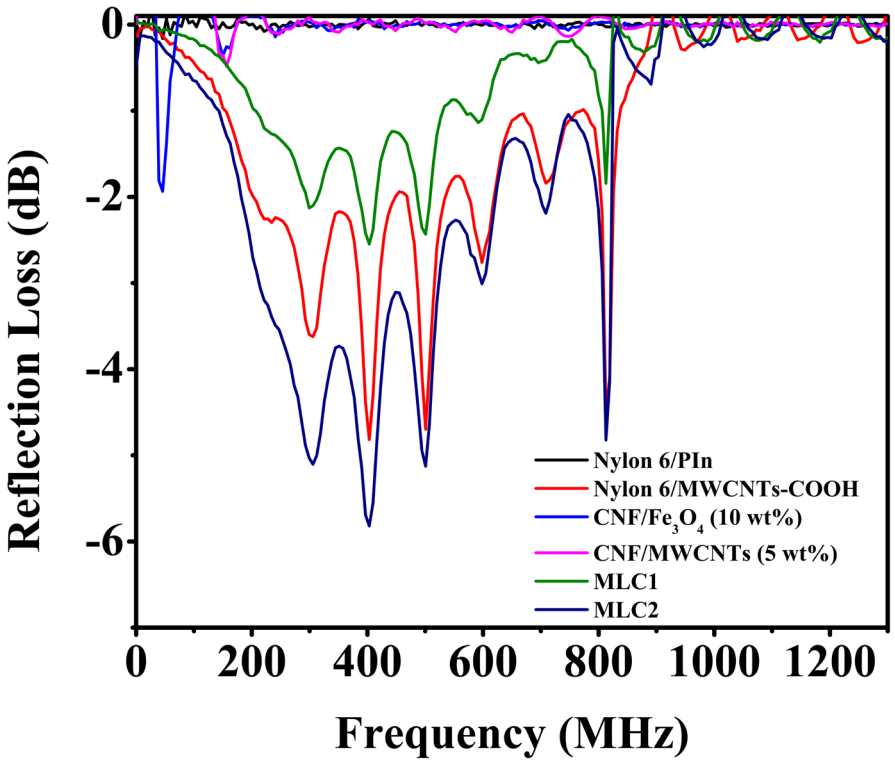

Figure 39: Reflection Loss of Nylon 6/PIn, Nylon 6/MWCNTs-COOH, CNF/Fe_3O_4 (10 wt%), CNF/MWCNTs (5 wt%), Multilayered Composite 1 (MLC1) & Multilayered Composite 2 (MLC2)

the reflection loss diminishes which displays CNFs/MWCNTs (20 wt%) has a reflection dominant mechanism. A similar type of reflection loss peaks for nylon-MWCNTs, MLC 1, MLC 2 were observed at the frequency of 305, 403, 500, and 812 MHz (Figure 39). This means that the nylon 6/MWCNTs were perfectly embedded within the stacked layered composites along with other layers without losing its contribution to the wave absorption mechanism. The minimum reflection loss recorded for MLC 2 was -5.82 dB in 403 MHz. Nearly about 73 percentage of absorption is obtained from MLC 2.

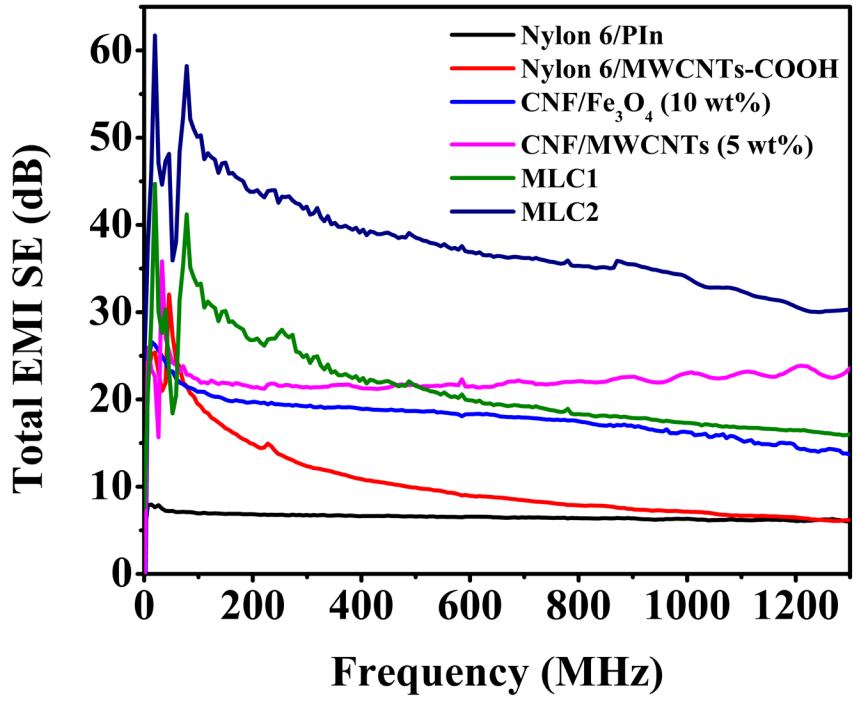

Figure 40: Total EMI Shielding Effectiveness of Nylon 6/PIn, Nylon 6/MWCNTs-COOH, CNF/Fe_3O_4 (10 wt%), CNF/MWCNTs(5 wt%), MLC 1 & MLC 2

Figure 40 shows the shielding performance of the selected layers and their multilayered composite materials. Multilayered composite 1 (MLC 1) composed of PIn, CNTs, Fe_3O_4 shows an ability to perform above 25 dB in the frequency range less than 500 MHz. Above 500 MHz frequency, EMI shielding dropped below the EMI shielding of the single CNF/MWCNTs layer

and slightly above the shielding value of CNF/Fe_3O_4. During the compression process, the reduction of the thickness of the CNFs layers caused the decrease of pore volume inside the composite resulting in less entrapped air and enhancing density. Thus, the percolation threshold did not remain the same with a similar amount of filler loading for which interfacial tension between polymer-filler decreases [35]. The eight layers composite (MLC 2) exhibits total shielding from 30 to 45 dB with the decrease of frequency.

From figure 41, theoretical reflection and absorption values are calculated from equation (8) & (9). The absorption for the samples is rising with the increase of the thickness of the samples and frequency, but the contributions are smaller compared to the reflection contribution (Figure 41 b). The average EMI SE of eight-layer containing MLC 2 was around 38 dB experimentally when the calculated SE was ~12 dB. Apart from these two contributions, multiple reflections could occur in these types of systems. The skin depth and distance from reflection to the surface have a relationship that is attributed to the multiple reflections. The skin depths of the samples are obtained from the following equation:

$$\delta = \frac{1}{\sqrt{\pi f \mu \sigma}} \tag{25}$$

In Figure 41 (d), the skin depth for the samples is reducing as the frequency is increased. In the figure, the material with higher electrical conductivity and thickness, the skin depth is calculated lower values. In the multilayered composite, even if the thickness and conductivity are higher, the skin depth is smaller than some of the other sample depth. A skin-effect phenomenon is occurring for the CNF/MWCNTs (10 wt%) which is experiencing a higher rate of decrease in shielding compared to the other CNFs with different MWCNTs percentages (Figure 38 b). For this sample, the skin depth (Figure 41 d) is approaching its thickness (Table 9) and at the higher

frequency, it tends to be smaller than the thickness of the material resulting in multiple reflections.

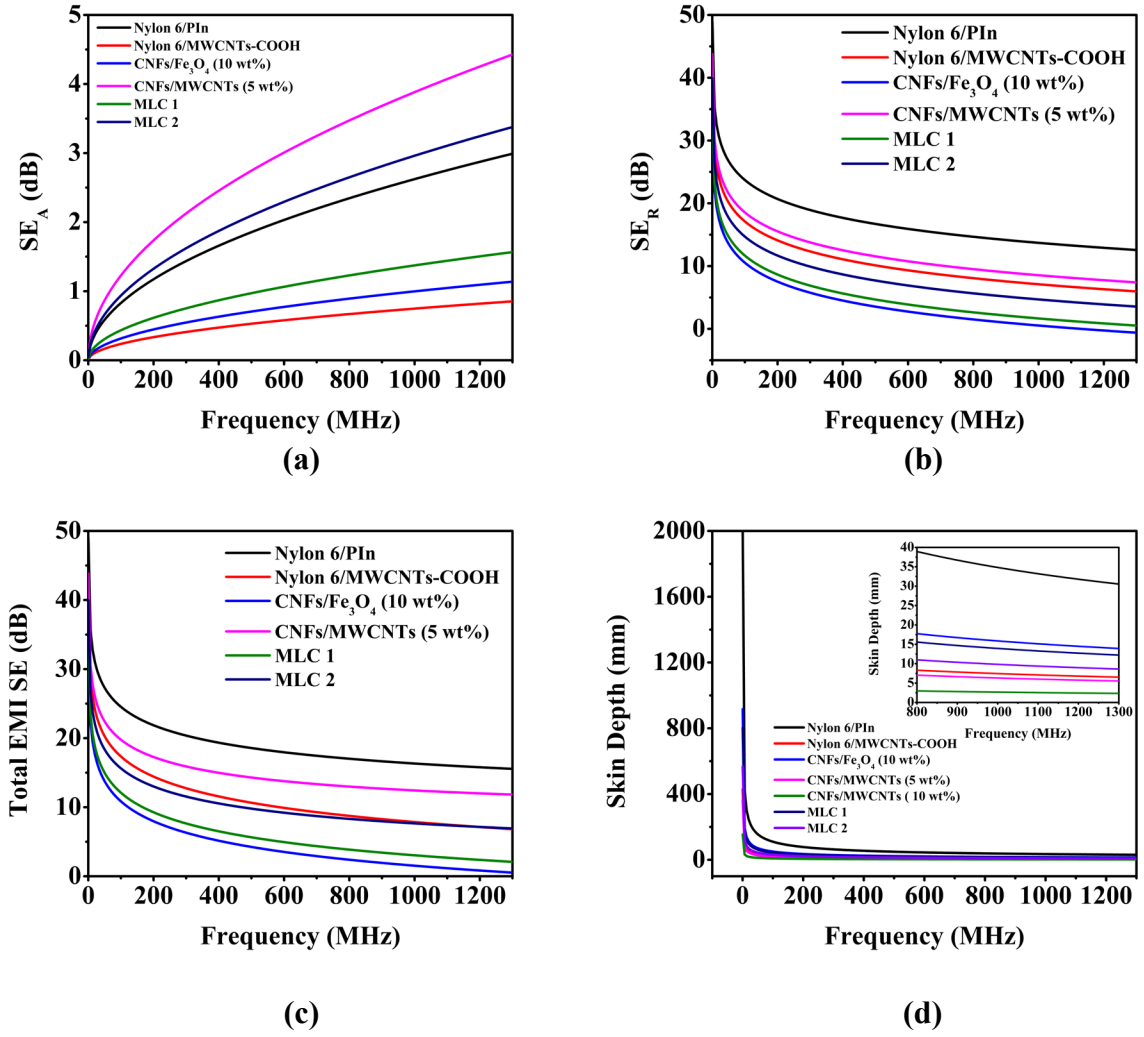

Figure 41 : Calculated EMI SE vs Frequency (a) SE_A (b) SE_R (c) Total EMI SE of Nylon 6/PIn, Nylon 6/MWCNTs-COOH, CNF/Fe_3O_4 (10 wt%), CNF/MWCNTs(5 wt%), CNF/MWCNTs(10 wt%), Multilayered Composite 1 (MLC 1) & Multilayered Composite 2 (MLC 2) (d) Skin depth with respect to frequency. The inset in (d) represents a zooming view of skin depth at a high frequency from 800 to 1300 MHz.

5.3 Electrical Conductivity Analysis

Table 7. Values of in-plane and through-plane electrical resistivity/conductivity of developed Nylon coated composites

Coated Material	Thickness (cm)	Resistivity (Ω·cm)	Conductivity ($S \cdot cm^{-1}$)
Nylon 6/PANI mat	0.04	30	0.033
Nylon 6/PIn	0.11	4.8	0.21
Nylon 6/MWCNTs-COOH	0.07	22	0.05
Nylon 6/MWCNTs-NH_2	0.14	113	0.009
Nylon 6/MWCNTs-F	0.12	108	0.01

The electrical conductivity of all the samples was measured using a four-point probe. It is observed in Table 7 that the nylon 6 mat PIn shows greater conductivity than the Nylon 6/PANI mat. MWCNTs-COOH coated nylon is showing superior performance in electrical conductivity than the other functionalized MWCNTs coated mat.

From Table 8 & 9, carbon nanofiber obtained from 700ºC and 800ºC carbonizing temperature, electrical conductivity increase from 0.01056 to 0.01299 S/cm which can be attributed to an increasing degree of graphitization at higher pyrolysis temperature [201].

From Table 8, the addition to 5 wt% magnetite shows a reduction of conductivity due to hindering the continuity of the fiber network. Further 10 wt % addition to Fe_3O_4 decrease in surface resistivity is due to the possible catalytic graphitization of carbon. Again, it appears that a further increase of filler loading of 15 wt% and 20 wt% gradually enhances the resistivity by building non-conducting separation between the fibers [29]. Then, extra addition in filler loading gradually reduces the conductivity as the non-conducting separation increases.

Table 8. Values of electrical resistivity/conductivity of developed CNFs/Magnetite composites

Sample Material	Thickness (cm)	Resistivity (Ω·cm)	Conductivity ($S \cdot cm^{-1}$)
CNF@700	0.154	94.7	0.011
CNF/Fe_3O_4(5wt%)	0.172	135.7	0.0074
CNF/Fe_3O_4(10 wt%)	0.182	99.41	0.01
CNF/Fe_3O_4(15 wt%)	0.18	119.74	0.008
CNF/Fe_3O_4(20 wt%)	0.1955	152.6	0.007

From table 9, 5 wt% addition of CNTs increases the conductivity by five times than control CNFs. The addition of CNTs (10 wt%) drastically improved the conductivity as the formation of a strong conducting network was formed. Then, it gradually decreases with the increase of the CNTs loading as there is a possibility of the hindrance of the continuity of the fiber conductive path. As the number of layers is increasing, the trapped air between the interfaces increasing along the direction of thickness of the materials causing a reduction in conductivity. MLC 2 is showing less electrical conductivity than MLC 1 (Table 10).

Table 9. Values of electrical resistivity/conductivity of developed CNFs/ MWCNTs composites

Sample Material	Thickness (cm)	Resistivity (Ω·cm)	Conductivity ($S \cdot cm^{-1}$)
CNF@800	0.14	77	0.013
CNF/MWCNTs (5 wt%)	0.28	15.7	0.064
CNF/MWCNTs (10 wt%)	0.21	2.8	0.357
CNF/MWCNTs (15 wt%)	0.13	5.6	0.18
CNF/MWCNTs (20 wt%)	0.17	6.8	0.15

Table 10. Values of electrical resistivity/conductivity of developed multilayered composites

Sample ID	Thickness (cm)	Resistivity (Ω·cm)	Conductivity ($S \cdot cm^{-1}$)
MLC-1	0.22	76.63	0.013
MLC-2	0.3347	38.16	0.026

Table 11. Values of average EMI SE, average EMI shielding effectiveness per mm thickness, specific SE (SSE), and absolute shielding effectiveness (SSE/t) of developed composites

Sample ID	Average EMI SE (dB)	Average EMI SE/t (dB/mm)	SSE ($dB.cm^3.g^{-1}$)	SSE/t ($dB.cm^2.g^{-1}$)
Nylon 6/PANI mat	7	19.954	26.85	767
Nylon 6/PIn	6.53	6.22	25.24	240.4
CNF@700	8.83	5.74	321.8	2089.5
CNF@800	14.03	9.95	413.55	2933
CNF/Fe_3O_4 (5wt%)	12.05	7	610.45	3549.1
CNF/Fe_3O_4 (10 wt%)	17.8	9.78	799.14	4390.9
CNF/Fe_3O_4 (15 wt%)	14.47	8.04	362.01	2011.2
CNF/Fe_3O_4 (20 wt%)	13.15	6.73	478.4	2446.87
CNF/MWCNTs (5 wt%)	22.1	7.85	1297.8	4610.3
CNF/MWCNTs (10 wt%)	18.14	8.85	808.4	3943.2
CNF/MWCNTs (15 wt%)	14.47	11.1	736.9	5646.9
CNF/MWCNTs (20 wt%)	16.74	9.62	699.04	4017.4
Nylon 6/MWCNTs-COOH	10.44	16.32	45.91	717.3
Nylon 6/MWCNTs-NH_2	9.074	6.67	40.95	301.1
Nylon 6/MWCNTs-F	5.01	4.32	23.12	199.3
MLC1	21.14	9.61	22.35	235.2
MLC2	37.7	11.265	85.04	254.1
CNF-MWCNT mat IC-8-0.1 [15]	13.7	N/A	48.9	5433.3
Interlayered composite [15]	52	N/A	76.5	1176.9

The average values of Shielding effectiveness were obtained from the arithmetic average of 150 shielding values to their corresponding frequencies from 300 MHz to 1300 MHz. CNFs containing 5 wt % of MWCNTs indicating the uppermost specific shielding effectiveness (SSE) value of around 1298 $dB.cm^3.g^{-1}$. Maximum absolute shielding effectiveness was calculated a value of ~ 5647 $dB.cm^2.g^{-1}$ for CNFs/MWCNTs (15wt%). It is observed that the addition CNTs gradually decreases the SSE of CNFs-MWCNTs as the more filler loading is contributing supplementary weight to the carbon nanofibers. A similar case is also found from the calculated values of SSE for CNFs-Fe_3O_4. SSE for conducting polymers coated fiber mat shows close values but nylon 6/PANI is indicating the superior value in SSE/t than nylon 6/PIn. Low values of SSE of these MWCNT or CPs coated nylon 6 mats as their thickness was minimal. MWCNTs-COOH coated nylon mat represents the highest values for both SSE and SSE/t among other CNTs coated fiber mat. The values of absolute SE for NPs loaded CNFs offers high performance as the carbon nanofiber possesses lower density due to their porous structure. The final 8 layers composite is showing SSE and SSE/t of 85 $dB.cm^3.g^{-1}$ and 254 $dB.cm^2.g^{-1}$ respectively. The specific shielding effectiveness of MLC 2 shows better values than the previously discussed investigation on laminated composite[15]. The highest average EMI SE value recorded was around 38 dB for MLC 2. The additional epoxy applied in the interfaces was contributing to excess weight to the final composite resulting in low specific and absolute shielding effectiveness.

CHAPTER VI

CONCLUSION

Nylon 6 mats were successfully coated with functionalized CNTs showing conductive properties and EMI shielding performance with wave absorption mechanism. The same nano fiber mat was also decorated with polyindole conducting polymer by in-situ polymerization technique which surpasses the traditional polyaniline coated amide polymer substrate for both EMI shielding performance and electrical conductivity. 10 wt% Fe_3O_4 filler embedded CNF shows 100% more shielding effectiveness than CNF with no magnetite filler. Increasing carbonizing temperature may result increase of conductivity and electromagnetic properties. At 800^oC carbonization temperature, the 5 wt% CNT incorporated CNFs shows better electromagnetic performance while maintaining a continuous conductive network. The selected samples in the layered composite were evaluated also by calculated EMI SE which deviates from the experimental values due to omitting their multiple reflection and non-homogeneity along their thickness.

This study actually shows polyindole as a promising candidate for EMI shielding composite development. The aggregation of magnetite filler can be reduced by optimizing the weight percentage of filler with a proper dispersion steps resulting more porous site after carbonization. Due to well dispersiveness of functionalized CNTs in the solvent, they can be widely used filler in the polymer solution in Forcespinning® process for potential improvement of properties. Among all the samples, the eight layered composite displays a greater shielding effectiveness of 40 dB at 300-700 MHz.

CHAPTER VII

FUTURE WORK

A smooth surface of nanofibers can be achieved by modifying the technique of collecting fiber, number of cycles and run time during Forcespinning® which may play an important role in a homogenous dispersion of conducting nanoparticles. The dip coating technique with might be improved further by varying the amount of TFE addition and the associated experimental setup to provide better adsorption of functionalized CNTs on polymer substrate. Carbon nanofibers with an optimized amount of filler can be subjected to higher carbonization temperature in order to achieve higher electrical and electromagnetic properties. The compression of the laminated composite can be carried out with different pressure condition to find the effects on EMI shielding properties. This interlayered system contains heterogeneity along with its thickness. So, a new mathematical equation model to calculate the EMI SE of the composite should be developed to get a better relation to the experimental values.

REFERENCES

1. Qin, Y., *Medical textile materials*. 2015: Woodhead Publishing.

2. Zhang, D., *Advances in filament yarn spinning of textiles and polymers*. 2014: Elsevier.

3. Place, N.S.S. *What Is the Solar Cycle?* 2019, June 28; Available from: https://spaceplace.nasa.gov/solar-cycles/en/.

4. Jiang, D., et al., *Electromagnetic interference shielding polymers and nanocomposites-a review.* Polymer Reviews, 2019. **59**(2): p. 280-337.

5. Singh, R. and S.G. Kulkarni, *Nanocomposites based on transition metal oxides in polyvinyl alcohol for EMI shielding application.* Polymer bulletin, 2014. **71**(2): p. 497-513.

6. Yang, Q., et al., *Aligned polyaniline/porous biomass carbon composites with superior microwave absorption properties.* Journal of Materials Science: Materials in Electronics, 2019. **30**(2): p. 1374-1382.

7. Singh, A.K., et al., *A review of porous lightweight composite materials for electromagnetic interference shielding.* Composites Part B: Engineering, 2018. **149**: p. 188-197.

8. Tong, X.C., *Advanced materials and design for electromagnetic interference shielding*. 2016: CRC press.

9. Moore, N. *EMC/EMI Shielding Explained*. 2019, December 18; Available from: https://www.harwin.com/emc-emi-shielding-explained/.

10. Thomassin, J.-M., et al., *Polymer/carbon based composites as electromagnetic interference (EMI) shielding materials.* Materials Science and Engineering: R: Reports, 2013. **74**(7): p. 211-232.

11. *The Beginning of the EMI Field*. Oct 29, 2016; Available from: https://4emi.com/the-history-of-emi/beginning-emi-field/.

12. Chung, D., *Electromagnetic interference shielding effectiveness of carbon materials.* carbon, 2001. **39**(2): p. 279-285.

13. Engin, F.Z. and İ. Usta, *Development and characterisation of polyaniline/polyamide (PANI/PA) fabrics for electromagnetic shielding.* The Journal of The Textile Institute, 2015. **106**(8): p. 872-879.

14. Chung, D., *Materials for electromagnetic interference shielding.* Journal of Materials Engineering and performance, 2000. **9**(3): p. 350-354.

15. Ramírez-Herrera, C.A., et al., *Electrical Properties and Electromagnetic Interference Shielding Effectiveness of Interlayered Systems Composed by Carbon Nanotube Filled Carbon Nanofiber Mats and Polymer Composites.* Nanomaterials, 2019. **9**(2): p. 238.

16. Hong, S.Y., et al., *Anisotropic electromagnetic interference shielding properties of polymer-based composites with magnetically-responsive aligned Fe3O4 decorated reduced graphene oxide.* European Polymer Journal, 2020: p. 109595.

17. Fang, H., et al., *In-situ grown hollow Fe3O4 onto graphene foam nanocomposites with high EMI shielding effectiveness and thermal conductivity.* Composites Science and Technology, 2020. **188**: p. 107975.

18. Cheng, H., et al., *Synergetic effect of Fe3O4 nanoparticles and carbon on flexible poly (vinylidence fluoride) based films with higher heat dissipation to improve electromagnetic shielding.* Composites Part A: Applied Science and Manufacturing, 2019. **121**: p. 139-148.

19. Bayat, M., et al., *Electromagnetic interference shielding effectiveness of hybrid multifunctional Fe3O4/carbon nanofiber composite.* Polymer, 2014. **55**(3): p. 936-943.

20. Colaneri, N.F. and L. Schacklette, *EMI shielding measurements of conductive polymer blends.* IEEE transactions on instrumentation and measurement, 1992. **41**(2): p. 291-297.

21. Chen, Y., et al., *Multifunctional Cellulose/rGO/Fe3O4 Composite Aerogels for Electromagnetic Interference Shielding.* ACS Applied Materials & Interfaces, 2020. **12**(19): p. 22088-22098.

22. Chen, W., et al., *Enhanced electromagnetic interference shielding properties of carbon fiber veil/Fe3O4 nanoparticles/epoxy multiscale composites.* Materials Research Express, 2017. **4**(12): p. 126303.

23. Bhaskaran, K., R.K. Bheema, and K.C. Etika, *The influence of Fe3O4@ GNP hybrids on enhancing the EMI shielding effectiveness of epoxy composites in the X-band.* Synthetic Metals, 2020. **265**: p. 116374.

24. Zhan, Y., et al., *3D carbon fiber mats/nano-Fe3O4 hybrid material with high electromagnetic shielding performance.* Applied Surface Science, 2018. **444**: p. 710-720.

25. Liu, Y., et al., *Anisotropic thermal conductivity and electromagnetic interference shielding of epoxy nanocomposites based on magnetic driving reduced graphene oxide@ Fe3O4.* Composites Science and Technology, 2019. **174**: p. 1-10.

26. Fei, Y., et al., *Sandwich-like Magnetic Graphene Papers Prepared with MOF-Derived Fe3O4–C for Absorption-Dominated Electromagnetic Interference Shielding.* Industrial & Engineering Chemistry Research, 2019. **59**(1): p. 154-165.

27. Movassagh-Alanagh, F., et al., *Fabrication of microwave absorbing Fe3O4/MWCNTs@ CFs nanocomposite by means of an electrophoretic co-deposition process.* Synthetic Metals, 2019. **250**: p. 20-30.

28. Zhou, X., et al., *Synthesis of Fe3O4/carbon foams composites with broadened bandwidth and excellent electromagnetic wave absorption performance.* Composites Part A: Applied Science and Manufacturing, 2019. **127**: p. 105627.

29. Zhang, T., et al., *Fe3O4/carbon composite nanofiber absorber with enhanced microwave absorption performance.* Materials Science and Engineering: B, 2013. **178**(1): p. 1-9.

30. Zhu, S., et al., *Flexible Fe3O4/graphene foam/poly dimethylsiloxane composite for high-performance electromagnetic interference shielding.* Composites Science and Technology, 2020. **189**: p. 108012.

31. Miao, P., et al., *Poly (dimethylsilylene) diacetylene-guided ZIF-based heterostructures for full Ku-band electromagnetic wave absorption.* ACS applied materials & interfaces, 2019. **11**(19): p. 17706-17713.

32. Cao, M.-S., et al., *Ferroferric oxide/multiwalled carbon nanotube vs polyaniline/ferroferric oxide/multiwalled carbon nanotube multiheterostructures for highly effective microwave absorption.* ACS applied materials & interfaces, 2012. **4**(12): p. 6949-6956.

33. Liu, Y.-F., et al., *Segregated polypropylene/cross-linked poly (ethylene-co-1-octene)/multi-walled carbon nanotube nanocomposites with low percolation threshold and dominated negative temperature coefficient effect: Towards electromagnetic interference shielding and thermistors.* Composites Science and Technology, 2018. **159**: p. 152-161.

34. Liang, J., et al., *Electromagnetic interference shielding of graphene/epoxy composites.* Carbon, 2009. **47**(3): p. 922-925.

35. Mordina, B., et al., *Fe3O4 nanoparticles embedded hollow mesoporous carbon nanofibers and polydimethylsiloxane-based nanocomposites as efficient microwave absorber.* The Journal of Physical Chemistry C, 2017. **121**(14): p. 7810-7820.

36. Qiang, R., et al., *Metal organic framework-derived Fe/C nanocubes toward efficient microwave absorption.* Journal of Materials Chemistry A, 2015. **3**(25): p. 13426-13434.

37. Xia, T., et al., *Electrically conductive GNP/epoxy composites for out-of-autoclave thermoset curing through Joule heating.* Composites Science and Technology, 2018. **164**: p. 304-312.

38. Afzali, A., et al., *Electromagnetic properties of absorber fabric coated with BaFe12O19/MWCNTs/PANi nanocomposite in X and Ku bands frequency.* Journal of Magnetism and Magnetic Materials, 2017. **442**: p. 224-230.

39. Li, C., et al., *Lightweight three-dimensional Fe3O4/carbon micro-flowers with tunable microwave absorption properties.* Journal of Alloys and Compounds, 2019. **798**: p. 414-423.

40. Wei, S., et al., *Preparation of hierarchical core-shell C@ NiCo2O4@ Fe3O4 composites for enhanced microwave absorption performance.* Chemical Engineering Journal, 2017. **314**: p. 477-487.

41. Zhao, B., et al., *Yolk–shell Ni@ SnO2 composites with a designable interspace to improve the electromagnetic wave absorption properties.* ACS applied materials & interfaces, 2016. **8**(42): p. 28917-28925.

42. Guo, S., et al., *Fe ionic induced strong bioinspired Fe3O4@ graphene aerogel with excellent electromagnetic shielding effectiveness.* Applied Surface Science, 2020: p. 146569.

43. Wu, M., et al., *Microwave magnetic properties of Co 50/(SiO 2) 50 nanoparticles.* Applied Physics Letters, 2002. **80**(23): p. 4404-4406.

44. Wu, J. and D. Chung, *Combined use of magnetic and electrically conductive fillers in a polymer matrix for electromagnetic interference shielding.* Journal of Electronic Materials, 2008. **37**(8): p. 1088.

45. Zong, M., et al., *Facile preparation, high microwave absorption and microwave absorbing mechanism of RGO–Fe 3 O 4 composites.* RSC advances, 2013. **3**(45): p. 23638-23648.

46. Zhao, H., et al., *Enhanced X-band electromagnetic-interference shielding performance of layer-structured fabric-supported polyaniline/cobalt–nickel coatings.* ACS applied materials & interfaces, 2017. **9**(38): p. 33059-33070.

47. Dorraji, M.S., et al., *Microwave absorption properties of polyaniline-Fe3O4/ZnO-polyester nanocomposite: Preparation and optimization.* Applied Surface Science, 2016. **366**: p. 210-218.

48. Singh, K., et al., *Nanostructured graphene/Fe 3 O 4 incorporated polyaniline as a high performance shield against electromagnetic pollution.* Nanoscale, 2013. **5**(6): p. 2411-2420.

49. Wan, C. and J. Li, *Synthesis and electromagnetic interference shielding of cellulose-derived carbon aerogels functionalized with α-Fe2O3 and polypyrrole.* Carbohydrate polymers, 2017. **161**: p. 158-165.

50. Saini, P., et al., *Improved electromagnetic interference shielding response of poly (aniline)-coated fabrics containing dielectric and magnetic nanoparticles.* The Journal of Physical Chemistry C, 2012. **116**(24): p. 13403-13412.

51. Wang, G., et al., *Ultralow-threshold and lightweight biodegradable porous PLA/MWCNT with segregated conductive networks for high-performance thermal insulation and electromagnetic interference shielding applications.* ACS applied materials & interfaces, 2018. **10**(1): p. 1195-1203.

52. Pawar, S.P., et al., *Does the processing method resulting in different states of an interconnected network of multiwalled carbon nanotubes in polymeric blend nanocomposites affect EMI shielding properties?* ACS omega, 2018. **3**(5): p. 5771-5782.

53. Wang, Y., et al., *Hydro-sensitive sandwich structures for self-tunable smart electromagnetic shielding.* Chemical Engineering Journal, 2018. **344**: p. 342-352.

54. Wang, Z., R. Wei, and X. Liu, *Fluffy and ordered graphene multilayer films with improved electromagnetic interference shielding over X-band.* ACS Applied Materials & Interfaces, 2017. **9**(27): p. 22408-22419.

55. Yuan, J.-K., et al., *Biphasic polymer blends containing carbon nanotubes: heterogeneous nanotube distribution and its influence on the dielectric properties.* The Journal of Physical Chemistry C, 2012. **116**(2): p. 2051-2058.

56. Zhu, H., et al., *The electromagnetic property and microwave absorption of wormhole-like mesoporous carbons with different surface areas.* Journal of Materials Science, 2016. **51**(21): p. 9723-9731.

57. Huangfu, Y., et al., *Fabrication and investigation on the Fe3O4/thermally annealed graphene aerogel/epoxy electromagnetic interference shielding nanocomposites.* Composites Science and Technology, 2019. **169**: p. 70-75.

58. Kong, L., et al., *Electromagnetic wave absorption properties of graphene modified with carbon nanotube/poly (dimethyl siloxane) composites.* Carbon, 2014. **73**: p. 185-193.

59. Kim, S.H., et al., *Electrical properties and EMI shielding characteristics of polypyrrole–nylon 6 composite fabrics.* Journal of applied polymer science, 2003. **87**(12): p. 1969-1974.

60. Baker, C.O., et al., *Polyaniline nanofibers: broadening applications for conducting polymers.* Chemical Society Reviews, 2017. **46**(5): p. 1510-1525.

61. Alamer, F.A., *Structural and electrical properties of conductive cotton fabrics coated with the composite polyaniline/carbon black.* Cellulose, 2018. **25**(3): p. 2075-2082.

62. Liu, J., et al., *Microwave absorption enhancement of multifunctional composite microspheres with spinel Fe3O4 cores and anatase TiO2 shells.* Small, 2012. **8**(8): p. 1214-1221.

63. Chen, X., et al., *Preparation and microwave absorbing properties of nickel-coated carbon fiber with polyaniline via in situ polymerization.* Journal of Materials Science: Materials in Electronics, 2016. **27**(6): p. 5607-5612.

64. Yu, D., et al., *Preparation of silver-plated polyimide fabric initiated by polyaniline with electromagnetic shielding properties.* Journal of Industrial Textiles, 2018. **47**(6): p. 1392-1406.

65. Ates, M., T. Karazehir, and A. Sezai Sarac, *Conducting polymers and their applications.* Current Physical Chemistry, 2012. **2**(3): p. 224-240.

66. Bhagat, D. and G. Dhokane, *Ac conductivity investigation of polyindole/poly (vinyl acetate) composites.* Journal of Materials Science: Materials in Electronics, 2016. **27**(11): p. 11790-11797.

67. Sankar, S., et al., *Characterization, conductivity studies, dielectric properties, and gas sensing performance of in situ polymerized polyindole/copper alumina nanocomposites.* Journal of Applied Polymer Science, 2020: p. 49145.

68. Ebrahimpour, E., et al., *Poly (indole-co-thiophene)@ Fe3O4 as novel adsorbents for the extraction of aniline derivatives from water samples.* Microchemical Journal, 2017. **131**: p. 174-181.

69. Anjitha, T., et al., *Zinc ferrite@ polyindole nanocomposites: Synthesis, characterization and gas sensing applications.* Polymer Composites, 2019. **40**(7): p. 2802-2811.

70. Bhagat, D. and G. Dhokane, *Frequency Dependent Conductivity and Dielectric Behavior Studies of Cu Doped Polyindole in Presence of Poly (Vinyl Acetate).* Journal of Inorganic and Organometallic Polymers and Materials, 2017. **27**(1): p. 46-52.

71. Cai, Z., et al., *Electrospun polyindole nanofibers as a nano-adsorbent for heavy metal ions adsorption for wastewater treatment.* Fibers and Polymers, 2017. **18**(3): p. 502-513.

72. Wang, H., et al., *Bacterial cellulose nanofiber-supported polyaniline nanocomposites with flake-shaped morphology as supercapacitor electrodes.* The Journal of Physical Chemistry C, 2012. **116**(24): p. 13013-13019.

73. Bhardwaj, P., et al., *Exceptional electromagnetic radiation shielding performance and dielectric properties of surfactant assisted polypyrrole-carbon allotropes composites.* Radiation Physics and Chemistry, 2018. **151**: p. 156-163.

74. Wang, L.-X., X.-G. Li, and Y.-L. Yang, *Preparation, properties and applications of polypyrroles.* Reactive and Functional Polymers, 2001. **47**(2): p. 125-139.

75. Liu, H., et al., *Electrically conductive strain sensing polyurethane nanocomposites with synergistic carbon nanotubes and graphene bifillers.* Nanoscale, 2016. **8**(26): p. 12977-12989.

76. Liu, H., et al., *Electrically conductive thermoplastic elastomer nanocomposites at ultralow graphene loading levels for strain sensor applications.* Journal of Materials Chemistry C, 2016. **4**(1): p. 157-166.

77. Lee, S.H., J.H. Jung, and I.K. Oh, *3D Networked Graphene-Ferromagnetic Hybrids for Fast Shape Memory Polymers with Enhanced Mechanical Stiffness and Thermal Conductivity.* Small, 2014. **10**(19): p. 3880-3886.

78. Bhadra, S., et al., *Effect of different reaction parameters on the conductivity and dielectric properties of polyaniline synthesized electrochemically and modeling of conductivity against reaction parameters through regression analysis.* Journal of Polymer Science Part B: Polymer Physics, 2007. **45**(15): p. 2046-2059.

79. Saini, P., et al., *Polyaniline–MWCNT nanocomposites for microwave absorption and EMI shielding.* Materials Chemistry and Physics, 2009. **113**(2-3): p. 919-926.

80. Im, J.S., et al., *Enhanced adhesion and dispersion of carbon nanotube in PANI/PEO electrospun fibers for shielding effectiveness of electromagnetic interference.* Colloids and Surfaces A: Physicochemical and Engineering Aspects, 2010. **364**(1-3): p. 151-157.

81. *Nylon 6 And Nylon 66*. 2020 Sep 7 2020; Available from: https://www.encyclopedia.com/science/academic-and-educational-journals/nylon-6-and-nylon-66.

82. Matthies, P. and W.F. Seydl, *History and development of nylon 6*, in *High Performance Polymers: Their Origin and Development*. 1986, Springer. p. 39-53.

83. Ryu, Y.J., et al., *Transport properties of electrospun nylon 6 nonwoven mats.* European Polymer Journal, 2003. **39**(9): p. 1883-1889.

84. Fong, H., et al., *Generation of electrospun fibers of nylon 6 and nylon 6-montmorillonite nanocomposite.* Polymer, 2002. **43**(3): p. 775-780.

85. Hancock, T.A., J.E. Spruiell, and J.L. White, *Wet spinning of aliphatic and aromatic polyamides.* Journal of Applied Polymer Science, 1977. **21**(5): p. 1227-1247.

86. Weng, B., F. Xu, and K. Lozano, *Development of hierarchical structured carbon nanotube-nylon nanofiber mats.* Journal of Applied Polymer Science, 2015. **132**(38).

87. Jose, M.V., et al., *Morphology and mechanical properties of Nylon 6/MWNT nanofibers.* Polymer, 2007. **48**(4): p. 1096-1104.

88. Murase, S., et al., *Structure and properties of high-speed spun fibers of nylon 6.* Macromolecular Chemistry and Physics, 1997. **198**(2): p. 561-572.

89. Pathmanathan, K. and G. Johari, *The effect of increased crystallization on the electrical properties of nylon-12.* Journal of Polymer Science Part B: Polymer Physics, 1993. **31**(3): p. 265-271.

90. Zhang, C., et al., *Electromagnetic and microwave absorption properties of surface modified Fe–Si–Al flakes with nylon.* Journal of alloys and compounds, 2012. **527**: p. 71-75.

91. Oh, K.W., S.H. Kim, and E.A. Kim, *Improved surface characteristics and the conductivity of polyaniline–nylon 6 fabrics by plasma treatment.* Journal of Applied Polymer Science, 2001. **81**(3): p. 684-694.

92. Starkweather Jr, H.W. and P. Avakian, *Conductivity and the electric modulus in polymers.* Journal of Polymer Science Part B: Polymer Physics, 1992. **30**(6): p. 637-641.

93. Nirmala, R., et al., *Electrical properties of ultrafine nylon-6 nanofibers prepared via electrospinning.* Fibers and Polymers, 2011. **12**(8): p. 1021-1024.

94. Vankayala, R.R., et al., *Enhanced electrical conductivity of nylon 6 composite using polyaniline-coated multi-walled carbon nanotubes as additives.* Polymer, 2011. **52**(15): p. 3337-3343.

95. Qu, L., et al., *Soluble nylon-functionalized carbon nanotubes from anionic ring-opening polymerization from nanotube surface.* Macromolecules, 2005. **38**(24): p. 10328-10331.

96. Wikipedia. *Nylon 6*. 8 August 2020; Available from: https://en.wikipedia.org/wiki/Nylon_6.

97. Goodfellow. *Polyamide - Nylon 6 (PA 6) Material Information*. Available from: http://www.goodfellow.com/E/Polyamide-Nylon-6.html.

98. Matweb. *Overview of materials for Nylon 6*. Available from: http://www.matweb.com/search/datasheet.aspx?MatGUID=8d78f3cfcb6f49d595896ce6ce6a2ef1&ckck=1.

99. Britannica, T.E.o.E. *Polyacrylonitrile chemical compound*. Available from: https://www.britannica.com/science/polyacrylonitrile.

100. Bolboacă, S. and L. JÄNTSCHI, *Helical structure of linear homopolymers.* Materials Research Proceedings, 2018. **8**.

101. Rein, H., *Polyacrylnitril-Fasern Eine neue Gruppe von synthethischen Fasern.* Angewandte Chemie, 1948. **60**(6): p. 159-161.

102. Kalashnik, A., et al., *Properties and structure of polyacrylonitrile fibers.* Polymer Science Series A, 2010. **52**(11): p. 1233-1238.

103. Tsai, J.S. and C.H. Lin, *Effect of comonomer composition on the properties of polyacrylonitrile precursor and resulting carbon fiber.* Journal of applied polymer science, 1991. **43**(4): p. 679-685.

104. Matulka, R. *Top 9 Things You Didn't Know about Carbon Fiber*. March 29, 2013; Available from: https://www.energy.gov/articles/top-9-things-you-didn-t-know-about-carbon-fiber.

105. Henrici-Olive, G. and S. Olivé, *Molecular interactions and macroscopic properties of polyacrylonitrile and model substances*, in *Chemistry*. 1979, Springer. p. 123-152.

106. Allen, S., et al., *The barrier properties of polyacrylonitrile.* Journal of Membrane Science, 1977. **2**: p. 153-163.

107. Robson, D., F. Assabghy, and D. Ingram, *Some electronic properties of polyacrylonitrile-based carbon fibres.* Journal of Physics D: Applied Physics, 1972. **5**(1): p. 169.

108. Tsai, J.S. and C.H. Lin, *The effect of molecular weight on the cross section and properties of polyacrylonitrile precursor and resulting carbon fiber.* Journal of applied polymer science, 1991. **42**(11): p. 3045-3050.

109. Dunn, P. and B. Ennis, *Thermal analysis of polyacrylonitrile: Identification of acrylic fibres by differential thermal analysis.* Thermochimica Acta, 1971. **3**(2): p. 81-87.

110. Kimmel, R. and R. Andrews, *Birefringence effects in acrylonitrile polymers. II. The nature of the 140 C transition.* Journal of Applied Physics, 1965. **36**(10): p. 3063-3071.

111. Andrews, R. *Transition phenomena and solid-state structure in glassy polymers*. in *Journal of Polymer Science Part C: Polymer Symposia*. 1966. Wiley Online Library.

112. Warner, S., L. Peebles, and D.R. Uhlmann, *Oxidative stabilization of acrylic fibres.* Journal of Materials Science, 1979. **14**(3): p. 556-564.

113. Houtz, R., *" Orlon" Acrylic Fiber: Chemistry and Properties.* Textile Research Journal, 1950. **20**(11): p. 786-801.

114. Bohn, C., J. Schaefgen, and W. Statton, *Laterally ordered polymers: polyacrylonitrile and poly (vinyl trifluoroacetate).* Journal of Polymer Science, 1961. **55**(162): p. 531-549.

115. Hinrichsen, G. *Structural changes of drawn polyacrylonitrile during annealing*. in *Journal of Polymer Science Part C: Polymer Symposia*. 1972. Wiley Online Library.

116. Lindenmeyer, P. and R. Hosemann, *Application of the theory of paracrystals to the crystal structure analysis of polyacrylonitrile.* Journal of Applied Physics, 1963. **34**(1): p. 42-45.

117. Imai, Y., S. Minami, and T. Yoshihara, *Joh, Y. andSato, HJ Polym.* Sci. B, 1970. **8**: p. 281.

118. Hu, X., D. Johnson, and J. Tomka, *Molecular modelling of the structure of polyacrylonitrile fibres.* Journal of the Textile Institute, 1995. **86**(2): p. 322-331.

119. *Polyacrylonitrile*. 16 July 2020; Available from: https://en.wikipedia.org/wiki/Polyacrylonitrile#cite_note-3.

120. *POLYACRYLONITRILE PROPERTIES*. 2016; Available from: http://www.igtpan.com/Ingles/propriedade-poli.asp.

121. Zhu, C.-L., et al., *Fe3O4/TiO2 core/shell nanotubes: synthesis and magnetic and electromagnetic wave absorption characteristics.* The Journal of Physical Chemistry C, 2010. **114**(39): p. 16229-16235.

122. Wang, C., et al., *The electromagnetic property of chemically reduced graphene oxide and its application as microwave absorbing material.* Applied Physics Letters, 2011. **98**(7): p. 072906.

123. Ohlan, A., et al., *Microwave absorption properties of conducting polymer composite with barium ferrite nanoparticles in 12.4–18 GHz.* Applied physics letters, 2008. **93**(5): p. 053114.

124. Ghanbari, D., M. Salavati-Niasari, and M. Ghasemi-Kooch, *A sonochemical method for synthesis of Fe3O4 nanoparticles and thermal stable PVA-based magnetic nanocomposite.* Journal of Industrial and Engineering Chemistry, 2014. **20**(6): p. 3970-3974.

125. Zhou, C., et al., *Lightweight hollow carbon nanospheres with tunable sizes towards enhancement in microwave absorption.* Carbon, 2016. **108**: p. 234-241.

126. Dhawan, S., et al., *Conducting polymer embedded with nanoferrite and titanium dioxide nanoparticles for microwave absorption.* Synthetic Metals, 2009. **159**(21-22): p. 2259-2262.

127. Liang, C., et al., *SiC–Fe 3 O 4 dielectric–magnetic hybrid nanowires: controllable fabrication, characterization and electromagnetic wave absorption.* Journal of Materials Chemistry A, 2014. **2**(39): p. 16397-16402.

128. Xu, Y., et al., *Gradient structure design of flexible waterborne polyurethane conductive films for ultraefficient electromagnetic shielding with low reflection characteristic.* ACS applied materials & interfaces, 2018. **10**(22): p. 19143-19152.

129. Ni, S., et al., *Hydrothermal synthesis and microwave absorption properties of Fe3O4 nanocrystals.* Journal of Physics D: Applied Physics, 2009. **42**(5): p. 055004.

130. Marsden, A., et al., *Electrical percolation in graphene–polymer composites.* 2D Materials, 2018. **5**(3): p. 032003.

131. Zhang, H., et al., *Robust and flexible cellulose nanofiber/multiwalled carbon nanotube film for high-performance electromagnetic interference shielding.* Industrial & Engineering Chemistry Research, 2018. **57**(50): p. 17152-17160.

132. Liu, H.-Y., et al., *Effect of Fe3O4 nanoparticles on magnetic electrospun nanofibers.* The Journal of The Textile Institute, 2015. **106**(5): p. 503-509.

133. Weng, B., et al., *The production of carbon nanotube reinforced poly (vinyl) butyral nanofibers by the Forcespinning® method.* Polymer Engineering & Science, 2015. **55**(1): p. 81-87.

134. Sebe, I., et al., *Polymer structure and antimicrobial activity of polyvinylpyrrolidone-based iodine nanofibers prepared with high-speed rotary spinning technique.* International journal of pharmaceutics, 2013. **458**(1): p. 99-103.

135. Nava, R., et al., *Centrifugal spinning: an alternative for large scale production of silicon–carbon composite nanofibers for lithium ion battery anodes.* ACS applied materials & interfaces, 2016. **8**(43): p. 29365-29372.

136. Upson, S.J., et al., *Centrifugally spun PHBV micro and nanofibres.* Materials Science and Engineering: C, 2017. **76**: p. 190-195.

137. Weng, B., F. Xu, and K. Lozano, *Mass production of carbon nanotube-reinforced polyacrylonitrile fine composite fibers.* Journal of Applied Polymer Science, 2014. **131**(11).

138. Weng, B., et al., *Mass production of carbon nanotube reinforced poly (methyl methacrylate) nonwoven nanofiber mats.* Carbon, 2014. **75**: p. 217-226.

139. Patlan, R., et al., *Fabrication and Characterization of Poly (L-lactic Acid) Fiber Mats Using Centrifugal Spinning.* Fibers and Polymers, 2018. **19**(6): p. 1271-1277.

140. Akia, M., et al., *High-Throughput Production With Improved Functionality and Graphitization of Carbon Fine Fibers Developed from Sodium Chloride-Polyacrylonitrile Precursors.* Polymer Engineering & Science, 2018. **58**(11): p. 2047-2054.

141. Li, Y., et al., *Preparation of SiO 2/PS superhydrophobic fibers with bionic controllable micro–nano structure via centrifugal spinning.* RSC advances, 2017. **7**(18): p. 11041-11048.

142. Phasuksom, K., W. Prissanaroon-Ouajai, and A. Sirivat, *A highly responsive methanol sensor based on graphene oxide/polyindole composites.* RSC Advances, 2020. **10**(26): p. 15206-15220.

143. Phasuksom, K. and A. Sirivat, *Synthesis of nano-sized polyindole via emulsion polymerization and doping.* Synthetic Metals, 2016. **219**: p. 142-153.

144. Dogan, E., E. Ozkazanc, and H. Ozkazanc, *Multifunctional polyindole/nanometal-oxide composites: Optoelectronic and charge transport properties.* Synthetic Metals, 2019. **256**: p. 116154.

145. Shakeel, N., et al., *Green synthesis of Zno nanoparticles decorated on polyindole functionalized-Mcnts and used as anode material for enzymatic biofuel cell applications.* Scientific Reports, 2020. **10**(1): p. 1-10.

146. Bela Purty, R.B.C., Amrita Biswas, G. Udayabhanu, *Chemically grown mesoporous f-CNT/α-MnO2/PIn nanocomposites as electrode materials for supercapacitor application.* Polymer Bulletin, 2019(4/2019).

147. Maarouf, E., D. Billaud, and E. Hannecart, *Electrochemical cycling and electrochromic properties of polyindole.* Materials research bulletin, 1994. **29**(6): p. 637-643.

148. Jayakrishnan, P. and M. Ramesan, *Synthesis, characterization, electrical conductivity and material properties of magnetite/polyindole/poly (vinyl alcohol) blend nanocomposites.* Journal of Inorganic and Organometallic Polymers and Materials, 2017. **27**(1): p. 323-333.

149. Elango, M., et al., *Investigation of structural, morphological and antimicrobial properties of polyindole/Ag doped CeO2 nanocomposites.* Materials Today: Proceedings, 2019.

150. Moreno, I., et al., *Facile preparation of transparent and conductive polymer films based on silver nanowire/polycarbonate nanocomposites.* Nanotechnology, 2013. **24**(27): p. 275603.

151. Badrossamay, M.R., et al., *Nanofiber assembly by rotary jet-spinning.* Nano letters, 2010. **10**(6): p. 2257-2261.

152. Shanmuganathan, K., et al., *Solventless high throughput manufacturing of poly (butylene terephthalate) nanofibers.* ACS Macro Letters, 2012. **1**(8): p. 960-964.

153. Vida, T.A., et al., *Fibrous PCL/PLLA scaffolds obtained by rotary jet spinning and electrospinning.* Materials Research, 2017. **20**: p. 910-916.

154. Liu, C., et al., *A comparison of centrifugally-spun and electrospun regenerated silk fibroin nanofiber structures and properties.* Rsc Advances, 2015. **5**(119): p. 98553-98558.

155. Vasquez, H., et al., *Titanium Dioxide Nanofibers through Forcespinning.* Journal of Engineered Fibers and Fabrics, 2015. **10**(2): p. 155892501501000215.

156. Sarkar, K., et al., *Electrospinning to forcespinning™.* Materials today, 2010. **13**(11): p. 12-14.

157. Rane, Y., et al., *Preparation of superhydrophobic Teflon® AF 1600 sub-micron fibers and yarns using the forcespinning technique.* Journal of Engineered Fibers and Fabrics, 2013. **8**(4): p. 88-95.

158. Padron, S., et al., *Production and characterization of hybrid BEH-PPV/PEO conjugated polymer nanofibers by forcespinning™.* Journal of applied polymer science, 2012. **125**(5): p. 3610-3616.

159. Raghavan, B., H. Soto, and K. Lozano, *Fabrication of melt spun polypropylene nanofibers by forcespinning.* Journal of Engineered Fibers and Fabrics, 2013. **8**(1): p. 155892501300800106.

160. Padron, S., D.I. Caruntu, and K. Lozano. *Influence of Viscosity on Forcespinning™ Dynamics*. in *ASME 2012 International Mechanical Engineering Congress and Exposition*. 2012. American Society of Mechanical Engineers Digital Collection.

161. Padron, S., D.I. Caruntu, and K. Lozano. *On 2D forcespinning™ modeling*. in *ASME 2011 International Mechanical Engineering Congress and Exposition*. 2011. American Society of Mechanical Engineers Digital Collection.

162. Riahi, D.N., et al., *On nonlinear rotating polymeric jets during forcespinning process.* Fluid Dynamics Research, 2018. **50**(6): p. 065507.

163. Mahalingam, S. and M. Edirisinghe, *Forming of polymer nanofibers by a pressurised gyration process.* Macromolecular rapid communications, 2013. **34**(14): p. 1134-1139.

164. Mary, L.A., et al., *Centrifugal spun ultrafine fibrous web as a potential drug delivery vehicle.* Express Polymer Letters, 2013. **7**(3): p. 238-248.

165. Li, X., H. Chen, and B. Yang, *Centrifugally spun starch-based fibers from amylopectin rich starches.* Carbohydrate polymers, 2016. **137**: p. 459-465.

166. Sinatra, N.R., J.U. Lind, and K.K. Parker. *Fabricating multi-material nanofabrics using rotary jet spinning*. in *2017 IEEE 17th International Conference on Nanotechnology (IEEE-NANO)*. 2017. IEEE.

167. Andjani, D., et al. *Fabrication of Polyvinylpyrrolidone Fibers by Means of Rotary Forcespinning Method*. in *IOP Conference Series: Materials Science and Engineering*. 2018. IOP Publishing.

168. Rogalski, J.J., C.W. Bastiaansen, and T. Peijs, *PA6 nanofibre production: a comparison between rotary jet spinning and electrospinning.* Fibers, 2018. **6**(2): p. 37.

169. Dotto, G., et al., *Chitosan/polyamide nanofibers prepared by Forcespinning® technology: A new adsorbent to remove anionic dyes from aqueous solutions.* Journal of cleaner production, 2017. **144**: p. 120-129.

170. Cremar, L.D., et al., *Mechanical and electrical characterization of carbon nanofibers produced from water soluble precursors.* Materials Today Communications, 2016. **7**: p. 134-139.

171. Mîndru, T.B., et al., *Morphological aspects of polymer fiber mats obtained by air flow rotary-jet spinning.* Fibers and Polymers, 2013. **14**(9): p. 1526-1534.

172. Xu, F., et al., *Fabrication of cellulose fine fiber based membranes embedded with silver nanoparticles via Forcespinning.* Journal of Polymer Engineering, 2016. **36**(3): p. 269-278.

173. Szabó, P., et al., *Preparation of hydroxypropyl cellulose microfibers by high-speed rotary spinning and prediction of the fiber-forming properties of hydroxypropyl cellulose gels by texture analysis.* Cellulose, 2014. **21**(6): p. 4419-4427.

174. Vo, P.P., et al., *Centrifugally spun recycled PET: Processing and characterization.* Polymers, 2018. **10**(6): p. 680.

175. Golecki, H.M., et al., *Effect of solvent evaporation on fiber morphology in rotary jet spinning.* Langmuir, 2014. **30**(44): p. 13369-13374.

176. Gonzalez, G.M., et al., *Production of Synthetic, Para-Aramid and Biopolymer Nanofibers by Immersion Rotary Jet-Spinning.* Macromolecular Materials and Engineering, 2017. **302**(1): p. 1600365.

177. Ren, L., et al., *Large-scale and highly efficient synthesis of micro-and nano-fibers with controlled fiber morphology by centrifugal jet spinning for tissue regeneration.* Nanoscale, 2013. **5**(6): p. 2337-2345.

178. Badrossamay, M.R., et al., *Engineering hybrid polymer-protein super-aligned nanofibers via rotary jet spinning.* Biomaterials, 2014. **35**(10): p. 3188-3197.

179. Schabikowski, M., et al., *Rotary jet-spinning of hematite fibers.* Textile Research Journal, 2015. **85**(3): p. 316-324.

180. Stojanovska, E., et al., *Developing lignin-based bio-nanofibers by centrifugal spinning technique.* International journal of biological macromolecules, 2018. **113**: p. 98-105.

181. Zander, N.E., *Formation of melt and solution spun polycaprolactone fibers by centrifugal spinning.* Journal of Applied Polymer Science, 2015. **132**(2).

182. Wallwork, I., et al., *The trajectory and stability of a spiralling liquid jet. Part 1. Inviscid theory.* Journal of Fluid Mechanics, 2002. **459**: p. 43.

183. Decent, S., A. King, and I. Wallwork, *Free jets spun from a prilling tower.* Journal of Engineering Mathematics, 2002. **42**(3-4): p. 265-282.

184. Akia, M., et al., *In situ production of graphene–fiber hybrid structures.* ACS applied materials & interfaces, 2017. **9**(30): p. 25474-25480.

185. Akia, M., et al., *Development and optimization of alumina fine fibers utilizing a centrifugal spinning process.* Microporous and Mesoporous Materials, 2018. **262**: p. 175-181.

186. Cremar, L., et al., *Development of antimicrobial chitosan based nanofiber dressings for wound healing applications.* Nanomedicine Journal, 2018. **5**(1): p. 6-14.

187. Zuniga, L., et al., *Multichannel hollow structure for improved electrochemical performance of TiO2/Carbon composite nanofibers as anodes for lithium ion batteries.* Journal of Alloys and Compounds, 2016. **686**: p. 733-743.

188. Xu, F., et al., *Large-scale production of a ternary composite nanofiber membrane for wound dressing applications.* Journal of bioactive and compatible polymers, 2014. **29**(6): p. 646-660.

189. Li, Q., et al., *Heterogeneous Manganese Oxide-Encased Carbon Nanocomposite Fibers for High Performance Pseudocapacitors.* Ceramic Materials for Energy Applications III, 2013: p. 41-55.

190. Akia, M., K.A. Mkhoyan, and K. Lozano, *Synthesis of multiwall α-Fe2O3 hollow fibers via a centrifugal spinning technique.* Materials Science and Engineering: C, 2019. **102**: p. 552-557.

191. Altecor, A., Y. Mao, and K. Lozano, *Large-scale synthesis of tin-doped indium oxide nanofibers using water as solvent.* Functional Materials Letters, 2012. **5**(03): p. 1250020.

192. Nancy Birkner (UCD), Q.W.U. *How an FTIR Spectrometer Operates*. Aug 15, 2020; Available from: https://chem.libretexts.org/Bookshelves/Physical_and_Theoretical_Chemistry_Textbook_Maps/Supplemental_Modules_(Physical_and_Theoretical_Chemistry)/Spectroscopy/Vibrational_Spectroscopy/Infrared_Spectroscopy/How_an_FTIR_Spectrometer_Operates.

193. Fang, Y., et al., *Tin fluorophosphate nonwovens by melt state centrifugal Forcespinning.* Journal of materials science, 2014. **49**(24): p. 8252-8260.

194. Tissera, N.D., et al., *Heterogeneous in situ polymerization of polyaniline (PANI) nanofibers on cotton textiles: improved electrical conductivity, electrical switching, and tuning properties.* Carbohydrate polymers, 2018. **186**: p. 35-44.

195. Vasquez, H., et al., *Simple device for electromagnetic interference shielding effectiveness measurement.* IEEE EMC Soc. Newslett, 2009. **220**: p. 62-68.

196. Oraon, R., et al., *Hierarchical self-assembled nanoclay derived mesoporous CNT/polyindole electrode for supercapacitors.* RSC advances, 2016. **6**(69): p. 64271-64284.

197. Park, I.H., S.H. Kwon, and H.J. Choi, *Emulsion-polymerized polyindole nanoparticles and their electrorheology.* Journal of Applied Polymer Science, 2018. **135**(25): p. 46384.

198. Pai, C.-L., M.C. Boyce, and G.C. Rutledge, *Morphology of porous and wrinkled fibers of polystyrene electrospun from dimethylformamide.* Macromolecules, 2009. **42**(6): p. 2102-2114.

199. Wang, S., et al., *Effective amino-functionalization of carbon nanotubes for reinforcing epoxy polymer composites.* Nanotechnology, 2006. **17**(6): p. 1551.

200. Salinas, A., et al., *Production of b-Silicon Carbide Nanofibers using the Forcespinning® Method.* 2016.

201. Bayat, M., H. Yang, and F. Ko, *Electromagnetic properties of electrospun Fe3O4/carbon composite nanofibers.* Polymer, 2011. **52**(7): p. 1645-1653.

202. Kar, G.P., et al., *Tailoring the dispersion of multiwall carbon nanotubes in co-continuous PVDF/ABS blends to design materials with enhanced electromagnetic interference shielding.* Journal of Materials Chemistry A, 2015. **3**(15): p. 7974-7985.

APPENDIX A

APPENDIX A

EXTENDED SEM MORPHOLOGY OF THE SAMPLES

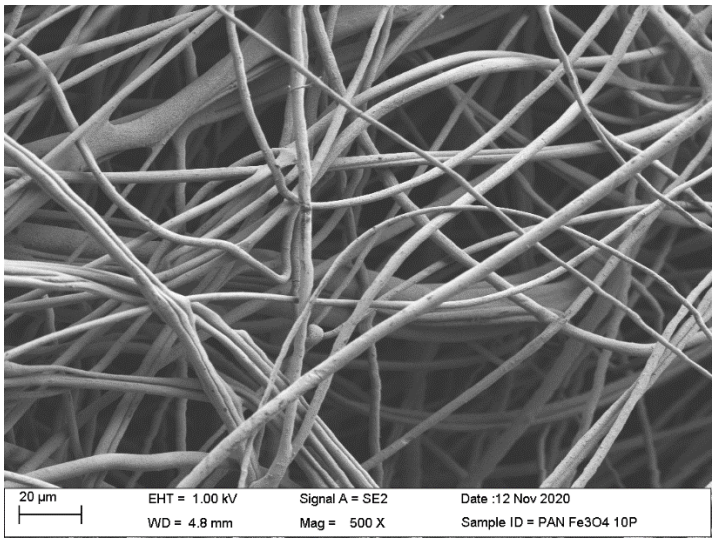

Figure S1. SEM of PAN/Fe_3O_4 (10 wt%)

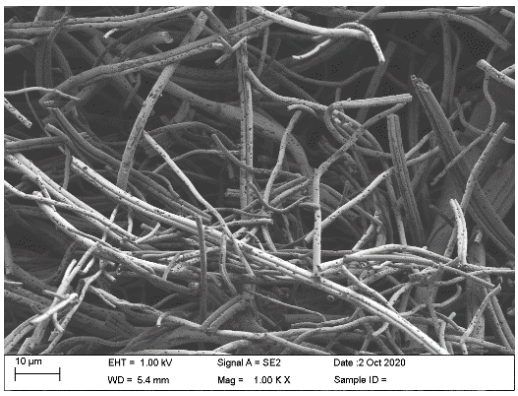

(a)

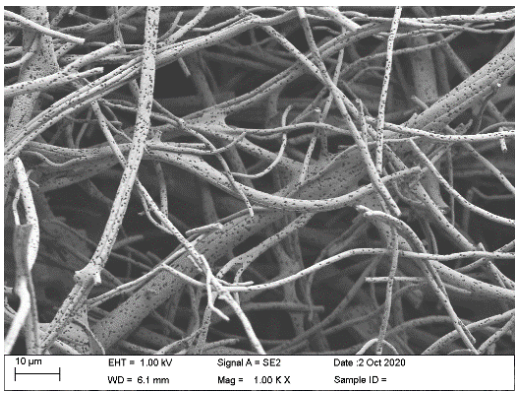

(b)

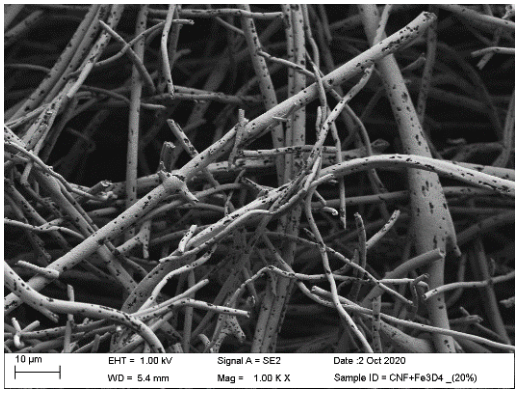

(c)

Figure S2. SEM of (a) 5 wt% (b) 10 wt% & (c) 20 wt % Fe_3O_4 embedded CNFs

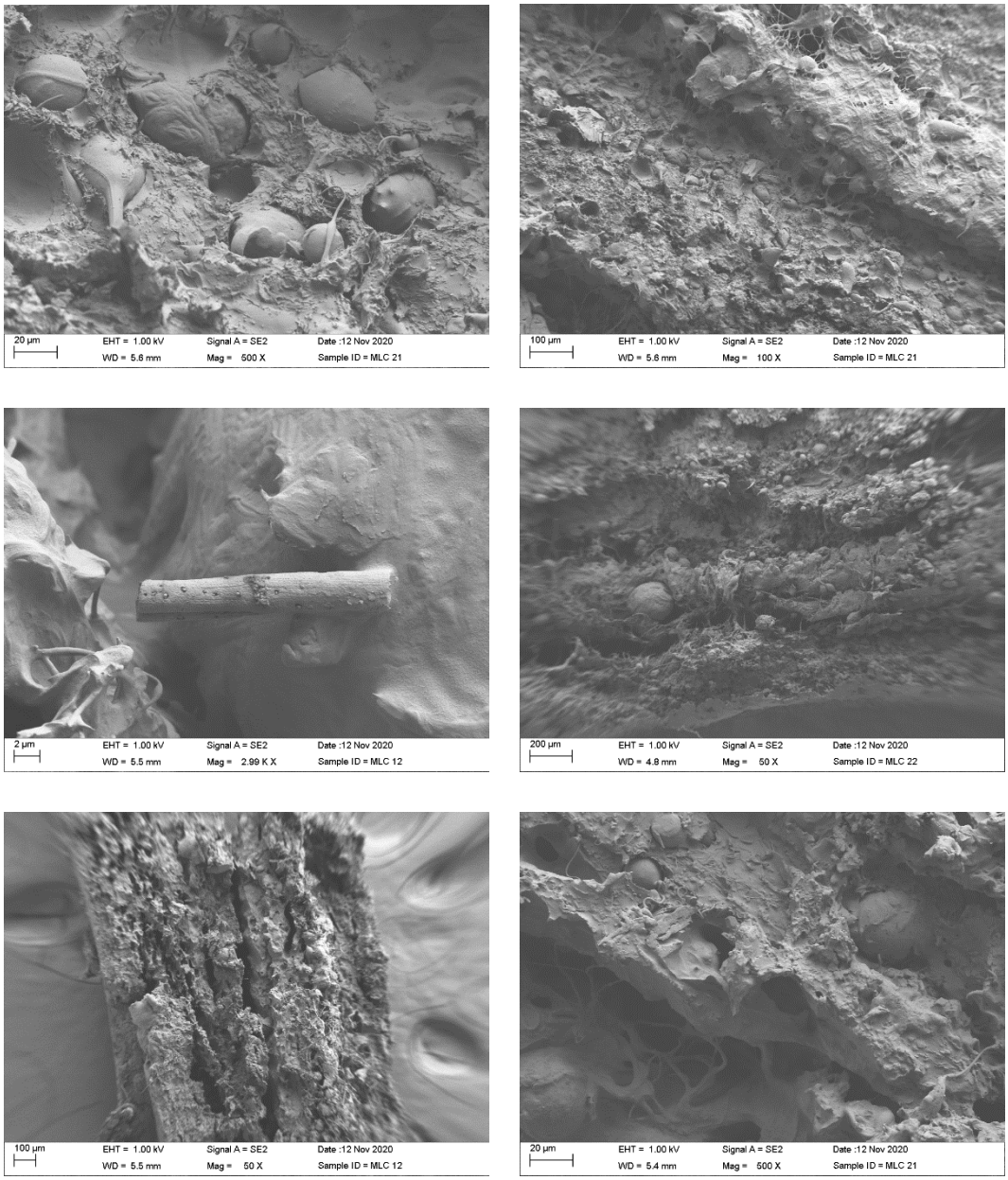

Figure S3. Different SEM magnification view of multilayered composite (MLC)

Table A1. State-of-the-Art Equipment

Equipment	Purpose	Results Obtained
SEM/EDS	Used to characterize all materials prepared in the work	Morphology, fiber diameter, and elemental mapping
Forcespinning®	Fiber fabrication	Different polymer fiber mats to produce carbon fiber and conductive surface
Vector Network Analyzer	Used to evaluate the EMI shielding properties	Total shielding and reflection mechanism were obtained for all the samples
Four Point Probe	Used to evaluate electrical properties	To measure the electrical resistivity and conductivity of the samples

Table A2. State-of-the-Art Software

Software	Purpose	Results Obtained
ORIGIN	Plotting EMI shielding results, histograms, and normal distribution for fiber diameter measurements	Reflection loss, Total EMI shielding of all the samples
EndNote	Sorting of citations in publications and thesis manuscript	Two ongoing research articles as first author
Microsoft Word	Writing the thesis manuscript	Two ongoing research articles as first author
PowerPoint	To prepare the thesis/research presentation	Developing flowchart, diagram etc for presentation
Excel	Organizing data	Calculating results of theoretical and experimental result of EMI and electrical properties

BIOGRAPHICAL SKETCH

Shaik Merkatur Hakim Marjuban was born in Rangpur city, Bangladesh, in December 1994. He has spent his childhood in Lalmonirhut, a remote area until he finished his fifth grade. Then he moved to Rangpur city where he had lived for over 11 years. He went to Cantonment Public School & College, Rangpur and completed his elementary school education and pursued a secondary school certificate and higher secondary certificate degree in 2009 and 2011 respectively.

In April 2012, he entered the Bangladesh University of Engineering and Technology (BUET), Dhaka, Bangladesh to pursue his bachelor's in Mechanical Engineering. During this time, he had participated in student organizations such as Greater Rangpur Students Welfare Association (GRSWA), Mechanical Engineering Association (MEA), Badhan (Blood donation organization) etc. He also availed an opportunity to participate in an internship program at ACI Pharmaceuticals Ltd, Narayanganj in summer of 2016. In February 2017, he graduated from BUET with a bachelor's degree in Mechanical Engineering. In the end of 2018, he was awarded with the Presidential Graduate Research Assistantship (PGRA) scholarship which allowed him to pursue his master's program in the US. After two years of research on polymer composite materials, he earned his Master of Science in Mechanical Engineering from University of Texas Rio Grande Valley (UTRGV) in December 2020.